Syracuse University

SURFACE

Dissertations - ALL SURFACE

December 2020

Modeling and Simulation of Morphological Instabilities in Thin Elastic Solids

Junbo Chen
Syracuse University

Follow this and additional works at: https://surface.syr.edu/etd

 Part of the Engineering Commons

Recommended Citation

Chen, Junbo, "Modeling and Simulation of Morphological Instabilities in Thin Elastic Solids" (2020). *Dissertations - ALL*. 1198.
https://surface.syr.edu/etd/1198

This Dissertation is brought to you for free and open access by the SURFACE at SURFACE. It has been accepted for inclusion in Dissertations - ALL by an authorized administrator of SURFACE. For more information, please contact surface@syr.edu.

Abstract

The study of morphological instabilities in thin solids, such as buckling of thin shells and wrinkling of thin sheets, is of growing interest to a number of academic disciplines including engineering, physics, biology, and many others. For example, buckling has traditionally been regarded as an unfavorable phenomenon in engineering design, but emerging technologies consider such behavior as an opportunity for novel functionality. The formation of wrinkle patterns on thin sheets has also emerged rapidly as canonical problems to investigate pattern formation in the physics community. The nonlinearities of the post-buckling behaviors encountered in these problems make theoretical analysis a challenging endeavor, thus highlighting the important role of numerical methods in the study of these problems. Our modeling and simulations of several prototypical instability problems – the buckling of spherical cap shells and cylindrical shells, and the wrinkling of annular sheets – reveal the complex post-buckling morphologies and energy landscapes. Our computational frameworks are promising for a wide range of applications, such as designing robust thin shell structures, developing buckling-induced smart devices, and explaining pattern formation in disordered systems.

Modeling and Simulation of Morphological Instabilities in Thin Elastic Solids

by

Junbo Chen

B.S., Tongji University, 2015

M.S., Northwestern University, 2017

Dissertation

Submitted in partial fulfillment of the requirements for the degree of

Doctor of Philosophy in Mechanical and Aerospace Engineering

Syracuse University

December 2020

Copyright © Junbo Chen 2020

All Rights Reserved

Preface

Chapter 3.4 is based on the collaborative work with Prof. Halim Kusumaatmaja's group at Durham University, UK. I conducted a proof-of-concept study on the minimum energy path search of a spherical cap buckling problem (detailed in Chapter 3.3). I developed the discrete shell model for cylindrical shells and implemented it in FORTRAN code, which is integrated into Prof. Kusumaatmaja's in-house pathfinding code to survey energy landscapes of cylinders under compressive loads. This collaborative work has been published in Communication Physics [112].

Chapter 4 is based on the collaborative work with Prof. Joseph D. Paulsen's group at Syracuse University and Prof. Benny Davidovitch's group at the University of Massachusetts, Amherst. I set up the finite element model for the Lame problem and performed the simulations (detailed in sections 4.4 and 4.5) to compare with the theoretical predictions (Prof. Benny Davidovitch) and experimental measurements (Prof. Joseph D. Paulsen). The work has been published in Proceedings of the National Academy of Sciences of the United States of America [143].

Acknowledgments

Foremost, I would like to express my sincere gratitude to my advisor Prof. Teng Zhang for the continuous support of my Ph.D. study and research. His guidance helped me in all the time of research and writing of this thesis. His patience, motivation, enthusiasm, and immense knowledge encourage me to follow his example.

I would also like to express my gratitude to the rest of my defense committee: Prof. John Dannenhoffer, Prof. Alan Levy, Prof. Joseph Paulsen, Prof. Zhao Qin, and Prof. Wanliang Shan, for serving in my committee and overcoming all the difficulties and inconvenience in holding a defense through an online meeting.

I thank my research colleagues, Prof. Halim Kusumaatmaja, Prof. Joseph Paulsen, Prof. Benny Davidovitch, Prof. Xueju Wang, Dr. Jack Panter, Mr. Sam Avis, and Mr. Yi Li, for their valuable discussions and important theoretical, experimental and simulation works.

Finally, I am extremely grateful to my parents for their love, caring, and sacrifices for educating and preparing me for my future.

Table of Contents

List of Figures

List of Tables

List of Boxes

Chapter 1: Introduction

1.1 Morphological instabilities of thin solids in nature and engineered structures

Confined thin solids (e.g. thin rods, shells, and sheets) are prone to lose stability to relieve the compression energy. Stability analysis of thin solids began with Euler's solution of buckling of an elastic column [1] and has matured to become not only a fundamental problem in solid mechanics [2]. It is also crucially important to ensure the safety of structures against collapses in disciplines such as structural engineering, aerospace engineering, and nuclear engineering [3]. A detailed overview of this subject can be found in the seminal book by Bazant and Cedolin [4]. From this perspective, buckling has traditionally been regarded as an unfavorable phenomenon that should be avoided through special design modifications -- an approach that can be referred to as *Buckliphobia* [5]. By contrast, with the increasing use of extremely deformable materials and structures [5,6], *Buckliphilia* [5] is a more recent emerging trend that is changing the above paradigm, in which the buckling of thin solids is considered as an opportunity for novel functionality that enables a broad range of emerging technologies. Such applications include soft robotics actuators [7], mechanical metamaterials [8], morphable 3D microelectronic devices [9], deployable space structures [10], energy harvesting, or dissipation devices [11,12], and adaptive aerodynamic drag control [13].

As the study of pattern formation is gaining increasing prominence in the physics community, morphological instabilities in thin solids have also emerged rapidly as canonical problems to investigate how geometry can couple with nonlinearities to produce intricate patterns from featureless systems. One of the prototypical systems is the formation of wrinkle patterns on thin

sheets under a broad range of conditions such as boundary loads [14], incompatible topographical constraints [15-17], differential swelling [18], expansion on soft substrates [19,20], and growth in confined spaces [21,22].

Morphological instabilities in thin solids also play significant roles in explaining the morphogenesis process, one fundamental aspect of developmental biology, in which initially flat sheets of cells are transformed into complex three-dimensional structures of mature organs during embryonic development [23]. For example, the cerebral cortex of the mammalian brain forms folds because the cortical plate grows more quickly than the tissue beneath it, thereby causing the outer surface to buckle [24]; the initially straight intestinal tube forms the looping structure of the gut because the gut tube grows in length faster than does the mesentery to which it is attached, thereby causing compression in the tube and induce it to buckle [25].

1.2 Numerical methods for simulating instabilities in thin solids

The large displacements and rotations often associated with buckling of thin solids can yield non-negligible geometric nonlinearities, even if their material properties remain linear elastic, especially in the post-buckling regimes for the Buckliphilia approach. These nonlinearities, coupled with complex geometries encountered in various problems, pose challenges in deriving closed analytical solutions. This highlights the important role of numerical methods in the study of instabilities in thin solids. The simulations in this dissertation will be performed using two methods: the finite element method and discrete shell models. Here, we make a brief introduction to these two methods.

The finite element method is usually the preferred numerical methods for modeling complex solid mechanics problems, due to its ability to model complex geometries and the maturity of its

software development. For instance, commercial finite element packages have been used to analyze multistable structures [26-28]. However, in problems where there are a large number of similar post-buckling equilibrium states, the quasi-static implicit solvers implemented in those packages exhibit poor convergence, and the results tend to be trapped into one of many metastable states (local energy minima) if they are obtained [29] unless the appropriate buckling modes are known a priori and used as the imperfections. For most real applications, such an approach is cumbersome and requires user intervention, such that it becomes difficult and inefficient to explore the entire nonlinear space.

The discrete models based on discrete differential geometry have been widely used in the computer graphics community for simulating thin solids ranging from paper to metals [30-33]. The simplicity and efficiency of these models make them suitable for implementation in open source software or integration with existing algorithms, which are recent trends for modeling the instabilities of thin solids coupled with other phenomena, such as fluid-structure interactions [34], fracture [35], electromagnetic effects and growth. On the other hand, unlike the finite element method, these models suffer from problems such as mesh-dependent behaviors [32] and the effects of negative Poisson's ratio [36].

1.3 Outline of the dissertation

Chapter 1 provides an overview of various phenomena observed in nature and engineering applications related to the instabilities in thin solids. We also briefly discuss the numerical methods we will use in this thesis for simulating instabilities in thin solids.

Chapter 2 compares the performance of three widely used discrete shell models for a few benchmark problems in thin-film mechanics and use this as guidance to our simulations in the following chapters.

Chapter 3 demonstrates how the energy landscapes for shell buckling can be comprehensively surveyed by combing a simple discrete shell model with efficient energy minimization and pathfinding algorithms. We then apply our methods to two prototypical examples: spherical cap and cylindrical cap buckling.

Chapter 4 addresses the wrinkling phenomena characterized by a uniform wavelength and radially distributed wrinkles separately by a defect-rich buffer zone, by analyzing the wrinkle pattern on an annular sheet under tensile loads.

Chapter 5 includes some concluding remarks and future directions of study.

Chapter 2: Discrete Thin Shell Models

2.1 Introduction

Many problems in engineering and physics require accurate and efficient simulations of the deformation of shells. In these simulations, it is often necessary to represent deformed shells by meshes and approximate their strain energy as functions of unknown displacements at nodal points. The number of degrees of freedom (DOF) at each node can be 3 (translational only) or 5 (translational and rotational), depending on the kinematics assumptions. In classical shell theories [67] one has to distinguish between thick shells ($R/t < 20$) and thin shells ($R/t > 20$). In thick shell theories, transverse shear deformations are taken into account, and both translational and rotational DOF's are required in simulations; whereas in thin shell theories, transverse shear deformations are assumed to be negligible, and only translational DOF's are required.

Finite element methods based on thick shell theories [37] are most common in engineering applications, because in the presence of both translational and rotational DOF only C^0 continuity is required between elements which allows the use of very simple shape functions. However, the rotational DOF's often cause convergence difficulties and shear-locking [38,39]. Mixed formulations and special finite element function spaces are required to alleviate these problems, but resulting in more complex models [39-47].

On the other hand, simple and efficient discrete thin shell models based on discrete differential geometry, which involve only translational DOF as unknowns, are often used in computer graphics [47]. Unfortunately, some of these models lack the convergence of finite element methods, leading to mesh-dependent behaviors [47].

This chapter reports our implementation of the discrete shell models in molecular dynamics code LAMMPS, as well as their performance on several benchmark problems. This chapter is organized as follows. Section 2.2 reviews the kinematics description of shells and continuum elastic energy formulations based on Koiter's theory for a thin elastic shell. Section 2.3 derives three energy discretization formulations on triangular meshes. Section 2.4 describes the implementation details of the discrete shell models in molecular dynamics code LAMMPS. Section 2.5 tests the mesh dependency behaviors and accuracies of the three models after performing a series of benchmark tests. Section 2.6 concludes this chapter with some discussions of the results.

2.2 Elastic energy of a continuum thin shell

The elastic energy of a thin elastic shell can be described as a sum of a "membrane" term and a "bending" term, which depend, respectively, on the strain and curvature of the mid-plane. For a thin shell of thickness t made of elastic materials of Young modulus E, these two energies are proportional, respectively, to the stretching modulus ($Y \sim Et$) and bending modulus ($B \sim Et^3$). Among thin shell theories that that account for both membrane and bending terms, Ciarlet [48] advocated Koiter's nonlinear shell theory [49] as the best model in both the membrane-dominated and bending-dominated regimes in the case of linear elastic deformations. Steigmann [50] showed that Koiter's theory is the leading-order energy in the intermediate regime where bending and stretching deformation energies are assumed to be of comparable importance.

Here, I briefly summarize Koiter's theory for a thin elastic shell, which is based on the following kinematics assumptions [51]: (i) the normal lines to the middle surface in the reference configuration are deformed into normal lines to the middle surface in the current configuration (the unshearable assumption), (ii) the distances along the normal lines are preserved (the normal

inextensibility assumption). These two assumptions imply that the deformation of the middle surface completely describes the deformation at any point of the shell. Therefore, in the following discussions, we will represent a shell by its middle surface.

We describe the middle surface of a shell in undeformed and deformed states using parametric representation:

$$\mathbf{r}_0 = \boldsymbol{\phi}_0(u, v) \tag{2.1}$$

$$\mathbf{r} = \boldsymbol{\phi}(u, v) \tag{2.2}$$

where $(u, v) \in \omega \subset \mathbb{R}^2$ are curvilinear coordinates, $\boldsymbol{\phi}_0, \boldsymbol{\phi} : \omega \to \mathbb{R}^3$ are regular surfaces, $\mathbf{r}_0$ and $\mathbf{r}$ correspond to the material points on the undeformed and deformed middle surfaces. The above parametric representation completely describes the kinematics of the shell:

$$\mathbf{r} = \boldsymbol{\phi}\boldsymbol{\phi}_0^{-1}(\mathbf{r}_0) = \mathbf{F}(\mathbf{r}_0) \tag{2.3}$$

in which $\mathbf{F} = \boldsymbol{\phi}\boldsymbol{\phi}_0^{-1}$ is the deformation function.

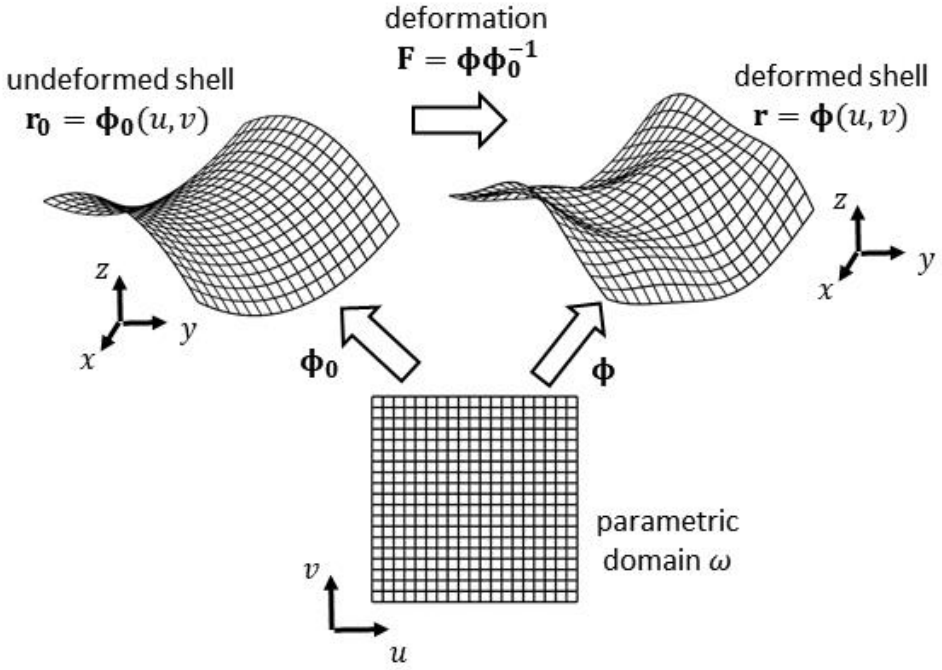

Figure 2.1 Parametric representation of the middle surface of a shell in undeformed and deformed states

The normal vectors of the middle surfaces are given by:

$$\mathbf{n}_0 = \frac{\partial_u \boldsymbol{\phi}_0 \times \partial_v \boldsymbol{\phi}_0}{\|\partial_u \boldsymbol{\phi}_0 \times \partial_v \boldsymbol{\phi}_0\|} \tag{2.4}$$

$$\mathbf{n} = \frac{\partial_u \boldsymbol{\phi} \times \partial_v \boldsymbol{\phi}}{\|\partial_u \boldsymbol{\phi} \times \partial_v \boldsymbol{\phi}\|} \tag{2.5}$$

where $\partial_u(\cdot)$ and $\partial_v(\cdot)$ are partial derivatives with respect to curvilinear coordinates u and v, $\times$ is the vector cross product. The geometry of the middle surface is completely described by the second-order metric ($\mathbf{a}_0$, **a)** and curvature ($\mathbf{b}_0$, **b**) tensors, whose components are computed as:

$$\mathbf{a_0} = \boldsymbol{\nabla}\boldsymbol{\phi}_0{}^{\mathrm{T}}\boldsymbol{\nabla}\boldsymbol{\phi}_0 \tag{2.6}$$

$$\mathbf{a} = \boldsymbol{\nabla}\boldsymbol{\phi}^{\mathrm{T}}\boldsymbol{\nabla}\boldsymbol{\phi} \tag{2.7}$$

$$\mathbf{b}_0 = -\frac{1}{2}(\boldsymbol{\nabla}\boldsymbol{\phi}_0^{\mathrm{T}}\boldsymbol{\nabla}\mathbf{n} + \boldsymbol{\nabla}\mathbf{n}^{\mathrm{T}}\boldsymbol{\nabla}\boldsymbol{\phi}_0) \tag{2.8}$$

$$\mathbf{b} = -\frac{1}{2}(\boldsymbol{\nabla}\boldsymbol{\phi}^{\mathbf{T}}\boldsymbol{\nabla}\mathbf{n} + \boldsymbol{\nabla}\mathbf{n}^{\mathrm{T}}\boldsymbol{\nabla}\boldsymbol{\phi}) \tag{2.9}$$

where $\boldsymbol{\nabla} = (\partial_u, \partial_v)$ is the gradient with respect to curvilinear coordinates (u, v). We use the following measures of deformation for the middle surface [16-18]:

$$\boldsymbol{\varepsilon} = \frac{1}{2}(\mathbf{a} - \mathbf{a}_0) \tag{2.10}$$

$$\boldsymbol{\kappa} = \mathbf{b} - \mathbf{b}_0 \tag{2.11}$$

where $\boldsymbol{\varepsilon}$ is the membrane strain tensor and $\boldsymbol{\kappa}$ is the bending strain tensor.

In Koiter's theory, the elastic energy density W is expressed as a sum of membrane energy W_m and bending energy W_b [49,50,55,56]:

$$W = W_m + W_b \tag{2.12}$$

$$W_m = \frac{Et}{8(1-\nu^2)}[\nu \,\mathrm{tr}(\boldsymbol{\varepsilon}^2) + (1-\nu)\,(\mathrm{tr}\boldsymbol{\varepsilon})^2] \tag{2.13}$$

$$W_b = \frac{Et^3}{24(1-\nu^2)}[\nu \,\mathrm{tr}(\boldsymbol{\kappa}^2) + (1-\nu)\,(\mathrm{tr}\boldsymbol{\kappa})^2] \tag{2.14}$$

where E is Young's modulus, ν is Poisson's ratio and t is shell thickness.

2.3 Elastic energy of a discrete thin shell

In the previous section, the membrane and bending strain tensors are both expressed in differential forms. In this section, we briefly review their discrete forms on a general triangular mesh. A variety of different discretizations of the bending strain tensor have been developed in engineering, physics, and computer graphics. Here, we compare three commonly used models: hinge model, triangle-averaged model, and quadratic fit model. We then derive the corresponding discrete membrane and bending energy of the three models. In the following, all the upper-case Roman letters or Greek letters with bar will denote quantities in the undeformed state, and all the lower-case Roman letters or Greek letters without bar will denote quantities in the deformed state.

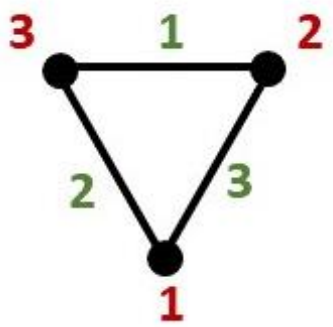

Figure 2.2 Numbering of vertices (red numbers) and edges (green numbers) in the computation of discrete membrane energy

2.3.1 Discrete membrane energy

Consider an arbitrary triangle within a triangular mesh, as shown in Figure 2.2. Let $\mathbf{X}_i$ be the coordinate vector of vertex i of the undeformed mesh and $\mathbf{V}_{ij}$ be the vector defined as

$$\mathbf{V}_{ij} = \mathbf{X}_i - \mathbf{X}_j \tag{2.15}$$

The outward unit normal vector of the triangle is

$$\mathbf{N} = \frac{\mathbf{V}_{21} \times \mathbf{V}_{32}}{\|\mathbf{V}_{21} \times \mathbf{V}_{32}\|} \tag{2.16}$$

Let $\mathbf{T}_i$ be the vector in the plane perpendicular to edge i having the same length as edge i, i.e.

$$\mathbf{T}_1 = \mathbf{V}_{32} \times \mathbf{N} \tag{2.17}$$

$$\mathbf{T}_2 = \mathbf{V}_{13} \times \mathbf{N} \tag{2.18}$$

$$\mathbf{T}_3 = \mathbf{V}_{21} \times \mathbf{N} \tag{2.19}$$

We use the following approximation for membrane strain on each triangle [57,58]:

$$\boldsymbol{\varepsilon} = \frac{1}{16A^2}(l_i^2 - L_i^2)\varepsilon_{ijk}^2 \mathbf{T}_j \otimes \mathbf{T}_k \tag{2.20}$$

where L_i and l_i are the undeformed and deformed lengths of edge i, and A is the triangular area. In the above equation, the alternating symbol ε_{ijk} is defined by

$$\varepsilon_{ijk} = \begin{cases} 1 & \text{if } \{i,j,k\} = \{1,2,3\}, \{2,3,1\} \text{ or } \{3,1,2\} \\ -1 & \text{if } \{i,j,k\} = \{2,1,3\}, \{1,3,2\} \text{ or } \{3,2,1\} \\ 0 & \text{if an index is repeated} \end{cases} \tag{2.21}$$

and the Einstein summation convention will be employed according to which summation over the range 1, 2, 3 is implied for any index that is repeated twice in any term, so that, for instance

$$u_i v_i = u_1 v_1 + u_2 v_2 + u_3 v_3 \tag{2.22}$$

$$S_{ij} u_i v_j = S_{1j} u_1 v_j + S_{2j} u_2 v_j + S_{3j} u_3 v_j \tag{2.23}$$

$$S_{ijk} u_i v_j w_k = S_{1jk} u_1 v_j w_k + S_{2jk} u_2 v_j w_k + S_{3jk} u_3 v_j w_k \tag{2.24}$$

Using the properties of the alternating symbol ε_{ijk} and cross product $\otimes$, some algebraic manipulations of $\boldsymbol{\varepsilon}$ in equation (2.20) yields

$$\boldsymbol{\varepsilon}^2 = \frac{1}{256A^2} s_i s_p \varepsilon_{ijk}^2 \varepsilon_{pqr}^2 (\mathbf{T}_k \cdot \mathbf{T}_q)(\mathbf{T}_j \otimes \mathbf{T}_r) \tag{2.25}$$

$$\mathrm{tr}(\boldsymbol{\varepsilon}^2) = \frac{1}{256A^4} s_i s_p \varepsilon_{ijk}^2 \varepsilon_{pqr}^2 (\mathbf{T}_k \cdot \mathbf{T}_q)(\mathbf{T}_j \cdot \mathbf{T}_r) \tag{2.26}$$

$$\mathrm{tr}\boldsymbol{\varepsilon} = \frac{1}{16A^2} s_i \varepsilon_{ijk}^2 (\mathbf{T}_j \cdot \mathbf{T}_k) \tag{2.27}$$

$$(\mathrm{tr}\boldsymbol{\varepsilon})^2 = \frac{1}{256A^4} s_i s_p \varepsilon_{ijk}^2 \varepsilon_{pqr}^2 (\mathbf{T}_j \cdot \mathbf{T}_k)(\mathbf{T}_q \cdot \mathbf{T}_r) \tag{2.28}$$

where $s_i = l_i^2 - L_i^2$. Substituting Equations (2.25-2.28) into Equation (2.13) for W_m and considering the relation $E_m = W_m A$ gives the following discretized form of membrane energy:

$$E_m = \frac{A}{2} a_{ip} s_i s_p \tag{2.29}$$

where

$$a_{ij} = \frac{Et}{128(1-\nu^2)A^4} a_{ij}^* \tag{2.30}$$

$$a_{11}^* = (\nu+1)(\mathbf{T}_2 \cdot \mathbf{T}_3)^2 - (\nu-1)(\mathbf{T}_2 \cdot \mathbf{T}_2)(\mathbf{T}_3 \cdot \mathbf{T}_3) \tag{2.31}$$

$$a_{22}^* = (\nu+1)(\mathbf{T}_1 \cdot \mathbf{T}_3)^2 - (\nu-1)(\mathbf{T}_1 \cdot \mathbf{T}_1)(\mathbf{T}_3 \cdot \mathbf{T}_3) \tag{2.32}$$

$$a_{33}^* = (\nu+1)(\mathbf{T}_1 \cdot \mathbf{T}_2)^2 - (\nu-1)(\mathbf{T}_1 \cdot \mathbf{T}_1)(\mathbf{T}_2 \cdot \mathbf{T}_2) \tag{2.33}$$

$$a_{12}^* = (\nu+1)(\mathbf{T}_1 \cdot \mathbf{T}_3)(\mathbf{T}_2 \cdot \mathbf{T}_3) - (\nu-1)(\mathbf{T}_1 \cdot \mathbf{T}_2)(\mathbf{T}_2 \cdot \mathbf{T}_3) \tag{2.34}$$

$$a_{13}^* = (\nu+1)(\mathbf{T}_1 \cdot \mathbf{T}_2)(\mathbf{T}_2 \cdot \mathbf{T}_3) - (\nu-1)(\mathbf{T}_1 \cdot \mathbf{T}_3)(\mathbf{T}_2 \cdot \mathbf{T}_2) \tag{2.35}$$

$$a_{23}^* = (\nu+1)(\mathbf{T}_1 \cdot \mathbf{T}_2)(\mathbf{T}_1 \cdot \mathbf{T}_3) - (\nu-1)(\mathbf{T}_1 \cdot \mathbf{T}_1)(\mathbf{T}_2 \cdot \mathbf{T}_3) \tag{2.36}$$

In equation (2.29), coefficients a_{ip} depends only on the quantities related to the undeformed mesh. Hence at each time step, we only evaluate edge length change $s_i = l_i^2 - L_i^2$.

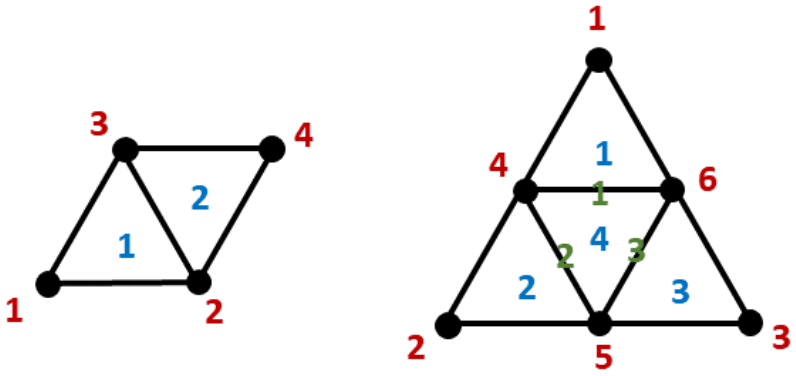

Figure 2.3 Numbering of vertices (red numbers), edges (green numbers), and triangles (blue numbers) in the computation of discrete bending energy. (left) Hinge model (right) Triangle-averaged and quadratic fit models

2.3.2 Discrete bending energy

2.3.2.1 Hinge model

The first model has been used in cloth (computer graphics) and membrane (physics) simulations [59-61]. It assumes that the bending strain tensor is concentrated at the hinge connecting two adjacent triangles (Figure 2.3a). Let $\mathbf{N}_i$ be the outward unit normal vector of triangle i:

$$\mathbf{N}_1 = \frac{\mathbf{V}_{21} \times \mathbf{V}_{32}}{\|\mathbf{V}_{21} \times \mathbf{V}_{32}\|} \tag{2.37}$$

$$\mathbf{N}_2 = \frac{\mathbf{V}_{42} \times \mathbf{V}_{34}}{\|\mathbf{V}_{42} \times \mathbf{V}_{34}\|} \tag{2.38}$$

and $\mathbf{T}$ be the vector perpendicular to the central edge:

$$\mathbf{T} = \mathbf{V}_{32} \times \mathbf{N}_1 \tag{2.39}$$

The hinge angle $\bar{\theta}$ is defined as the angle between two unit normal vectors:

$$\bar{\theta} = \text{acos}(\mathbf{N}_1 \cdot \mathbf{N}_1) \tag{2.40}$$

The bending strain tensor on the hinge is approximated as

$$\boldsymbol{\kappa} = \frac{\theta - \bar{\theta}}{(A_1 + A_2)L}\mathbf{T}\otimes\mathbf{T} \tag{2.41}$$

where A_1 and A_2 are triangular areas, and L is the length of the hinge edge.

Applying Equation (2.41) to Equation (2.14) and considering the area each hinge occupies, the bending energy of each hinge is computed as

$$E_b = \frac{6(1-\nu^2)L^2(\theta - \bar{\theta})^2}{Et^3(A_1 + A_2)} \tag{2.42}$$

Using the approximation $1 - \cos(\theta - \bar{\theta}) \approx (\theta - \bar{\theta})^2/2$, Equation (2.42) can be expressed the alternative form:

$$E_b = k[1 - \cos(\theta - \bar{\theta})] \tag{2.43}$$

where

$$k = \frac{12(1-\nu^2)L^2}{Et^3(A_1 + A_2)} \tag{2.44}$$

In Equations (2.43) and (2.44), all quantities except θ depend only on the quantities of the undeformed configuration, hence at every time step we reevaluate only θ.

2.3.2.2 Triangle-averaged model

The bending strain tensor in this model is approximated by averaging the contributions of three triangular hinges (edges 1-3 in Figure 2.3b). Its expression is [47,57]

$$\boldsymbol{\kappa} = \frac{\theta_i - \bar{\theta}_i}{2AL_i}\mathbf{T}_i\otimes\mathbf{T}_i \tag{2.45}$$

where θ_i, $\bar{\theta}_i$, $\mathbf{T}_i$, L_i are defined in the same way as in the hinge model, and A is the area of the triangle in the center.

Using the properties of the cross product $\otimes$, we have

$$\boldsymbol{\kappa}^2 = \frac{(\theta_i - \bar{\theta}_i)(\theta_j - \bar{\theta}_j)}{4A^2 L_i L_j}(\mathbf{T}_i \cdot \mathbf{T}_j)(\mathbf{T}_i \otimes \mathbf{T}_j) \tag{2.46}$$

$$\mathrm{tr}(\boldsymbol{\kappa}^2) = \frac{(\theta_i - \bar{\theta}_i)\left(\theta_j - \bar{\theta}_j\right)}{4A^2 L_i L_j}\left(\mathbf{T}_i \cdot \mathbf{T}_j\right)^2 \tag{2.47}$$

$$\mathrm{tr}\boldsymbol{\kappa} = \frac{\theta_i - \bar{\theta}_i}{2AL_i}(\mathbf{T}_i \cdot \mathbf{T}_i) = \frac{(\theta_i - \bar{\theta}_i)L_i}{2A} \tag{2.48}$$

$$(\mathrm{tr}\boldsymbol{\kappa})^2 = \frac{[(\theta_i - \bar{\theta}_i)L_i]^2}{4A^2} \tag{2.49}$$

Substituting Equations (2.46-2.49) into Equation (2.14) for W_b and considering the relation $E_b = W_b A$ gives the following equation for discrete bending energy:

$$E_b = \frac{1}{4}\left[\alpha\left((\theta_i - \bar{\theta}_i)L_i\right)^2 + \beta\frac{(\theta_i - \bar{\theta}_i)\left(\theta_j - \bar{\theta}_j\right)}{L_i L_j}T_{ij}^2\right] \tag{2.50}$$

where

$$\alpha = \frac{Et^3\nu}{24(1-\nu^2)} \tag{2.51}$$

$$\beta = \frac{Et^3}{24(1+\nu)} \tag{2.52}$$

$$T_{ij} = \mathbf{T}_i \cdot \mathbf{T}_j \tag{2.53}$$

2.3.2.3 Quadratic fit model

This model approximates the bending strain tensor of a given triangle by fitting the coordinates of the six vertices of its three neighboring triangles (shown in Figure 2.3b) with a quadratic function [62-64]. We begin by constructing a local orthonormal basis $\{\mathbf{E}_u, \mathbf{E}_v, \mathbf{N}\}$ on the undeformed mesh:

$$\mathbf{E}_u = \frac{\mathbf{V}_{21}}{\|\mathbf{V}_{21}\|} \tag{2.54}$$

$$\mathbf{N} = \frac{\mathbf{V}_{21} \times \mathbf{V}_{32}}{\|\mathbf{V}_{21} \times \mathbf{V}_{32}\|} \tag{2.55}$$

$$\mathbf{E}_v = \mathbf{N} \times \mathbf{E}_u \tag{2.56}$$

The local coordinates of the six vertices $(\mathrm{U}_i, \mathrm{V}_i, \mathrm{W}_i)(i = 1, \dots 6)$ are given by:

$$\mathrm{U}_i = \mathbf{V}_{i1} \cdot \mathbf{E}_u \tag{2.57}$$

$$\mathrm{V}_i = \mathbf{V}_{i1} \cdot \mathbf{E}_v \tag{2.58}$$

$$\mathrm{W}_i = \mathbf{V}_{i1} \cdot \mathbf{N} \tag{2.59}$$

where $\mathrm{W}_4 = \mathrm{W}_5 = \mathrm{W}_6 = 0$ since the triangle in the center is lying on the $\mathbf{E}_u - \mathbf{E}_v$ plane. The coordinates of the six vertices are then fitted to the following quadratic function [62-64]:

$$W_i = A_1 + A_2 U_i + A_3 V_i + A_4 U_i^2 + A_5 U_i V_i + A_6 V_i^2 \ (i = 1,2, \dots 6) \tag{2.60}$$

Solving the above system of linear equations for the unknown coefficients A_i $(i = 1, \dots 6)$ we have

$$A_1 = A_2 = A_3 = 0 \tag{2.61}$$

$$A_i = C_{ij} W_j \approx C_{ij} D_j \bar{\theta}_j \ (i = 4,5,6; j = 1,2,3) \tag{2.62}$$

where C_{ij} are coefficients depending on $(\mathrm{U}_i, \mathrm{V}_i)$, D_j are the height of triangle j, and $\bar{\theta}_j$ are the hinge angles of edge i. Similarly, the quadratic function that fits the coordinates of the six vertices on the deformed mesh are:

$$w_i = a_1 + a_2 u_i + a_3 v_i + a_4 u_i^2 + a_5 u_i v_i + a_6 v_i^2 \ (i = 1,2, \dots 6) \tag{2.63}$$

with its coefficients given by

$$a_1 = a_2 = a_3 = 0 \tag{2.64}$$

$$a_i = C_{ij} w_j \approx C_{ij} D_j \theta_j \ (i = 4,5,6; j = 1,2,3) \tag{2.65}$$

The discrete bending strain tensor can be approximated as:

$$\boldsymbol{\kappa} = \begin{pmatrix} w_{uu} - W_{UU} & w_{uv} - W_{UV} \\ w_{uv} - W_{UV} & w_{vv} - W_{VV} \end{pmatrix} = \begin{pmatrix} 2(a_4 - A_4) & a_5 - A_5 \\ a_5 - A_5 & 2(a_6 - A_6) \end{pmatrix} \tag{2.66}$$

Substituting Equation (2.66) into Equation (2.14) for W_b and considering the relation $E_b = W_b A$ gives the following equation for discrete bending energy:

$$E_b = 4\alpha A[(a_4 - A_4) + (a_6 - A_6)]^2 + \beta[4(a_4 - A_4)^2 + 2(a_5 - A_5)^2 + 4(a_6 - A_6)^2] \tag{2.67}$$

where $a_4 \sim a_6$ are given in Equation (2.65) and α, β are given in Equation (2.51) and (2.52).

2.4 LAMMPS implementation of the discrete thin shell models

2.4.1 Overview of LAMMPS

LAMMPS [67] is an open-source molecular dynamics (MD) code that models the interactions and movements of particles governed by Newton's second law:

$$m_i \ddot{\mathbf{r}}_i = \mathbf{f}_i \tag{2.68}$$

where m_i is the mass, $\mathbf{r}_i$ is the Cartesian coordinate, and $\mathbf{f}_i$ is the interaction force acting on the ith particle. The force is determined by

$$\mathbf{f}_i = -\frac{\partial U}{\partial \mathbf{r}_i} \tag{2.69}$$

where U is the potential energy. In LAMMPS, a single particle can be an atom or molecule or electron, a coarse-grained cluster of atoms, or a mesoscopic or macroscopic clump of material.

There are several reasons for us to use LAMMPS. First, LAMMPS is robust and efficient which has been already validated by numerous benchmarks and publications. Second, LAMMPS

is an open-source code with clear documentation, which makes it easy to be modified or extended with new capabilities, such as user-defined potentials. Third, LAMMPS is designed for parallel computers, dramatically reducing the computational cost for large models.

In the following sections, we will describe the steps that should be followed for the implementation and usage of discrete shell models in LAMMPS, as illustrated in Figure 2.4.

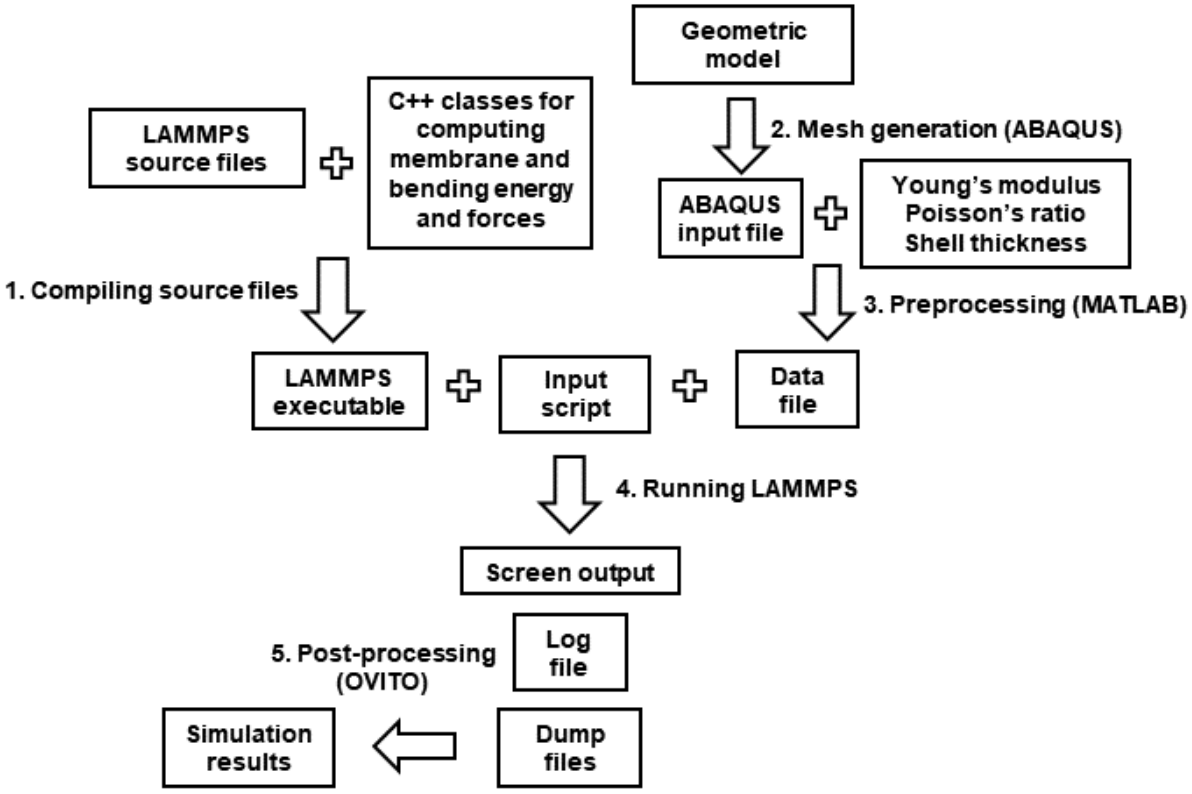

Figure 2.4 Flow chart of procedures to implement and use discrete shell models in LAMMPS

2.4.3 Compiling source files

LAMMPS is open-source and its source files available for download at its official website [71]. As LAMMPS is written in object-oriented C++ language, users can add new potentials by writing new C++ classes. We added four new classes:

```
angle_membrane
```

```
bond_bending_hinge
angle_bending_triangle
angle_bending_quadratic
```

which compute the elastic energy and corresponding forces (Appendix A) of the discrete shell models described in the previous section. These classes are written by modifying the source files of the built-in LAMMPS classes angle_harmonic and bond_harmonic. To compile LAMMPS, copy the source files of the new classes to the src directory, load the LAMMPS standard package

```
molecule
```

```
make yes-molecule
```

and build a parallel LAMMPS executable lmp_mpi by issuing

```
make mpi
```

in the src directory.

2.4.4 Mesh generation

We use finite element software ABAQUS to automatically generate unstructured 3-node elements (S3) on arbitrary shell surfaces. The ABAQUS input file (.inp), which contains nodal coordinates and element connectivity, will be read by a MATLAB code in the preprocessing step. Here is a sample ABAQUS input file:

```
...
*Node
1, 749.317322, 31.9929314, 0
2, 749.136047, 35.9891472, 0
3, 748.933411, 39.9843369, 0
...
*Element, type=S3
1, 6904, 1146, 1145
2, 7393, 1148, 1147
3, 10050, 8914, 8977
...
```

In the *Node section, the first column contains node ID and the next three columns are x, y, and z coordinates of the node. In the *Element section, the first column contains element ID and the next three columns contain the IDs of the three element nodes.

2.4.5 Preprocessing

I developed a MATLAB program for each discrete shell model in the preprocessing step. The program takes the name of the ABAQUS input file, Young's modulus, Poisson's ratio, and shell thickness as input parameters, and generates a LAMMPS data file which contains basic information about the size of the problem to be run, the initial atomic coordinates, molecular topology, and force-field coefficients. Here is a sample data file for the quadratic fit discrete shell model:

```
LAMMPS DATA FILE

525 atoms
832 angles

3 atom types
832 angle types

-0.2 6.2 xlo xhi
-0.2 0.4 ylo yhi
-2.0 2.0 zlo zhi

Masses

1 1
2 1
3 1

Angle Coeffs

1 membrane i1 i2 i3 A alpha beta Th1 Th2 Th3 T11 T22 T33 T12 T13 T23
2 membrane i1 i2 i3 A alpha beta Th1 Th2 Th3 T11 T22 T33 T12 T13 T23
3 membrane i1 i2 i3 A alpha beta Th1 Th2 Th3 T11 T22 T33 T12 T13 T23
...

Atoms

1 1 2 0.0577350269189626 0.1 0
2 2 1 0.0866025403784439 0.15 0
3 3 2 0.0577350269189626 0.2 0
...

Angles

1 1 277 278 272
2 2 62 68 63
3 3 302 307 308
```

In the Angle Coeffs section, the first column contains angle type No., followed by the name of angle style and the coefficients computed by the preprocessing MATLAB code. The meaning of each coefficient is listed in Tables 2.1–2.3.

Table 2.1 Coefficients for angle style membrane

i1	Global nodal ID of node 1
i2	Global nodal ID of node 2
i3	Global nodal ID of node 3
A	Undeformed triangular area A
L1	Undeformed edge length of edge 1 L_1
L2	Undeformed edge length of edge 2 L_2
L3	Undeformed edge length of edge 3 L_3
a11	Coefficient a_{11} defined in Equation (2.30)
a22	Coefficient a_{22} defined in Equation (2.30)
a33	Coefficient a_{33} defined in Equation (2.30)
a12	Coefficient a_{12} defined in Equation (2.30)
a13	Coefficient a_{13} defined in Equation (2.30)
a23	Coefficient a_{23} defined in Equation (2.30)

Table 2.2 Coefficients for bond style bending/hinge

k	Coefficient k in Equation (2.44)
Th	Undeformed hinge angle $\bar{\theta}$

Table 2.3 Coefficients for angle style bending/triangle/averaged

i1	Global nodal ID of node 1
i2	Global nodal ID of node 2

i3	Global nodal ID of node 3
A	Undeformed triangular area A
alpha	Coefficient α in Equation (2.51)
beta	Coefficient β in Equation (2.52)
Th1	Undeformed hinge angle $\bar{\theta}_1$
Th2	Undeformed hinge angle $\bar{\theta}_2$
Th3	Undeformed hinge angle $\bar{\theta}_3$
T11	Coefficient T_{11} defined in Equation (2.53)
T22	Coefficient T_{22} defined in Equation (2.53)
T33	Coefficient T_{33} defined in Equation (2.53)
T12	Coefficient T_{12} defined in Equation (2.53)
T13	Coefficient T_{13} defined in Equation (2.53)
T23	Coefficient T_{23} defined in Equation (2.53)

Table 2.4 Coefficients for angle style bending/quadratic/fit

i1	Global nodal ID of node 1
i2	Global nodal ID of node 2
i3	Global nodal ID of node 3
A	Undeformed triangular area A
alpha	Coefficient α in Equation (2.51)
beta	Coefficient β in Equation (2.52)
Th1	Undeformed hinge angle $\bar{\theta}_1$
Th2	Undeformed hinge angle $\bar{\theta}_2$
Th3	Undeformed hinge angle $\bar{\theta}_3$
D1	Undeformed height of triangular 1 D_1
D2	Undeformed height of triangular 2 D_2
D3	Undeformed height of triangular 3 D_3

C44	Coefficient C_{44} defined in Equation (2.62)
C55	Coefficient C_{55} defined in Equation (2.62)
C66	Coefficient C_{66} defined in Equation (2.62)
C45	Coefficient C_{45} defined in Equation (2.62)
C46	Coefficient C_{46} defined in Equation (2.62)
C56	Coefficient C_{56} defined in Equation (2.62)

2.4.6 Running LAMMPS

LAMMPS executes by reading commands from an input script and data from the data file. Here is an example input script for cantilever beam test (Figure 2.8) using the quadratic fit discrete shell model:

```
units metal
dimension 3
boundary f f f
newton on
processors * * 1

atom_style molecular
angle_style hybrid membrane bending/quadratic/fit

read_data rect-a1000-b100-h5-square.lam

comm_style brick
atom_modify sort 1000 2.0
comm_modify mode single cutoff 15
neigh_modify once yes
balance 1.1 rcb

group other type 1
group lb type 2
group rb type 3

variable nrb equal count(rb)
variable f equal -1000/${nrb}

fix 1 all nve
fix 2 all langevin 0 0 0.01 9042970
fix 3 lb setforce 0 0 0
fix 4 rb addforce 0 0 ${f}

compute disp rb displace/atom
```

```
compute zmin rb reduce min c_disp[3]
compute zmax rb reduce max c_disp[3]

timestep 1e-6
thermo 10000
thermo_style custom step temp ke pe etotal fmax fnorm c_zmin c_zmax
thermo_modify lost ignore flush yes
thermo_modify format float %20.10g

dump 1 all custom 100000 dump/*.xyz id type x y z
dump_modify 1 format float %20.10g

run 20000000
```

2.5 Validation tests

2.5.1 Mesh dependency tests

While it is hard to expect the solution of a discrete problem to be entirely independent of the choice of mesh, it is reasonable to require that these dependencies vanish for sufficiently fine meshes. In this section, we test the mesh dependency of the three discrete thin shell models by applying them to several benchmark problems on three types of triangular mesh shown in Figure 2.5.

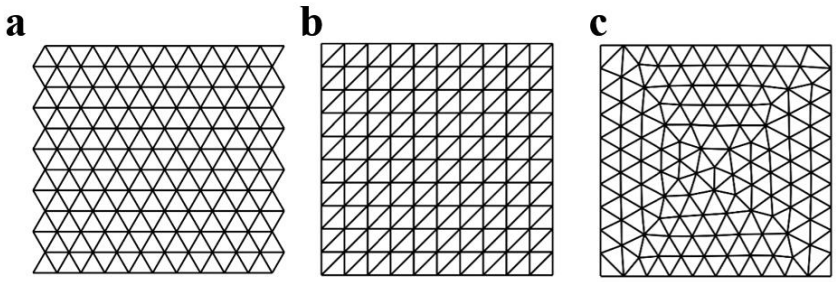

Figure 2.5 Mesh types used in our tests. (a) Equilateral (b) Regular (c) Irregular

In Figures 2.6 and 2.7, we compute the discrete bending energy of an initially flat thin square plate under two prescribed out-of-plane deformation modes (see Figures 2.6a and 2.7a for detailed descriptions) with increasingly fine meshes. We can observe from the deformed shapes (shown in exaggerated scales in Figures 2.6a and 2.67) that, the first mode has nonzero curvature

in the x direction and zero curvature in the y direction (or zero Gaussian curvature), while the second mode has nonzero curvatures in both directions (or nonzero Gaussian curvature). These two tests aim to evaluate the discrete shell models' performance in cases of zero or nonzero Gaussian curvatures.

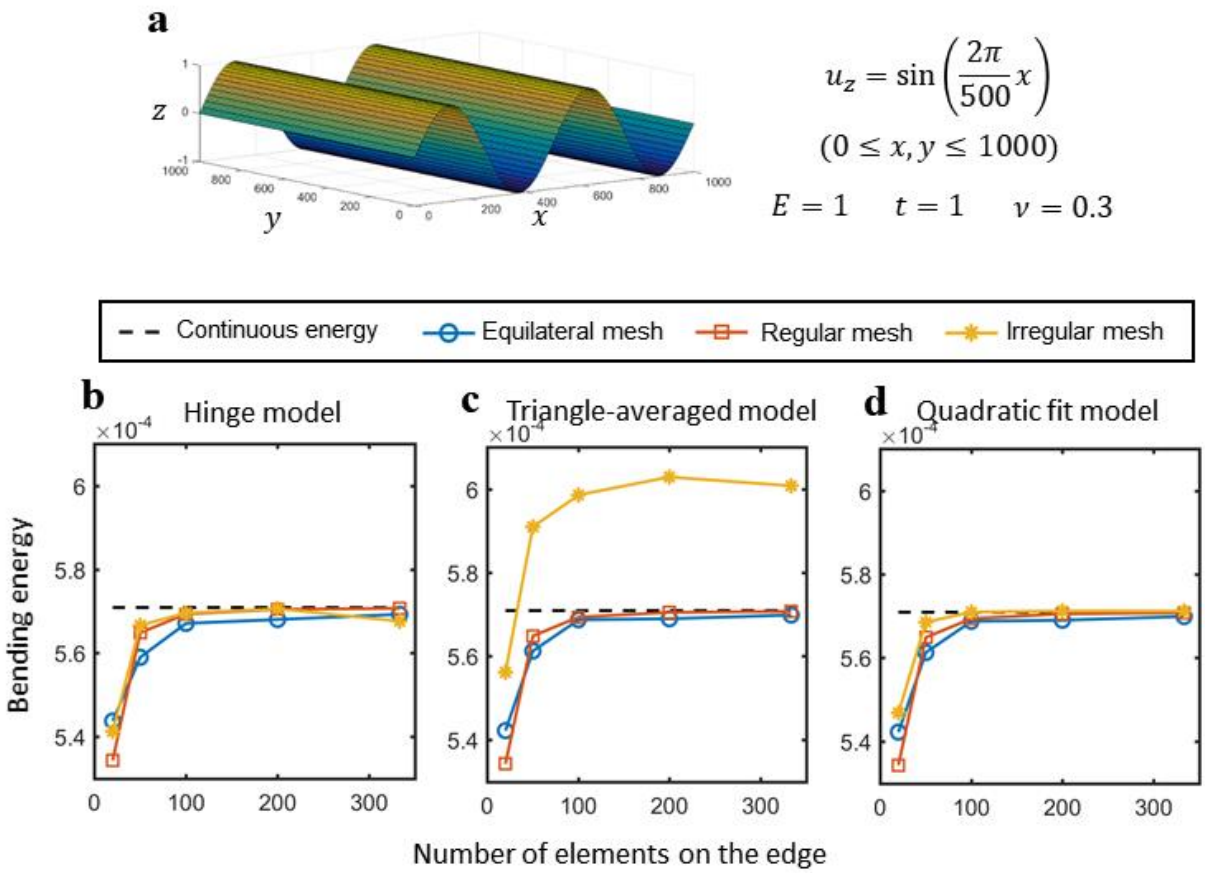

Figure 2.6 (a) An initially flat thin square plate under a prescribed out-of-plane deformation $u_z = \sin(2\pi/500x)$. (b-d) Convergence behaviors of discrete bending energy on a sequence of increasingly fine meshes compared to continuous bending energy for different discrete shell models and mesh types.

Figures 2.6b-d plot the convergence behaviors of discrete bending energy on a sequence of increasingly fine meshes for the first deformation mode. We observe that the hinge and quadratic

fit models converge to the continuous energy on all mesh types, and the triangle-averaged model is only convergent on equilateral and regular meshes.

Figures 2.7b-d plot the convergence behaviors for the second deformation mode. We observe that the quadratic fit model is the only model that converges to the continuous energy on all mesh types. The hinge model is only convergent on equilateral mesh and the triangle-averaged model is only convergent on equilateral and regular meshes.

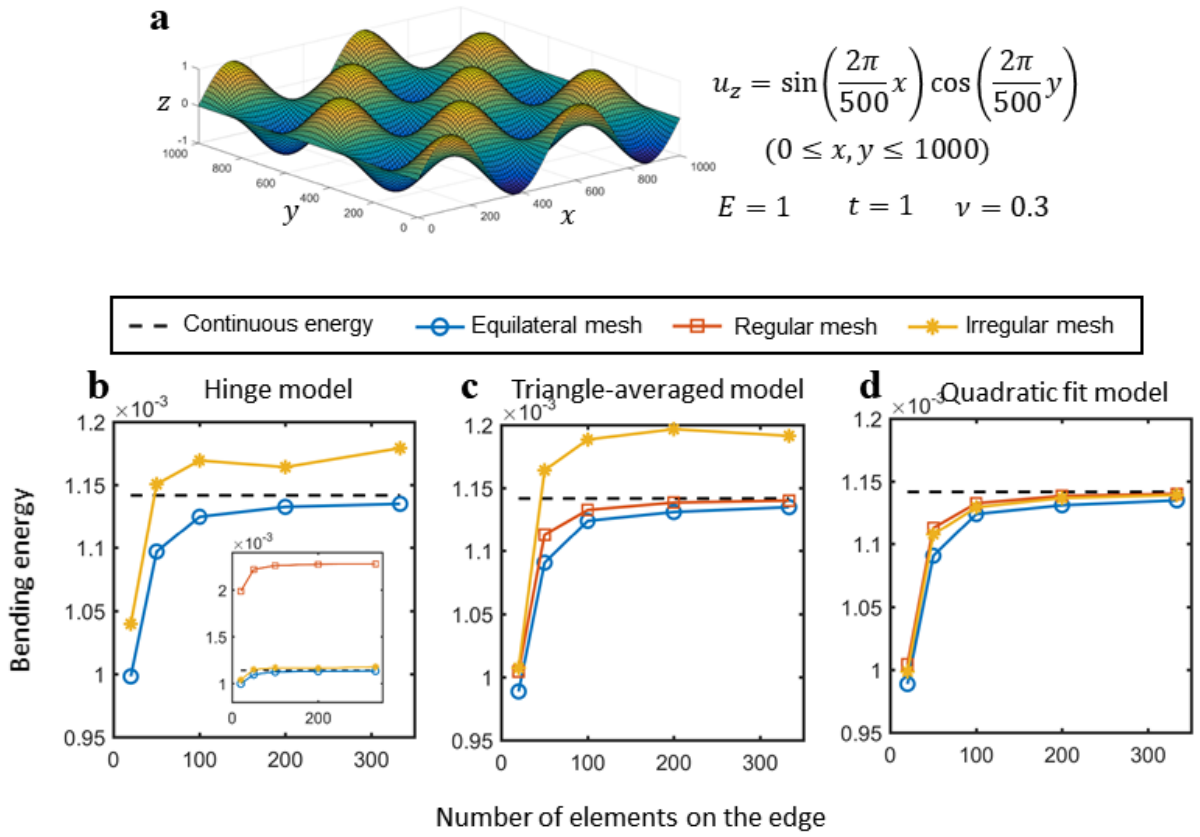

Figure 2.7 (a) An initially flat thin square plate under a prescribed out-of-plane deformation $u_z = \sin(2\pi/500x)\cos(2\pi/500y)$. (b-d) Convergence of discrete bending energy on a sequence of increasingly fine meshes compared to continuous bending energy for different discrete shell models and mesh types.

Cantilever beam tests have been used in shell finite element method to evaluate element sensitivity to various deformation patterns [65,66]. Here we use similar setups in which a rectangular piece of a thin plate fixed at one end is subjected to a distributed line load or a twisting couple at the other end (see Figures 2.8a and 2.9a for detailed descriptions). These two tests aim to evaluate the discrete shell models' performance in the situations of bending and twisting deformations.

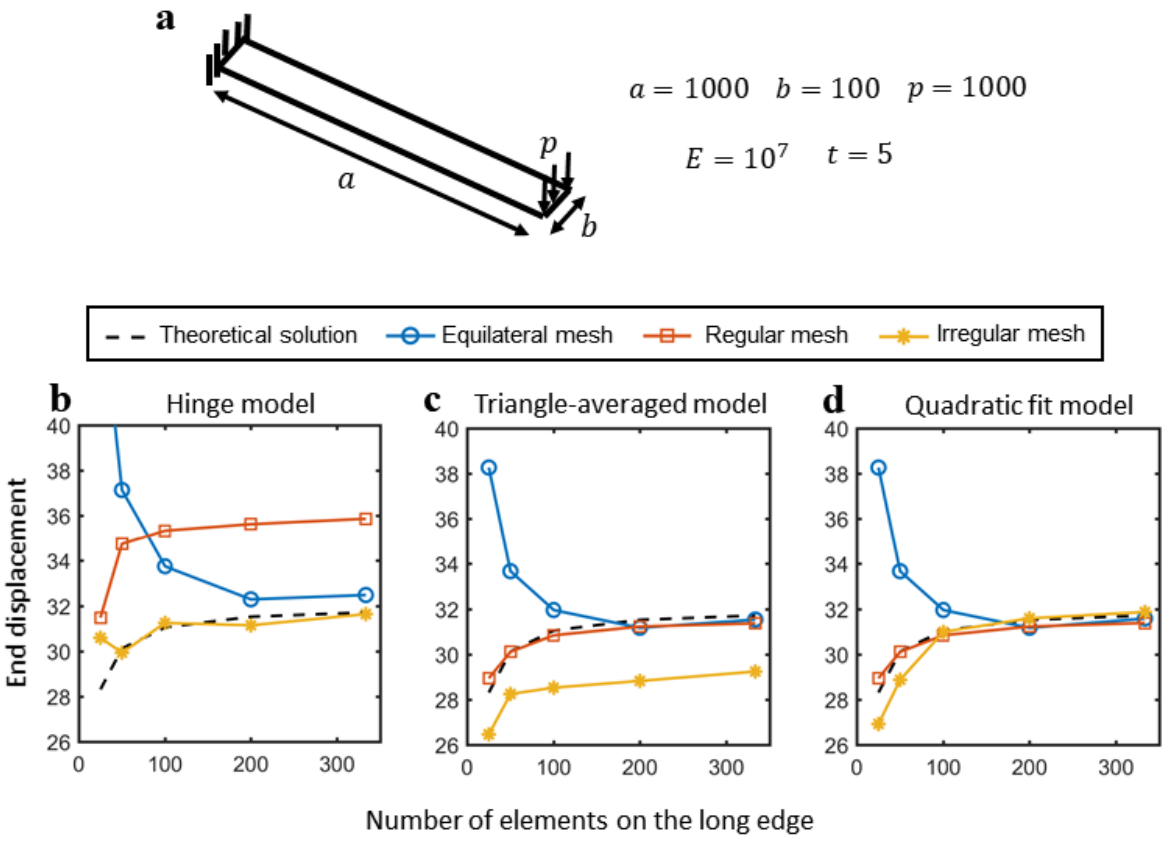

Figure 2.8 (a) A rectangular piece of thin plate fixed at one end is subjected to a distributed line load at the other end. (b-d) Convergence behaviors of end displacement on a sequence of increasingly fine meshes compared to the theoretical solution for different discrete shell models and mesh types.

Figures 2.8b-d plot the convergence behaviors of end displacement on a sequence of increasingly fine meshes compared to the theoretical solution for cantilever beam bending. We observe that the quadratic fit model is the only model that converges to the theoretical solution on all mesh types. The hinge and triangle averaged models are only convergent on regular and irregular meshes. Note that the clamped boundary conditions in these discrete shell models need to constrain two layers of nodes, which effectively leads to a mesh dependent total length of the thin plate. This is the reason why the analytical solution of the plate deflection varies with the element number.

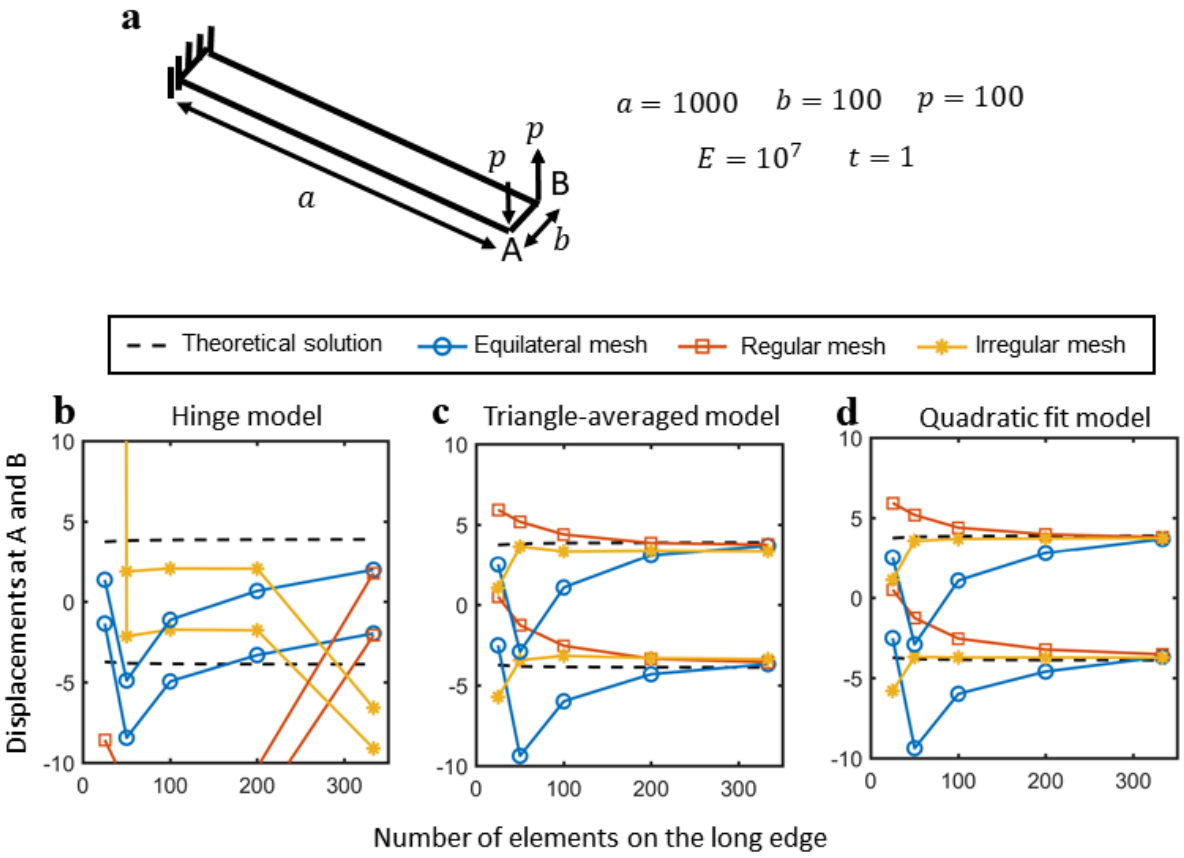

Figure 2.9 (a) A rectangular piece of thin plate fixed at one end is subjected to a twisting couple at the other end. (b-d) Convergence behaviors of displacements at A and B on a sequence of increasingly fine meshes compared to the theoretical solution for different discrete shell models and mesh types.

Figures 2.9b-d plot the convergence behaviors for cantilever beam twisting. We observe that the quadratic fit model is the only model that converges to the theoretical solution on all mesh types. The triangle-averaged and quadratic fit models converge to the continuous energy on all mesh types, while the hinge model fails to converge on all mesh types.

Numerically simulating deformations in thin elastic sheets is a challenging problem in computational mechanics due to destabilizing compressive stresses that result in wrinkling [56]. Determining the structure of wrinkle patterns in these problems is an area of increasing interest in the fields of physics and engineering [70]. Here we consider the classical Lamé problem [68]: an annular sheet of thickness t and radii $r_i < r_o$ is subjected to radial tensile loads γ_i and γ_o at its inner and outer boundaries (Figure 2.10a). Intuitively, if γ_i is sufficiently larger than γ_o, a region near the inner boundary is pulled inward, such that the sheet is subjected there to hoop compression, which is relieved through a wrinkle pattern.

Similar to the cantilever beam tests, we implement the three models as user-defined potentials in LAMMPS and add a fictitious damping force to each node. The radial tensile loads are added through user-defined potentials rather than forces applied on boundary nodes since the direction of forces depends on the position of the boundary node. After applying random perturbations to all atoms at the beginning of simulations through Langevin thermostat to make sure the system is not trapped in the unwrinkled equilibrium state, the discrete system is dynamically relaxed until the wrinkle pattern reaches stabilization.

Figure 2.10b compares stabilized wrinkle patterns for the parameters listed in Figure 2.10a, obtained using the three discrete shell models on equilateral and irregular meshes. Several mesh sizes have been tested such that refinement of the current mesh size ($a = 1$) will not change the number of wrinkles. We observe that all models yield mesh-dependent wrinkle patterns: (1) The

wrinkle extension length tends to be more uniformly distributed in all directions on equilateral mesh than on irregular mesh (2) The numbers of wrinkles are different on two mesh types for the triangle-averaged and quadratic fit models. We also notice that all the models predict similar wrinkle numbers compared to the theoretical model and the numerical simulations based on the classic shell models [56]. This indicates that the discrete shell models are applicable to the Lamé problem if the statistical characterization of the wrinkling patterns (e.g., the radial distribution of wrinkle numbers) is of the main interest.

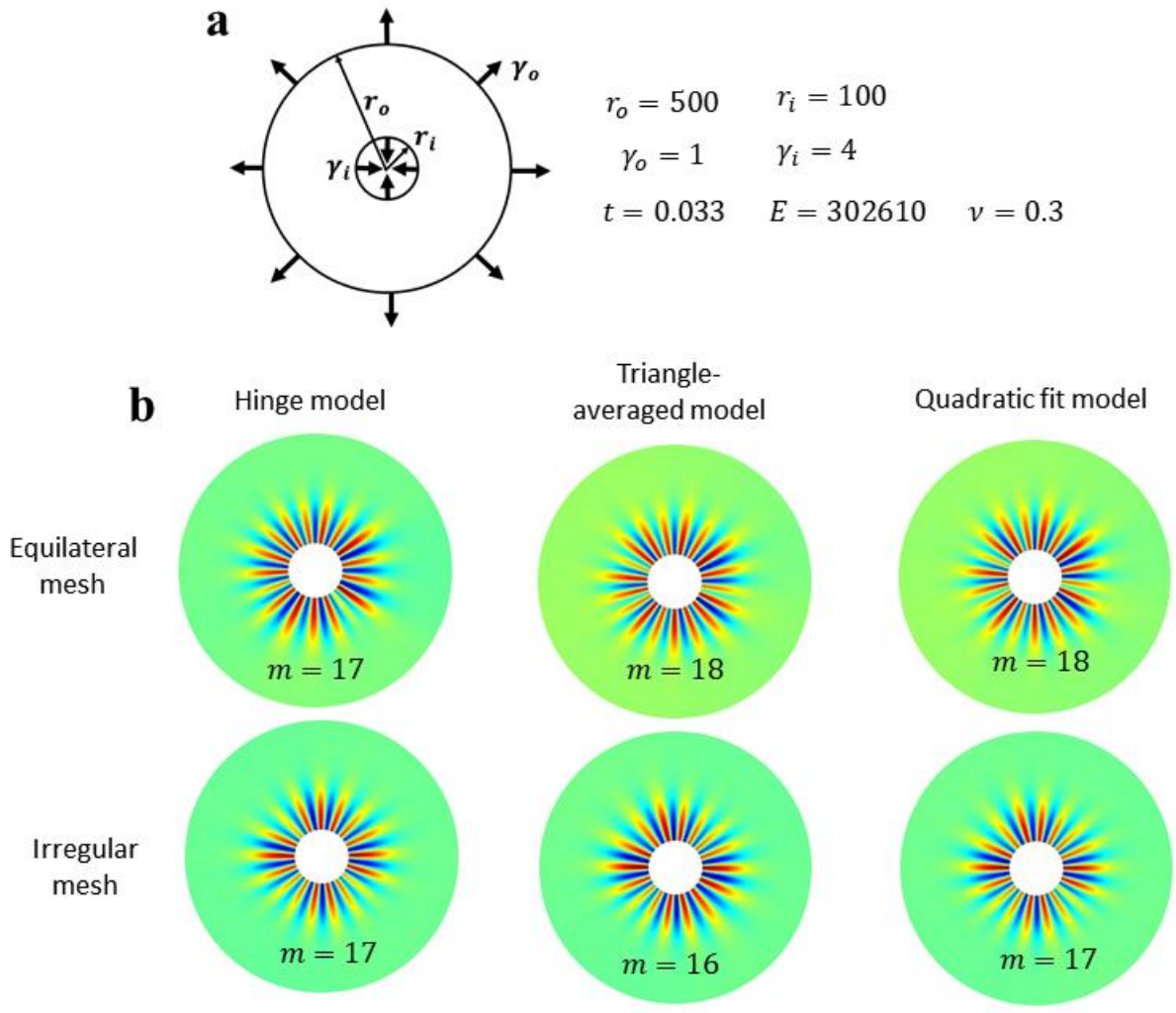

Figure 2.10 (a) Classical Lamé problem: an annular sheet of thickness t and radii $r_i < r_o$ is subjected to radial tensile loads γ_i and γ_o at its inner and outer boundaries. (b) Wrinkle patterns (marked with the number of wrinkles m) of the Lamé problem for different discrete shell models on equilateral and irregular meshes.

2.5.2 Comparison with finite element method

Here we test two shell buckling problems and compare the results of the discrete shell model with hinge bending energy and finite element simulations performed in ABAQUS. The first problem is poking an axially compressed cylindrical (radius R_0 = 28.6 mm, height L_0 = 107 mm, thickness t = 0.104 mm, Young's Modulus E = 71000 MPa and Poisson's ratio ν = 0.3) with a spherical indenter (radius $r = 2.35$ mm), as illustrated in Figure 2.11A. The cylinder is initially compressed to a preset axial strain $\epsilon_{\mathrm{A}} = \epsilon_{\mathrm{A}}^0$. When the preset load is reached, the nodes at the top and bottom ends of the cylinder are fixed, while the horizontal indenter is advanced towards the cylinder at a constant speed, and the indenter force F_{p} is simultaneously recorded. Shell stability is investigated by poking individual cylinders from the side with ϵ_{A}^0 ranging from 5×10^{-4} to 10×10^{-4}. Depending on ϵ_{A}^0, simulation reveals a plethora of stereotypical responses, with three qualitatively different regimes. For small values of ϵ_{A}^0, F_{p} monotonically increases, as shown by the $\epsilon_{\mathrm{A}}^0 = 5 \times 10^{-4}$ curve in Figure 2.11B. In this regime, the cylinders are stable and do not buckle. A second regime emerges at an intermediate range of ϵ_{A}^0, the shells still do not buckle but the F_{p} curves are more detailed and nonmonotonic, exhibiting a maximum force $F_{\mathrm{p}}^{\max}$ and then a local minimum force $F_{\mathrm{p}}^{\min}$, as shown by the $\epsilon_{\mathrm{A}}^0 = 8 \times 10^{-4}$ and $\epsilon_{\mathrm{A}}^0 = 7 \times 10^{-4}$ curves in Figure 2.11B. For larger values of ϵ_{A}^0, poking eventually leads to buckling. The F_{p} curve shows a maximum. However, it will no longer show a minimum; instead, at a critical distance F_{p} vanishes, and

at this point the shells become unstable and buckles, as shown by the $\epsilon_{\mathrm{A}}^{0} = 9 \times 10^{-4}$ and $\epsilon_{\mathrm{A}}^{0} = 10 \times 10^{-4}$ curves in Figure 2.11B. The F_{p} curves obtained by the ABAQUS simulations using 4-node shell finite elements are also plotted in Figure 2.11B, and they are in great agreement with those obtained by the MD simulations. The instabilities during poking captured by our simulations have also been reported in experiments [55].

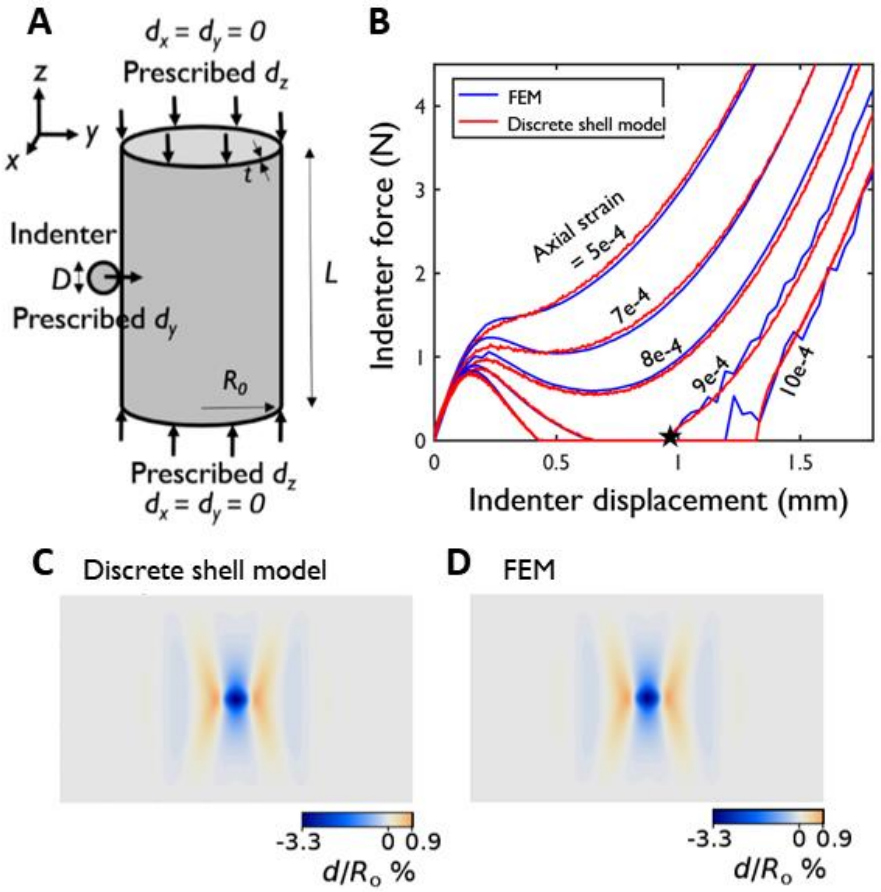

Figure 2.11 Simulations of poking a cylindrical shell under axial compression. The cylinder has a radius R_0 = 28.6 mm, L_0 = 107 mm, t = 0.104 mm, Young's Modulus E = 71000 MPa and Poisson's ratio ν = 0.3. The spherical indenter has a radius $r = 2.35$ mm. (A) Loading and boundary conditions. (B) Poking force vs. displacement curves obtained from FEM and discrete

shell model simulations at different axial strains. (C-D) Contour plots of the radial displacement fields at the local energy minima of the axial strain = 9×10^{-4} curves (black star in panel B).

The second problem is the bending of a slender cylindrical shell under an axial compressive strain slightly above Euler's buckling load of a beam with the same boundary conditions as the first problem. The comparison between our model and the shell finite element method in ABAQUS is presented in Figure 2.12. The lateral deflection fields of both models are in good agreement, with a difference of less than 1% in maximum values.

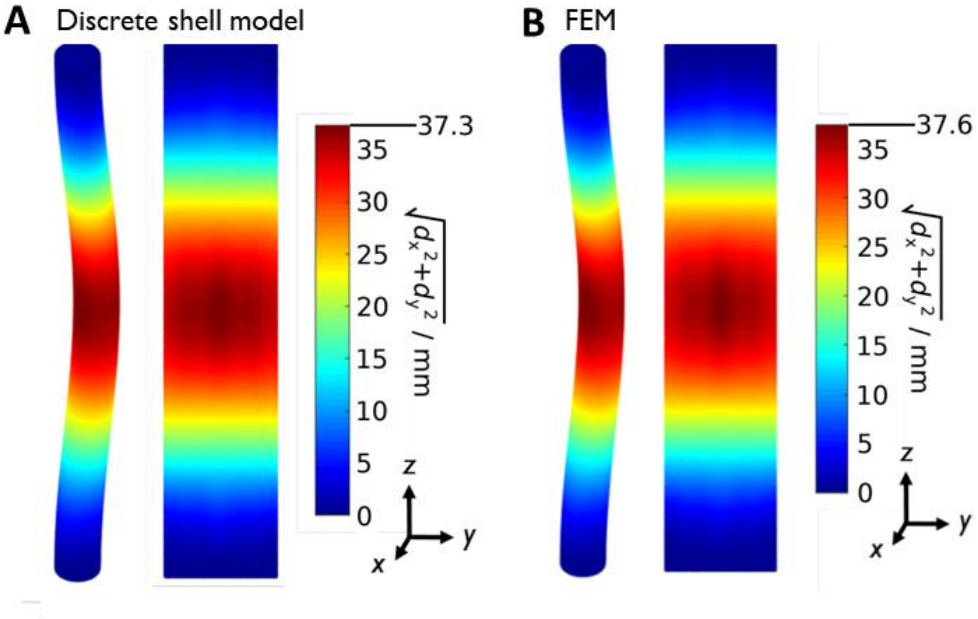

Figure 2.12 Beam-bending simulations for a long cylindrical shell under compression. The cylinder has a radius R_0 = 28.6 mm, length L_0 = 858 mm, thickness t = 3.575 mm, Young's Modulus E = 71000 MPa and Poisson's ratio ν = 0.3. (A-B) Contour plots of lateral deflection fields obtained from FEM and discrete shell model simulations under an axial strain of 0.024.

2.6 Summary

We implemented the three discrete thin shell models in molecular dynamics code LAMMPS as user-defined potentials and tested their mesh dependency behaviors and accuracy on several benchmark problems. We show that among the three models, only the quadratic fit model is convergent to the theoretical solution in all tests regardless of mesh types. It is also worth noting that all three models are convergent on equilateral mesh in all tests. Our results suggest that for thin shell problems in which an equilateral mesh is possible, the hinge model is a preferable choice since it is not only convergent but also the easiest to implement and the most computationally efficient. Otherwise, the quadratic fit model is the only choice to ensure convergence on general triangular meshes. Our test results of the Lamé problem show that the wrinkle patterns are mesh-dependent for all models. This is possibly due to the existence of multiple local energy minima (metastable states) in the Lamé problem. In this case, the fully relaxed wrinkle pattern will be highly sensitive to different meshes and initial perturbations. Our cylinder poking and beam buckling results show that the accuracy of the discrete shell model with hinge bending energy is comparable with the shell finite element method.

Chapter 3: Energy Landscapes of Shell Buckling

3.1 Introduction

Natural and engineered structures ranging from egg shells to spacecraft are built from thin shells that offer exceptional rigidity at minimal weight. Accurately predicting and designing the buckling loads of those shells is thus an important yet not fully resolved problem of structural engineering.

The main focus of shell stability analysis in the literature has been attempting to explain the tremendous discrepancy between theoretically predicted and experimentally measured buckling loads for imperfection-sensitive thin shell structures, two prototypical examples of which are cylindrical shells under axial compression [72] and spherical shells under external pressure [73]. As shown in Figure 3.1, which plots the experimental buckling data collected in the 1960s for axially compressed cylindrical shells, all tested cylinders buckled at loads significantly lower than those predicted by theory, and in some cases, buckling occurred at less than 20% of the theoretical values.

Early works [72,73] contributing to the understanding of this discrepancy generally focused on analyzing the buckling of thin shells with geometric imperfections in the shape of classical buckling modes that extend over the entire shell, i.e. sinusoidal axisymmetric imperfections for cylindrical and spherical shells. These works revealed that small geometric imperfections in thin shell structures can dramatically reduce their buckling loads. With the progress of numerical methods and understanding of nonlinear phenomena, the importance of localized dimple imperfections has been demonstrated in later works [74,80], as they represent more realistic and unfavorable geometric imperfections. Subsequent theoretical [81-83] and experimental [84] results

revealed the extreme imperfection sensitivity of externally pressurized spherical shells: the buckling pressure of imperfect shell plateaus to roughly 20% of that of a perfect shell when the imperfection amplitude exceeds about one shell thickness.

One recent development in shell stability analysis is to quantify the robustness of a loaded shell against buckling in the presence of disturbing forces or unexpected loads with the energy barrier between its unbuckled and post-buckling states, i.e. the minimum energy required for a loaded shell to buckle. A ground-breaking analysis was carried by Horak et al. [75], who numerically computed the buckling energy barrier for axially compressed cylindrical shells, and used a novel mathematical technique to prove that single-dimple buckling is the most energetically favorable (having the lowest energy barrier). Influenced by this work, Hutchinson and Thompson [82] performed a highly accurate post-buckling analysis of spherical shells under external pressure and determined their buckling energy barriers. Their results showed that the buckling mode localizes into a dimple immediately after the onset of buckling. It has also been shown that these theoretical energy barriers can be measured experimentally by probing a loaded shell [83,85-87].

For more realistic engineering shell structures, a general computational framework is needed to characterize their imperfection sensitivity and robustness against buckling. Here, we demonstrate how this can be done by comprehensively surveying the energy landscapes for shell buckling. In section 3.2, we briefly describe our numerical methods: a simple discrete shell model combined with efficient energy minimization and pathfinding algorithms, as well as their LAMMPS and Fortran implementations. In sections 3.3 and 3.4, we apply our methods to two prototypical examples: spherical cap and cylindrical cap buckling. Section 3.5 is a summary of this chapter.

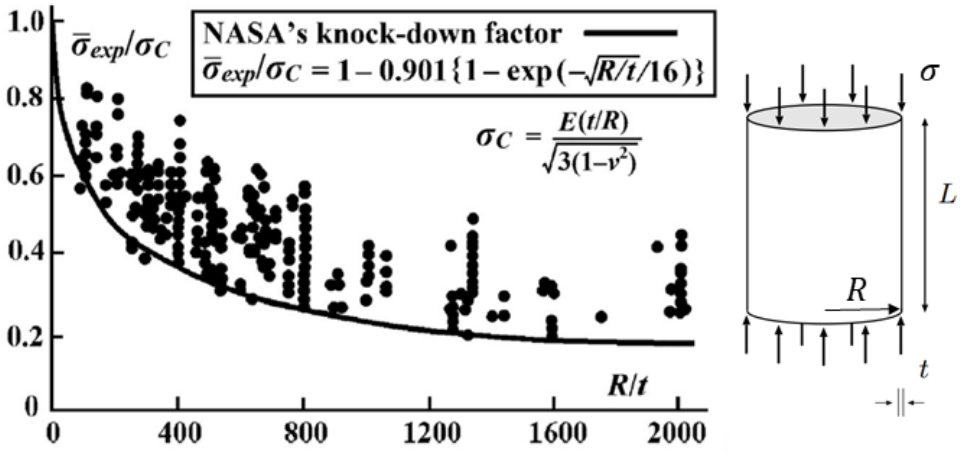

Figure 3.1 Buckling of cylindrical shells under axial compression. Experimental buckling data for thin cylindrical shells under axial compression collected in the 1960s and plotted as the average compressive stress at buckling $\bar{\sigma}_{\text{exp}}$ divided by the classical buckling stress σ_{c} for the perfect shell versus the radius to thickness ratio. The NASA knockdown factor used in design codes for assigning the buckling load assuming 'worse case' imperfections is shown. This figure is from Reference [88].

3.2 Numerical methods

3.2.1 Energy discretization

Here, the discrete shell model with hinge bending energy discussed in Chapter 2 is used to discretize the elastic energy of thin shells. As shown in Figure 2.6, this model is not only the most computationally efficient but also convergent (in terms of energy) on equilateral triangular mesh with which we discretize the cylindrical shells here. Here we briefly summarize the discrete energy formulation on a triangular mesh.

The discrete membrane energy on the triangle shown in Figure 3.1 (left) is

$$E_m = \frac{A}{2} a_{ip} s_i s_p \tag{3.1}$$

where $s_i = l_i^2 - L_i^2$ are the change in square length of edge i, a_{ip} are coefficients that depend o nly on the undeformed mesh and their values are given in Equations (2.30) – (2.36), and A is the undeformed triangular area.

The discrete bending energy of on each hinge shown in Figure 3.1 (right) is

$$E_b = k[1 - \cos(\theta - \bar{\theta})] \tag{3.2}$$

where θ and $\bar{\theta}$ are deformed and undeformed hinge angles and k is a coefficient that depends only on the undeformed mesh and its value is given in Equation (2.44).

The discrete elastic energy of the entire shell is then computed by summing up the discrete membrane energy (3.1) on all triangles and the discrete bending energy (3.2) on all hinges.

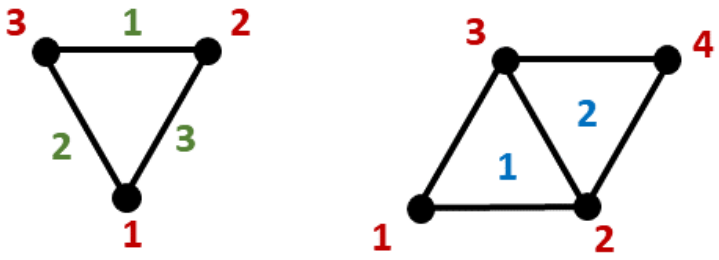

Figure 3.2 Numbering of vertices, edges, and triangles in the computation of discrete membrane (left) and bending (right) energy

3.2.2 Energy minimization algorithms

Finding mechanically stable equilibrium configurations of discrete systems is one of the most common tasks in not only solid mechanics, but also materials science, solid-state physics, chemistry, and biology. For a discrete system consisting of N vertices and its configuration rep-

resented by a $3N$-dimensional position vector $\mathbf{x} \in \mathbb{R}^{3N}$, this corresponds to finding the local minima of the potential energy function $E(\mathbf{x})$. To solve this task a variety of well-established minimization methods, like conjugate gradient (CG), Newton Raphson, quasi-Newton, and dynamic relaxation (DR) methods are available [91-95]. This section briefly describes two widely used variants of the conjugate gradient and quasi-Newton methods, both of which will be used in our computational framework.

3.2.2.1 Polak-Ribière conjugate gradient algorithm

The conjugate gradient (CG) method was introduced by Fletcher and Reeves in the 1960s [99]. It is one of the earliest known techniques for solving large-scale nonlinear optimization problems. Over the years, many variants of this original scheme have been proposed. The variant considered here is the Polak-Ribière version proposed by Polak [100].

The CG algorithm is an iterative method and iteration numbers are shown as subscripts. For example, the sequence of points $\mathbf{x}_1, \mathbf{x}_2, \mathbf{x}_3$, ... is calculated by the successive iterations and it should converge to the point in the space of the variables at which $E(\mathbf{x})$ is least. Let k denote the number of the current iteration starting with $k = 0$ and $\mathbf{g}_k = \boldsymbol{\nabla} E(\mathbf{x}_k)$ be the energy gradient in the nth iteration. If $k = 0$, let $\mathbf{d}_k$ be the steepest descent direction

$$\mathbf{d}_k = -\mathbf{g}_k \tag{3.3}$$

Otherwise, for $k \geq 1$, we apply the formula

$$\mathbf{d}_k = -\mathbf{g}_k + \beta_k \mathbf{d}_{k-1} \tag{3.4}$$

where β_k has the value

$$\beta_k = \langle \mathbf{g}_k, \mathbf{g}_k - \mathbf{g}_{k-1} \rangle / \langle \mathbf{g}_{k-1}, \mathbf{g}_{k-1} \rangle \tag{3.5}$$

with $\langle \quad \rangle$ being the inner product of two vectors. We obtain $\mathbf{x}_{k+1}$ by searching for the minimum value of $E(\mathbf{x})$ from $\mathbf{x}_k$ along the direction $\mathbf{d}_k$. Thus $\mathbf{x}_{k+1}$ is the vector

$$\mathbf{x}_{k+1} = \mathbf{x}_k + \lambda_k \boldsymbol{d}_k \tag{3.6}$$

where λ_k is the value of λ that satisfies the Wolfe conditions:

$$E(\mathbf{x}_k + \alpha_k \mathbf{p}_k) \leq E(\mathbf{x}_k) + c_1 \alpha_k \boldsymbol{\nabla} E_k^T \mathbf{p}_k \tag{3.7}$$

$$\boldsymbol{\nabla} E(\mathbf{x}_k + \alpha_k \mathbf{p}_k)^T \mathbf{p}_k \geq c_2 \boldsymbol{\nabla} E_k^T \mathbf{p}_k \tag{3.8}$$

This completes the iteration, and another one is begun unless the energy gradient is sufficiently small:

$$\|\boldsymbol{\nabla} E(\mathbf{x}_k)\| \leq \epsilon \tag{3.9}$$

where ϵ is a small positive number.

The complete algorithm is summarized as follows:

Box 3.1 Polak-Ribière conjugate gradient algorithm

Input:

Potential energy function $E(\mathbf{x})$

Initial configuration $\mathbf{x_0} \in \mathbb{R}^{3N}$

Wolfe conditions parameters $0 < c_1 < c_2 \ll 1$

Convergence tolerance $0 < \epsilon \ll 1$

Output:

Converged configuration $\mathbf{x}_{\min}$

Steps:

1. Set $k = 0$ and $-\mathbf{d}_0 = \mathbf{g}_0 = \boldsymbol{\nabla} E(\mathbf{x}_0)$.
2. Compute $\lambda_k \geq 0$ that satisfies the Wolfe conditions:

$$E(\mathbf{x}_k + \alpha_k \mathbf{p}_k) \leq E(\mathbf{x}_k) + c_1 \alpha_k \boldsymbol{\nabla} E_k^T \mathbf{p}_k$$

$$\boldsymbol{\nabla} E(\mathbf{x}_k + \alpha_k \mathbf{p}_k)^T \mathbf{p}_k \geq c_2 \boldsymbol{\nabla} E_k^T \mathbf{p}_k$$

3. Update $\mathbf{x}_k$

$$\mathbf{x}_{k+1} = \mathbf{x}_k + \lambda_k \boldsymbol{d}_k$$

4. If $\|\boldsymbol{\nabla} E(\mathbf{x}_k)\| \leq \epsilon$, stop. Else, set

$$\mathbf{g}_{k+1} = \boldsymbol{\nabla} E(\mathbf{x}_{k+1})$$

$$\beta_k = \langle \mathbf{g}_k, \mathbf{g}_k - \mathbf{g}_{k-1} \rangle / \langle \mathbf{g}_{k-1}, \mathbf{g}_{k-1} \rangle$$

$$\mathbf{d}_{k+1} = -\mathbf{g}_{k+1} + \beta_k \mathbf{d}_k$$

$$k = k + 1$$

and go to Step 3.

3.2.2.2 L-BFGS algorithm

In Quasi-Newton methods, a model of the potential energy function that is good enough to produce superlinear convergence is constructed using the Hessian matrix approximated by measuring the changes in gradients. There exist a variety of quasi-Newton algorithms for solving optimization problems. The most popular one is the BFGS algorithm, named for its discoverers Broyden [101], Fletcher [102], Goldfarb [103], and Shanno [104]. Also in common use is the L-BFGS algorithm [105], which is a limited-memory version of BFGS that is particularly suited to problems with very large numbers of variables. Before describing the L-BFGS algorithm, I will first introduce its parent, the BFGS algorithm.

The algorithm forms the following quadratic model of the energy function at the current iterate $\mathbf{x}_k$:

$$m_k(\mathbf{p}) = E_k + \boldsymbol{\nabla} E_k^T \mathbf{p} + \frac{1}{2} \mathbf{p}^T \mathbf{B}_k \mathbf{p} \tag{3.10}$$

Here $\mathbf{B}_k$ is the $3N \times 3N$ symmetric positive definite matrix that will be revised or updated at every iteration. The minimizer $\mathbf{p}_k$ of this convex quadratic model can be written explicitly as

$$\mathbf{p}_k = -\mathbf{H}_k \nabla E_k \tag{3.11}$$

where $\mathbf{H}_k = \mathbf{B}_k^{-1}$. Using $\mathbf{p}_k$ as the search direction, and the new iterate is

$$\mathbf{x}_{k+1} = \mathbf{x}_k + \alpha_k \mathbf{p}_k \tag{3.12}$$

where the step length α_k is chosen to satisfy the sufficient decrease and curvature conditions (Wolfe conditions):

$$E(\mathbf{x}_k + \alpha_k \mathbf{p}_k) \leq E(\mathbf{x}_k) + c_1 \alpha_k \nabla E_k^T \mathbf{p}_k \tag{3.13}$$

$$\nabla E(\mathbf{x}_k + \alpha_k \mathbf{p}_k)^T \mathbf{p}_k \geq c_2 \nabla E_k^T \mathbf{p}_k \tag{3.14}$$

with $0 < c_1 < c_2 < 1$.

Suppose that we have generated a new iterate $\mathbf{x}_{k+1}$, the new quadratic model has the form

$$m_{k+1}(\mathbf{p}) = E_{k+1} + \nabla E_{k+1}^T \mathbf{p} + \frac{1}{2} \mathbf{p}^T \mathbf{B}_{k+1} \mathbf{p} \tag{3.15}$$

Instead of computing $\mathbf{B}_{k+1}$ afresh at every iteration, we wish to update it to account for the curvature measured during the most recent step. Therefore, we require that the gradient of m_{k+1} match the gradient of the energy function E at the iterate $\mathbf{x}_k$:

$$\nabla m_{k+1}(-\alpha_k \mathbf{p}_k) = \nabla E_{k+1} - \alpha_k \mathbf{B}_{k+1} \mathbf{p}_k = \nabla E_k \tag{3.16}$$

Rearranging (3.16) and using $\mathbf{H}_{k+1} = \mathbf{B}_{k+1}^{-1}$ yields

$$\alpha_k \mathbf{p}_k = \mathbf{H}_{k+1}(\nabla E_{k+1} - \nabla E_k) \tag{3.17}$$

To simplify the notation it is useful to define the vectors

$$\mathbf{s}_k = \mathbf{x}_{k+1} - \mathbf{x}_k = \alpha_k \mathbf{p}_k \tag{3.18}$$

$$\mathbf{y}_k = \nabla E_{k+1} - \nabla E_k \tag{3.19}$$

So that (3.17) becomes

$$\mathbf{s}_k = \mathbf{H}_{k+1} \mathbf{y}_k \tag{3.20}$$

Equation (3.21) admits an infinite number of solutions of $\mathbf{H}_{k+1}$, since the degrees of freedom in a symmetric positive definite matrix exceed the n conditions imposed by Equation (3.21).

To determine $\mathbf{H}_{k+1}$ uniquely, we impose the additional condition that among all symmetric matrices satisfying Equation (3.21), $\mathbf{H}_{k+1}$ is closest to the current matrix $\mathbf{H}_k$. In other words, we solve the problem

$$\min_{\mathbf{H}} \|\mathbf{H} - \mathbf{H}_k\| \tag{3.21}$$

subject to

$$\mathbf{H} = \mathbf{H}^{\mathrm{T}} \tag{3.22}$$

$$\mathbf{H}\mathbf{y}_k = \mathbf{s}_k \tag{3.23}$$

The unique solution $\mathbf{H}_{k+1}$ to (3.24) is given by

$$\mathbf{H}_{k+1} = \mathbf{V}_k^T \mathbf{H}_k \mathbf{V}_k + \rho_k \mathbf{s}_k \mathbf{s}_k^T \tag{3.24}$$

where

$$\rho_k = \frac{1}{\mathbf{y}_k^T \mathbf{s}_k} \tag{3.25}$$

$$\mathbf{V}_k = \mathbf{I} - \rho_k \mathbf{y}_k \mathbf{s}_k^T \tag{3.26}$$

Equations (3.11) – (3.12) and (3.24) – (3.26) comprise the BFGS algorithm.

Since the inverse Hessian approximation $\mathbf{H}_k$ will generally be dense, the cost of storing and manipulating it is prohibitive when the number of variables is large. To circumvent this problem, the following recursive formula is used to compute $\mathbf{H}_k$ in the L-BFGS algorithm:

$$\begin{aligned}
\mathbf{H}_k = {} & (\mathbf{V}_{k-1}^T \cdots \mathbf{V}_{k-m}^T)\mathbf{H}_k^0(\mathbf{V}_{k-m} \cdots \mathbf{V}_{k-1}) \\
& + \rho_{k-m}(\mathbf{V}_{k-1}^T \cdots \mathbf{V}_{k-m+1}^T)\mathbf{s}_{k-m}\mathbf{s}_{k-m}^T(\mathbf{V}_{k-m+1} \cdots \mathbf{V}_{k-1}) \\
& + \rho_{k-m+1}(\mathbf{V}_{k-1}^T \cdots \mathbf{V}_{k-m+2}^T)\mathbf{s}_{k-m+1}\mathbf{s}_{k-m+1}^T(\mathbf{V}_{k-m+2} \cdots \mathbf{V}_{k-1}) \\
& + \cdots \\
& + \rho_{k-1}\mathbf{s}_{k-1}\mathbf{s}_{k-1}^T
\end{aligned} \tag{3.27}$$

which is obtained by repeated application of the formula (3.24). From this expression, we can derive a recursive procedure to compute the product $\mathbf{H}_k \boldsymbol{\nabla} E_k$ efficiently.

The L-BFGS algorithm can be stated formally as follows.

Box 3.2 L-BFGS algorithm

Input:

Potential energy function $E(\mathbf{x})$

Initial configuration $\mathbf{x_0} \in \mathbb{R}^{3N}$

Initial Hessian matrix $\mathbf{H}_0$

Wolfe conditions parameters $0 < c_1 < c_2 \ll 1$

Convergence tolerance $0 < \epsilon \ll 1$

Output:

Converged configuration $\mathbf{x}_{\min}$

Steps:

1. Set $k = 0$.
2. Compute $\mathbf{p}_k$

$$\mathbf{p}_k = -\mathbf{H}_k \boldsymbol{\nabla} E_k$$

3. Update $\mathbf{x}_k$

$$\mathbf{x}_{k+1} = \mathbf{x}_k + \alpha_k \mathbf{p}_k$$

where α_k satisfies the Wolfe conditions:

$$E(\mathbf{x}_k + \alpha_k \mathbf{p}_k) \leq E(\mathbf{x}_k) + c_1 \alpha_k \boldsymbol{\nabla} E_k^T \mathbf{p}_k$$

$$\boldsymbol{\nabla} E(\mathbf{x}_k + \alpha_k \mathbf{p}_k)^T \mathbf{p}_k \geq c_2 \boldsymbol{\nabla} E_k^T \mathbf{p}_k$$

4. If $\|\boldsymbol{\nabla} E(\mathbf{x}_k)\| \leq \epsilon$, stop. Else, go to Step 5.

5. Let $\hat{m} = \min\{k, m-1\}$. Update $\mathbf{H}_k$ $\hat{m}+1$ times using the pairs $\{\mathbf{y}_j, \mathbf{s}_j\}_{j=k-\hat{m}}^{k}$:

$$\mathbf{H}_k = (\mathbf{V}_{k-1}^T \cdots \mathbf{V}_{k-m}^T)\mathbf{H}_k^0(\mathbf{V}_{k-m} \cdots \mathbf{V}_{k-1})$$

$$+\rho_{k-m}(\mathbf{V}_{k-1}^T \cdots \mathbf{V}_{k-m+1}^T)\mathbf{s}_{k-m}\mathbf{s}_{k-m}^T(\mathbf{V}_{k-m+1} \cdots \mathbf{V}_{k-1})$$

$$+\rho_{k-m+1}(\mathbf{V}_{k-1}^T \cdots \mathbf{V}_{k-m+2}^T)\mathbf{s}_{k-m+1}\mathbf{s}_{k-m+1}^T(\mathbf{V}_{k-m+2} \cdots \mathbf{V}_{k-1})$$

$$+\cdots$$

$$+\rho_{k-1}\mathbf{s}_{k-1}\mathbf{s}_{k-1}^T$$

where

$$\mathbf{s}_k = \alpha_k \mathbf{p}_k$$

$$\mathbf{y}_k = \nabla E_{k+1} - \nabla E_k$$

$$\rho_k = \frac{1}{\mathbf{y}_k^T \mathbf{s}_k}$$

$$\mathbf{V}_k = \mathbf{I} - \rho_k \mathbf{y}_k \mathbf{s}_k^T$$

6. Set $k = k+1$ and go to Step 2.

3.2.3 Pathfinding algorithms

Another important problem in characterizing complex systems is to find the transition path between any two stable states. Such path is known as the minimum energy path (MEP), which is defined as the path in configuration space along which energy gradient is everywhere parallel to the path tangent vector. The MEP allows us to identify the transition state (the energy maxima on the MEP) and the energy barrier required to overcome (the energy difference between the transition state and the stable state) in a transition. An illustrative example of the MEP, stable state, and transition state in the energy landscape of a simple system with two degrees of freedom is

shown in Figure 3.5D. This section describes two widely used computational methods for finding MEPs, the nudged elastic band (NEB) method [106-108] and the string method [109-111].

3.2.3.1 Nudged elastic band method

Consider again a discrete system consisting of N vertices and its state represented by a $3N$-dimensional position vector $\mathbf{x} \in \mathbb{R}^{3N}$. The minimum energy path (MEP) $\mathbf{x}(\lambda)$ ($\lambda_{\text{init}} \leq \lambda \leq \lambda_{\text{fin}}$) connects the two energy minima (stable states) $\mathbf{x}_{\text{init}} = \mathbf{x}(\lambda_{\text{init}})$ and $\mathbf{x}_{\text{fin}} = \mathbf{x}(\lambda_{\text{fin}})$, and passes through at least one transition state $\mathbf{x}_{\text{trans}} = \mathbf{x}(\lambda_{\text{trans}})$ ($\lambda_{\text{initial}} \leq \lambda_{\text{trans}} \leq \lambda_{\text{final}}$). Let an elastic band be a sequence of $m+1$ images, $\{\mathbf{x}^0, \mathbf{x}^1, \ldots, \mathbf{x}^m\}$, where the two ends of the band corresponding to the initial ($\mathbf{x}^0 = \mathbf{x}_{\text{init}}$) and final ($\mathbf{x}^m = \mathbf{x}_{\text{fin}}$) states are fixed and the $m-1$ intermediate images are adjusted by the NEB algorithm. The band is a discrete approximation to the MEP $\mathbf{x}(\lambda)$.

The NEB method [106-108] starts with an initial band connecting the initial and final states. Typically, a linear initial path is enough. The states along the band are then relaxed to the MEP through a force projection scheme in which the total force on image $\mathbf{x}^i$ contains two independent components,

$$\mathbf{F}^i = \mathbf{F}_{\perp}^i + \mathbf{F}_{\parallel}^i \tag{3.28}$$

where $\mathbf{F}_{\perp}^i$ is the component of the force due to the potential perpendicular to the band,

$$\mathbf{F}_{\perp}^i = -\boldsymbol{\nabla} E(\mathbf{x}^i) + [\boldsymbol{\nabla} E(\mathbf{x}^i) \cdot \hat{\boldsymbol{\tau}}^i]\hat{\boldsymbol{\tau}}^i \tag{3.29}$$

and $\mathbf{F}_{\parallel}^i$ is the spring force parallel to the band,

$$\mathbf{F}_{\parallel}^i = k(|\mathbf{x}^{i+1} - \mathbf{x}^i| - |\mathbf{x}^i - \mathbf{x}^{i-1}|)\hat{\boldsymbol{\tau}}^i \tag{3.30}$$

In the above two equations, k is the spring constant, and $\hat{\boldsymbol{\tau}}^i$ is the unit tangent vector estimated by averaging the adjacent line segments on the band:

$$\boldsymbol{\tau}^i = \frac{\mathbf{x}^{i+1} - \mathbf{x}^i}{|\mathbf{x}^{i+1} - \mathbf{x}^i|} + \frac{\mathbf{x}^i - \mathbf{x}^{i-1}}{|\mathbf{x}^i - \mathbf{x}^{i-1}|} \tag{3.31}$$

$$\hat{\boldsymbol{\tau}}^i = \frac{\boldsymbol{\tau}^i}{|\boldsymbol{\tau}^i|} \tag{3.32}$$

The spring force $\mathbf{F}_{\parallel}^i$ thus drives the images equidistant from each other along the path, whereas the perpendicular potential force $\mathbf{F}_{\perp}^i$ drives each image toward an energy minimum in the direction perpendicular to the path. Minimization algorithms, such as those described in the previous section, are then used to move the band toward the MEP according to these forces, as it has been shown that a band with zero forces is a discretized approximation to a MEP [106,108].

While the above force projection scheme gives a discrete representation of the MEP, the energy of the transition state needs to be obtained by interpolation and the interpolation can be inaccurate. To overcome this problem, the force on the image $\mathbf{x}^{i\max}$ with the highest energy is replaced by

$$\mathbf{F}^{i\max} = -\boldsymbol{\nabla} E\left(\mathbf{x}^{i\max}\right) + 2\left[\boldsymbol{\nabla} E\left(\mathbf{x}^{i\max}\right) \cdot \hat{\boldsymbol{\tau}}^{i\max}\right]\hat{\boldsymbol{\tau}}^{i\max} \tag{3.33}$$

This is the full force due to the potential with the component along the elastic band inverted. This force moves image $\mathbf{x}^{i\max}$ up the potential energy surface along the elastic band and down the potential surface perpendicular to the band. As a result, image $\mathbf{x}^{i\max}$ eventually converges to the transition state.

The NEB method is summarized in box 3.3.

Box 3.3 Nudged elastic band method

Input:

Potential energy function $E(\mathbf{x})$

Initial and final stable states $\mathbf{x}_{\text{init}}, \mathbf{x}_{\text{fin}}$

Spring constant k

Convergence tolerance ϵ

Output:

Fully relaxed elastic band $\{\mathbf{x}^0, \mathbf{x}^1, \dots, \mathbf{x}^m\}$

Steps:

1. Set $k = 0$. Initialize the elastic band $\{\mathbf{x}_0^0, \mathbf{x}_0^1, \dots, \mathbf{x}_0^m\}$ by linearly interpolating the initial and final states.

$$\mathbf{x}_0^i = \frac{i}{m}\mathbf{x}_{\text{fin}} + \left(1 - \frac{i}{m}\right)\mathbf{x}_{\text{init}} \quad (i = 0,1, \dots m)$$

2. Compute the force $\mathbf{F}_k^i$ acting on image $\mathbf{x}_k^i$ $(i = 0,1, \dots m)$

$$\mathbf{F}_k^i = \begin{cases} 0 & i = 0 \text{ or } m \\ -\boldsymbol{\nabla} E(\mathbf{x}_k^i) + 2\left[\boldsymbol{\nabla} E(\mathbf{x}_k^i) \cdot \hat{\boldsymbol{\tau}}_k^i\right]\hat{\boldsymbol{\tau}}_k^i & i = i_{\max} \\ -\boldsymbol{\nabla} E(\mathbf{x}_k^i) + \left[\boldsymbol{\nabla} E(\mathbf{x}_k^i) \cdot \hat{\boldsymbol{\tau}}_k^i\right]\hat{\boldsymbol{\tau}}_k^i + k(\left|\mathbf{x}_k^{i+1} - \mathbf{x}_k^i\right| - \left|\mathbf{x}_k^i - \mathbf{x}_k^{i-1}\right|)\hat{\boldsymbol{\tau}}_k^i & \text{otherwise} \end{cases}$$

where $i_{\max}$ is the subscript of the highest energy image and

$$\hat{\boldsymbol{\tau}}_k^i = \frac{\boldsymbol{\tau}_k^i}{\left|\boldsymbol{\tau}_k^i\right|}$$

$$\boldsymbol{\tau}_k^i = \frac{\mathbf{x}_k^{i+1} - \mathbf{x}_k^i}{\left|\mathbf{x}_k^{i+1} - \mathbf{x}_k^i\right|} + \frac{\mathbf{x}_k^i - \mathbf{x}_k^{i-1}}{\left|\mathbf{x}_k^i - \mathbf{x}_k^{i-1}\right|}$$

3. Update the elastic band using minimization algorithms (e.g. the algorithms in Box 3.1 or Box 3.2)

$$\mathbf{x}_{k+1}^i = \mathbf{x}_k^i + \lambda_k^i \mathbf{d}_k^i \ (i = 1, \dots m) \ \text{(P-R CG)}$$

$$\mathbf{x}_{k+1}^i = \mathbf{x}_k^i + \alpha_k^i \mathbf{p}_k^i \ \ (i = 1, \dots m) \ \text{(L-BFGS)}$$

4. If $\max_i \left\| \mathbf{x}_{k+1}^i - \mathbf{x}_k^i \right\| < \epsilon$, stop. Else, set $k = k + 1$ and go to step 2.

3.2.3.2 String method

The string method [109-111] is very similar to the NEB in that the MEP is approximated by a chain of images. The same potential force projection in the NEB (Equation 3.29) is used to move the images down the potential energy surface perpendicular to the MEP. The one difference between the string and NEB methods is how the images are kept equally spaced along the MEP or by some other specified distribution. In the NEB method, spring forces are introduced between images to ensure equal spacing along the elastic band. In the string method, no spring forces are used. Instead, a cubic spline is used to interpolate the images and the images are redistributed along the spline (with equal spacing or concentrated at the image with the highest energy) after every several iterations. After the convergence of the string, the climbing image force projection scheme in Equation (3.33) is used to find the transition state precisely.

Box 3.4 summarizes the algorithms of the string method. Figure 3.3 is an illustrative example of the string method for the energy landscape of a two-dimensional system.

Box 3.4 String method

Input:

Potential energy function $E(\mathbf{x})$

Initial and final stable states $\mathbf{x}_{\text{init}}$, $\mathbf{x}_{\text{fin}}$

Convergence tolerance ϵ_1, ϵ_2

Maximum number of iterations $j_{\max}$

Output:

Fully relaxed string $\{\mathbf{x}^0, \mathbf{x}^1, \ldots, \mathbf{x}^m\}$

Steps:

1. Set $k = 0$. Initialize the string $\{\mathbf{x}_0^0, \mathbf{x}_0^1, \ldots, \mathbf{x}_0^m\}$ by linearly interpolating the initial and final states.

$$\mathbf{x}_0^i = \frac{i}{m}\mathbf{x}_{\text{fin}} + \left(1 - \frac{i}{m}\right)\mathbf{x}_{\text{init}} \quad (i = 0,1, \ldots m)$$

2. Set $j = 0$.

3. Compute the force $\mathbf{F}_k^i$ acting on image $\mathbf{x}_k^i$ $(i = 0,1, \ldots m)$

$$\mathbf{F}_k^i = \begin{cases} 0 & i = 0 \text{ or } m \\ -\boldsymbol{\nabla} E(\mathbf{x}_k^i) + \left[\boldsymbol{\nabla} E(\mathbf{x}_k^i) \cdot \hat{\boldsymbol{\tau}}_k^i\right]\hat{\boldsymbol{\tau}}_k^i & \text{otherwise} \end{cases}$$

where

$$\hat{\boldsymbol{\tau}}_k^i = \frac{\boldsymbol{\tau}_k^i}{\left|\boldsymbol{\tau}_k^i\right|}$$

$$\boldsymbol{\tau}_k^i = \frac{\mathbf{x}_k^{i+1} - \mathbf{x}_k^i}{\left|\mathbf{x}_k^{i+1} - \mathbf{x}_k^i\right|} + \frac{\mathbf{x}_k^i - \mathbf{x}_k^{i-1}}{\left|\mathbf{x}_k^i - \mathbf{x}_k^{i-1}\right|}$$

4. Update the string using minimization algorithms (e.g. the algorithms in Box 3.1 or Box 3.2)

$$\mathbf{x}_{k+1}^i = \mathbf{x}_k^i + \lambda_k^i \mathbf{d}_k^i \ (i = 1, \ldots m) \ \text{(P-R CG)}$$

$$\mathbf{x}_{k+1}^i = \mathbf{x}_k^i + \alpha_k^i \mathbf{p}_k^i \ (i = 1, \ldots m) \ \text{(L-BFGS)}$$

5. If $\max_i \left\|\mathbf{x}_{k+1}^i - \mathbf{x}_k^i\right\| < \epsilon_1$, go to Step 7. Else, set $k = k + 1, j = j + 1$, and go to step 6.

6. If $j > j_{\max}$, redistribute the images using cubic spline interpolation and go to Step 2. Else, go to 3.

7. Compute the force $\mathbf{F}_k^{i_{\max}}$ acting on the highest energy image $\mathbf{x}_k^{i_{\max}}$

$$\mathbf{F}_k^{i_{\max}} = -\nabla E\left(\mathbf{x}_k^{i_{\max}}\right) + 2\left[\nabla E\left(\mathbf{x}_k^{i_{\max}}\right) \cdot \hat{\boldsymbol{\tau}}_k^{i_{\max}}\right]\hat{\boldsymbol{\tau}}_k^{i_{\max}}$$

8. Update the string using minimization algorithms (e.g. the algorithms in Box 3.1 or Box 3.2)

$$\mathbf{x}_{k+1}^{i_{\max}} = \mathbf{x}_k^{i_{\max}} + \lambda_k^{i_{\max}} \mathbf{d}_k^{i_{\max}} \quad \text{(P-R CG)}$$

$$\mathbf{x}_{k+1}^{i_{\max}} = \mathbf{x}_k^{i_{\max}} + \alpha_k^{i_{\max}} \mathbf{p}_k^{i_{\max}} \quad \text{(L-BFGS)}$$

9. If $\left|E\left(\mathbf{x}_{k+1}^{i_{\max}}\right)/\mathrm{E}(\mathbf{x}_k^{i_{\max}}) - 1\right| < \epsilon_2$, stop. Else, set $k = k + 1$ and go to Step 7.

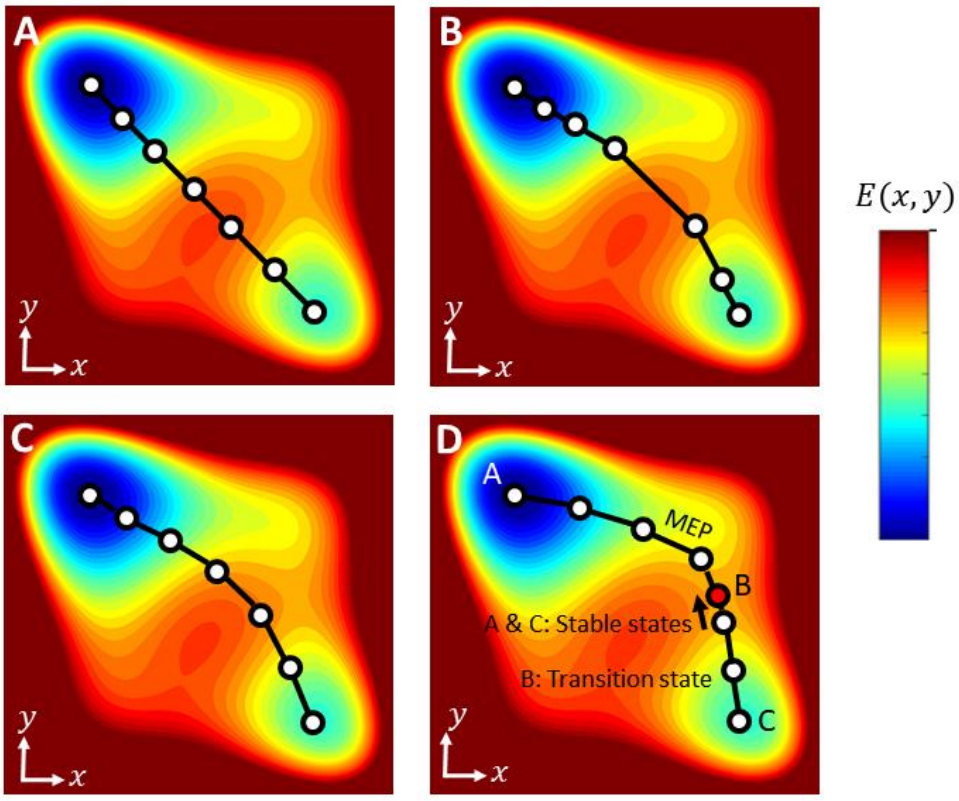

Figure 3.3 Illustrative example of the string method for the energy landscape of a two-dimensional system. (A) Step 1: An initial string of images is formed which linearly interpolates the coordinates of the two local minima. (B) Step 2: Each image in the string is partially relaxed according to the gradient of energy. (C) Step 3: The images are redistributed along the new string

so that the image density is concentrated near the highest energy point along the string. (D) Steps 4 & 5: After the convergence of the iterations, the image with the highest energy is evolved towards the transition state (the red circle).

3.2.4 Implementations in LAMMPS and FORTRAN

I implemented two versions of the discrete thin shell model, one as a user-defined C++ class in LAMMPS and the other as a FORTRAN module. The former version, together with LAMMPS's Polak-Ribière conjugate gradient algorithm and nudged elastic band method, is applied to the spherical cap buckling problem in section 3.5. The latter version is combined with a FORTRAN implementation of the L-BFGS algorithm and string method [112] by Prof. Halim Kusumaatmaja's group at Durham University to survey the energy landscape of cylindrical shell buckling in section 3.6.

The implementation of the discrete thin shell model in LAMMPS is discussed in section 2.4. The Polak-Ribière conjugate gradient minimization algorithm is built in the standard LAMMPS package, and can be invoked through the following commands in a LAMMPS input script:

```
min_style cg
minimize etol ftol maxiter maxeval
```

where etol, ftol, maxiter, maxeval are parameters corresponding to stopping tolerance for energy, stopping tolerance for force, maximum iterations of the minimizer, and the maximum number of energy/force evaluations. The nudged elastic band method can be invoked through the command

```
neb etol ftol N1 N2 Nevery file-style arg keyword
```

where etol, ftol, N1, N2, Nevery are parameters corresponding to stopping tolerance for energy, stopping tolerance for force, the maximum number of iterations to run initial NEB, the maximum

number of iterations to run barrier-climbing NEB, and number of iterations between printing replica energies and reaction coordinates.

The FORTRAN implementation of the discrete thin shell model is provided in Appendix B. It contains subroutines to compute energy, force vector, and hessian matrix (using hyper-dual number method).

3.3 Spherical cap shell buckling

3.3.1 Model system

One of the simplest examples of shell buckling with multiple stable states is exhibited by a spherical cap shell and can be demonstrated by cutting a section of a tennis ball, shown in Figure 3.4. If the section is sufficiently deep, it can be turned inside out and will remain in the inverted state when the loading is removed.

The computational model of this problem is illustrated in Figure 3.5. The undeformed shell (represented by the dark blue arc) is cut from a sphere of radius R, Young's modulus E, Poisson's ratio ν, and thickness t. The angle between the apex and the edge of the shell is denoted as α, represented by the dark blue arc. Its edge is free to rotate but restricted to move within the $z = 0$ plane ($u_z = 0$), and its apex is fixed in the x-y direction ($u_x = u_y = 0$). For a spherical cap with large enough R/t, when probed with an indenter moving down along the z axis, it will snap to an inverted stable equilibrium state (represented by the light blue arc), once the indenter displacement reaches a critical value [113].

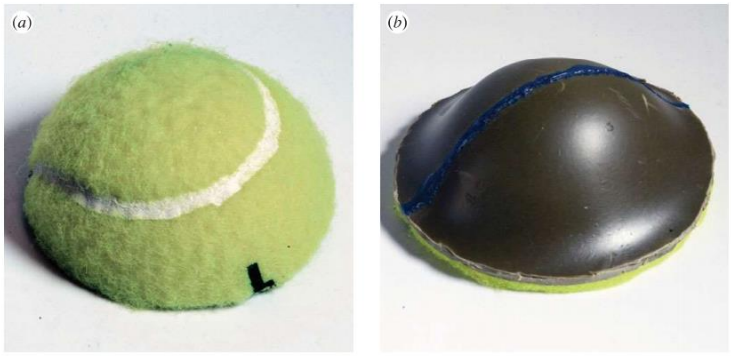

Figure 3.4 The bistability of a spherical cap. Adapted from Reference [113] (a) A section of a tennis ball in its natural state (before being inverted). (b) The same section of a tennis ball as in (a) but now inverted.

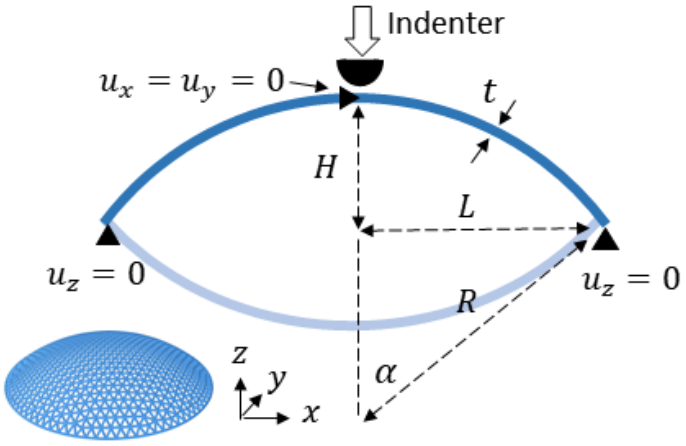

Figure 3.5 Computational model for the bistable buckling of a spherical cap shell.

3.3.2 Dimensionless parameters

Here we derive the key dimensionless parameters of this problem, by considering various energy scales. The bending energy density induced by inversion is

$$\epsilon_b \sim B\left(\frac{1}{R}\right)^2 \tag{3.34}$$

where $B = Et^3/[12(1-\nu^2)]$ is the bending stiffness of the shell. The strain due to inversion estimated by

$$\epsilon \sim \delta^2/l^2 \tag{3.35}$$

with

$$\delta = R(1-\cos\alpha) \sim \alpha^2 R \tag{3.36}$$

being the vertical deflection and

$$l \sim \sqrt{\delta R} \tag{3.37}$$

being the characteristic horizontal length associated with mirror buckling, leading to an estimate of the stretching energy density

$$\epsilon_s \sim Eh\epsilon^2 \sim Eh\alpha^4 \tag{3.38}$$

The relative importance of stretching to bending energy densities is, therefore,

$$\frac{\epsilon_s}{\epsilon_b} \sim \frac{Eh\alpha^4}{B/R^2} = 12(1-\nu^2)\frac{R^2}{h^2}\alpha^4 \tag{3.39}$$

The behavior of shells is more conventionally studied in terms of the fourth root of this parameter [114,115], namely,

$$\lambda_d = [12(1-\nu^2)]^{1/4}\sqrt{\frac{R}{h}}\alpha \tag{3.40}$$

Our goal of this section is to study the behavior of spherical cap shell in terms of two dimensionless parameters λ_d and α using the numerical simulations.

3.3.3 Simulation setup

To understand the geometric conditions under which a spherical cap shell is bistable, and the buckling transition between its stable equilibrium states, we use the LAMMPS implementation of the discrete thin shell model described in section 2.4 to simulate indenting spherical cap shells

of different material properties and geometries (with the parameters listed in Table 3.1). The simulations are carried out in three steps. In the first step, we use a spherical indenter (via the "fix indent" command) to apply a prescribed indentation depth twice the initial height of the spherical cap. The magnitude of the force exerted by the indenter on each node of the discretized shell is

$$F(r) = -K(r - r_0)^2 \tag{3.41}$$

where K is the specified force constant, r is the distance from the node to the center of the indenter, and r_0 is the radius of the indenter. In our simulations, we set $K = 10000$ and $r_0 = 0.1R\sin\alpha$. In the second step, the indenter is removed and the PRCG minimization algorithm (via the "minimize" command) is used to find the closest stable equilibrium state of the shell. If the shell has an inverted equilibrium state, the NEB method (via the "neb" command) is used to find the minimium energy path between the initial and inverted states.

Table 3.1 Parameters for spherical cap shells of different material properties and geometries

E	ν	t	R	α	λ_d
71000	-0.3	1.2475	151	0.2	4
71000	-0.3	0.9857	151	0.2	4.5
71000	-0.3	0.7984	151	0.2	5
71000	-0.3	0.5544	151	0.2	6
71000	-0.3	3.9504	151	0.6	4
71000	-0.3	3.1213	151	0.6	4.5
71000	-0.3	2.5283	151	0.6	5
71000	-0.3	1.7557	151	0.6	6

3.3.4 Results

Figure 3.6 shows the indenter force-displacement curves for different values of λ_d and α, as predicted from our simulations using a discrete shell model (DSM) in LAMMPS and finite element method (FEM) in ABAQUS. Two qualitatively different behaviors can be observed. For $\lambda_d = 5$ and 6, the indenter force initially increases to a maximum, and then decreases to zero, at which point the shell becomes unstable and buckles. Removing the indenter at this point and minimizing the elastic energy the shell will relax into an inverted state. We refer to this regime bistable as the shell has two stable equilibrium states. For $\lambda_d = 4$ and 4.5, the curves have similar shapes, but the indenter force does not decrease to zero. Removing the indenter at any point and minimizing the elastic energy the shell will relax into its natural state. We refer to this regime monostable as the shell has only one stable equilibrium state. We also notice from Figure 3.6 that the maximum indentation force required to buckle the shell increases with λ_d. Therefore, the parameter λ_d characterizes the softness (or hardness) of the shell.

Figure 3.7 summarizes the behaviors of the shells (monostable or bistable) in the (α, λ_d) parameter space. For a given value of α, bistability will be observed when λ_d is larger than a threshold value λ_d^c. The threshold curve $\lambda_d^c(\alpha)$ that separates the monostable and bistable regimes is approximately constant and independent of α. From our simulations, $4.5 < \lambda_d^c < 5$, consistent with the experimental value $\lambda_d^c \approx 4.6$ [113] (represented by the dashed line).

Figure 3.8 compares the energy vs. apex position curves obtained by integrating the force-displacement curve ($\alpha = 0.2$ and $\lambda_d = 5$) in Figure 3.6 with the minimum energy path (MEP) obtained by the string method. We can observe that probing meets the MEP at the transition state B but does not access the MEP generally. The (stable equilibrium) natural state, (unstable equilibrium) transition state, and (stable equilibrium) inverted state are marked with A, B, and C on

the curves, and their deformation profiles (with the radial displacement map in the insert) are shown in Figure 3.9.

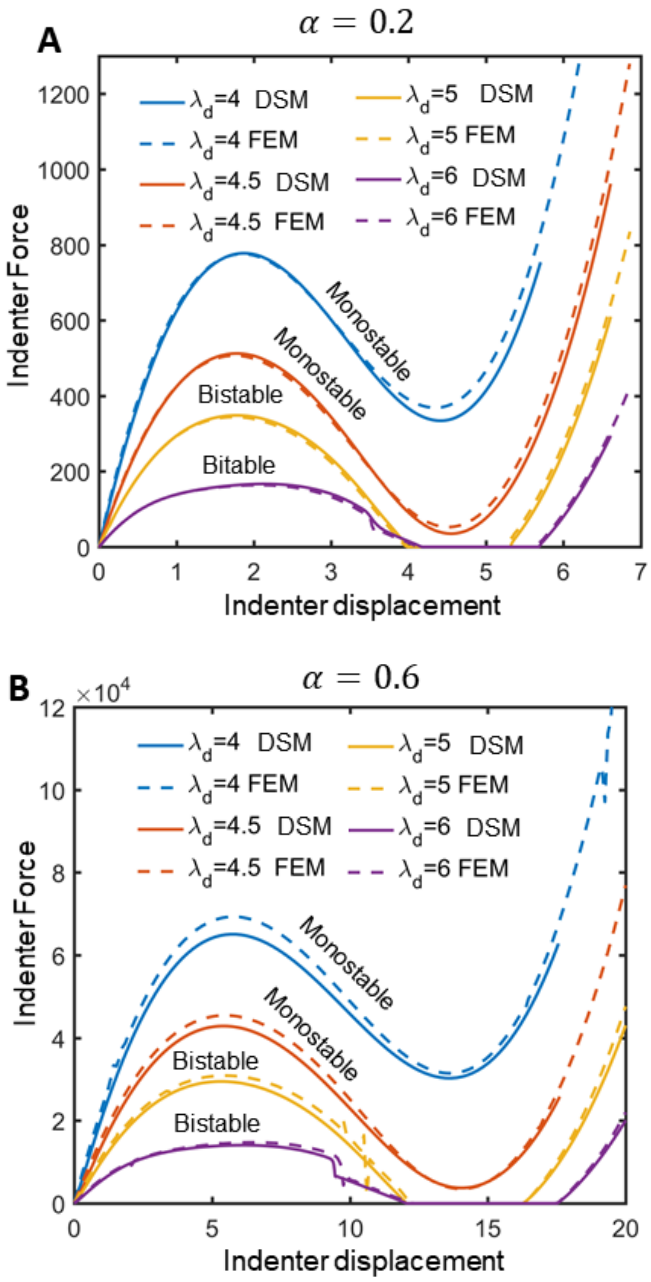

Figure 3.6 The force-displacement relationship for the indentation of a spherical cap shell. The solid line represents the discrete shell model (DSM) simulations in LAMMPS, while the dashed line represents finite element (FEM) simulations in ABAQUS. Different colors corresponds to different values of λ_d. (A) $\alpha = 0.2$ (B) $\alpha = 0.6$.

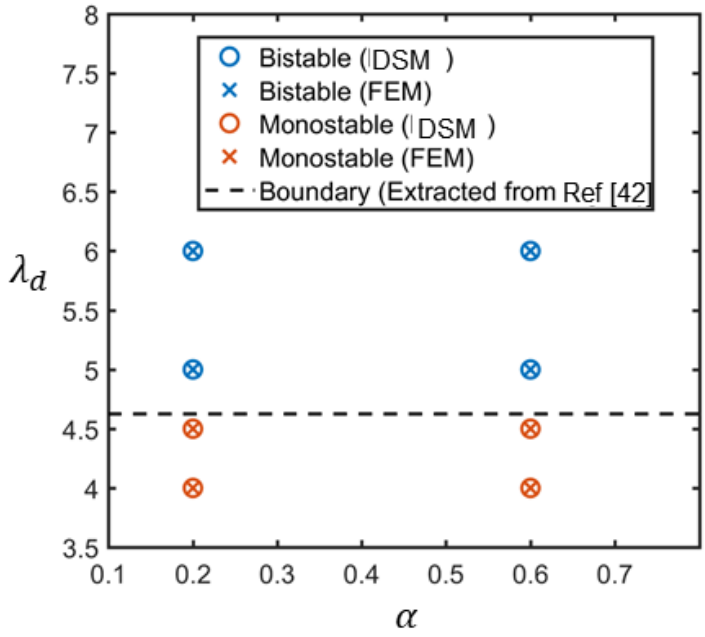

Figure 3.7 Monostable or bistable behaviors of spherical cap shells in the (α, λ_d) parameter space predicted by DSM and FEM simulations.

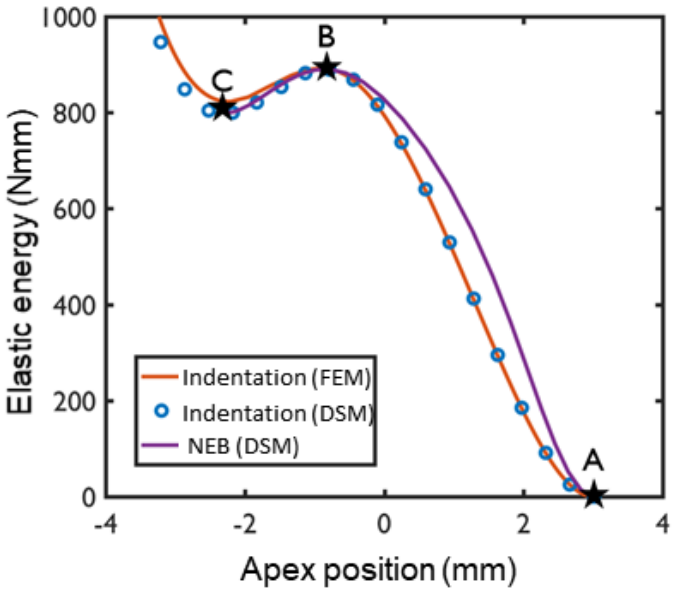

Figure 3.8 Comparison of the energy vs. apex position curves obtained by integrating the force-displacement curve ($\alpha = 0.2$ and $\lambda_d = 5$) in Figure 3.6 with the minimum energy path (MEP) obtained by the string method.

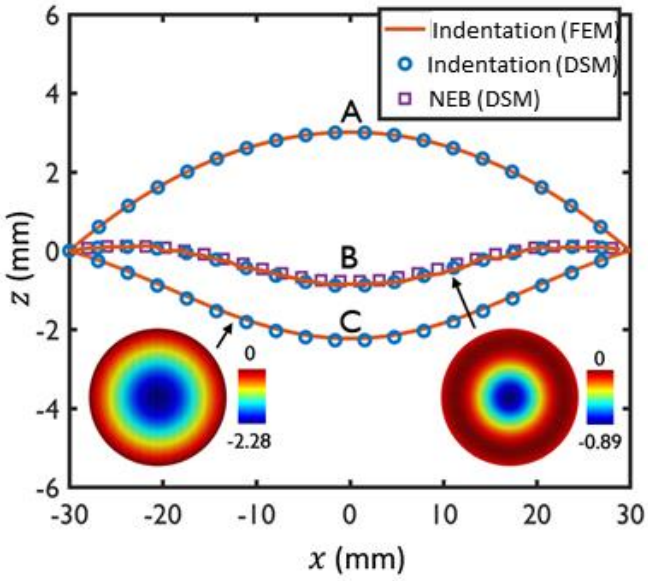

Figure 3.9 Deformation profiles and radial displacement maps corresponding to the three states (A, B and C) on the curves in Figure 3.8.

3.4 Cylindrical shell buckling

3.4.1 Model system

We apply the discrete thin shell model implemented in FORTRAN to the cylindrical buckling problem. Consider a cylindrical shell with radius R_0, length L_0, thickness t, Young's modulus E, and Poisson's ratio ν, as shown in Figure 10. The cylinder is axially compressed by prescribing the displacements at the top and bottom ends (rigid loading). The shortening ratio is defined as $\lambda = L/L_0$, where L is the length of the compressed cylinder. Another two important dimensionless parameters are aspect ratio $A_0 = L_0/(2R_0)$ and relative thickness R_0/t. We fix the relative thickness to be $R_0/t = 247$ which is similar to the relative thickness of aluminum

drink cans ($R_0/t \approx 300$). Throughout this work, we report the dimensionless energy $E_r = 6\sqrt{3}(1-\nu^2)E/(Yt^3)$.

Figure 3.10 The buckling of an axially compressed cylindrical shell

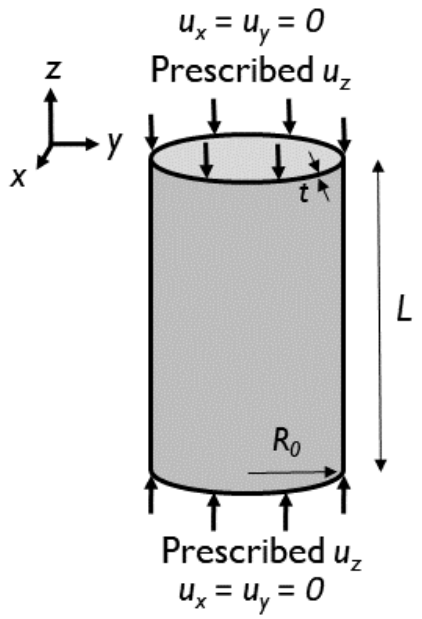

3.4.2 Stable states

The morphologies of the stable states for different aspect ratios A_0 and shortening ratios λ are summarized in Figure 3.11. Three characteristic morphologies are observed: unbuckled, singly dimpled and multiply dimpled. The multiply-dimpled states are the most common, which include highly symmetric Yoshimura-like dimple patterns (Figure 3.11D) [116] and irregular dimple patterns (Figure 3.11E). The phase diagram of global energy minima is shown in Figure 3.11F. At large λ, global minima are the unbuckled states; upon decreasing λ, the multiply-dimpled states become global minima. We observed that the singly dimpled state (Fig. 3.11) is never a global energy minimum, even though it is stable. Single dimple is therefore only metastable. When it is

energetically unfavorable to form a dimple, the unbuckled state is lower in energy; when it is energetically favorable to form a dimple, the energy is always lowered further by subsequent dimpling. This metastability region is outlined in blue in the phase diagram.

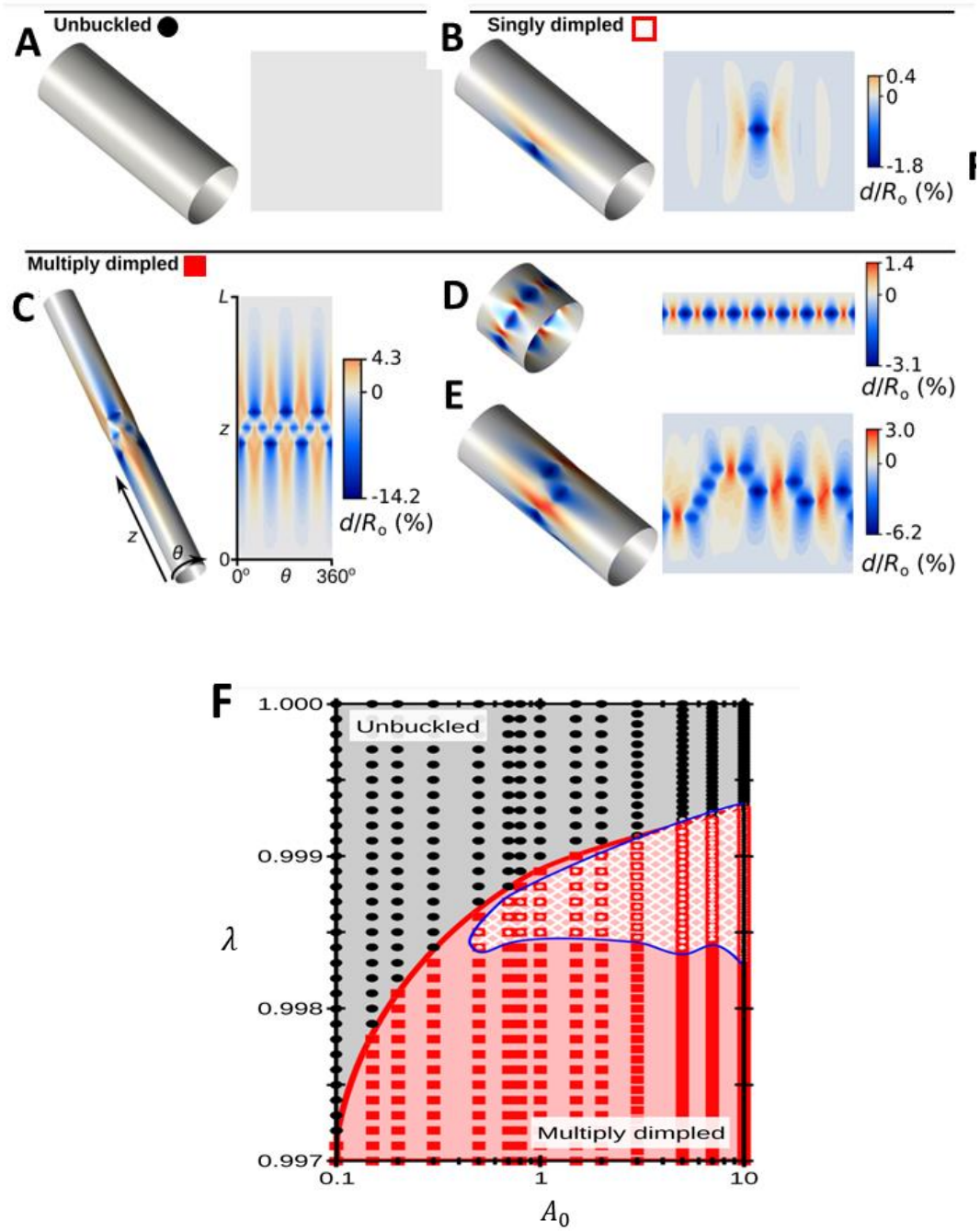

Figure 3.11 Morphologies of the local energy minima for aspect ratios $0.1 < A_0 < 10$ and shortening ratios $0.997 < \lambda < 1$. The relative thickness R_0/t is fixed to be 247. (A–E) Examples of the three characteristic morphologies: unbuckled, singly dimpled and multiply dimpled. The color represents radial displacement. (F) Phase diagram indicating the morphologies of the global energy minima across a range of aspect ratios A_0 and end shortening ratios λ. The global minima are either unbuckled (grey region, simulation data shown as black circles) or multiply dimpled (red region, simulation data shown as red squares). The region outlined in blue indicates metastable singly dimpled states. This figure is adapted from Reference [112].

3.4.3 Transition paths

After obtaining the local energy minima, we connect them with minimum energy paths using the string method. One example is shown in Figure 3.12 for a cylinder of $A_0 = 0.8, \lambda = 0.9986$. We find multiple minimum energy paths connecting the unbuckled state and the 9-dimple global energy minimum, and each path is complex, featuring many intervening local minima. The energy profiles along three of the paths are shown in Figure 3.8B, where the distance s along the path is defined as

$$s = \sum_{i=1}^{N_{\text{nodes}}} \left|\mathbf{a}_i - \mathbf{a}_i^0\right| \tag{3.4}$$

with $\mathbf{a}_i$ and $\mathbf{a}_i^0$ being the position vectors of node i in the buckled and unbuckled mesh, respectively. In path A, the cylinder undergoes a series of dimple-growing transitions starting with the unbuckled state. In the first seven, each transition adds an additional dimple to the cylinder and lowers the energy. The final transition sees two dimples forming simultaneously to complete the ring of nine dimples. In paths B and C, however, the cylinder undergoes transitions unrelated to dimple growing.

Figure 3.12A shows the energy profiles along the three paths for the 0-1 dimple transition, compared with the energy profile obtained by simulating the local probe technique as discussed in Section 3.3.4. We observe that the local probe technique does meet the minimum energy path at the transition state, although it does not coincide with it generally. This comparison shows that the local probe technique is capable of measuring the energy barrier between the unbuckled and post-buckling states for singly dimpled configurations.

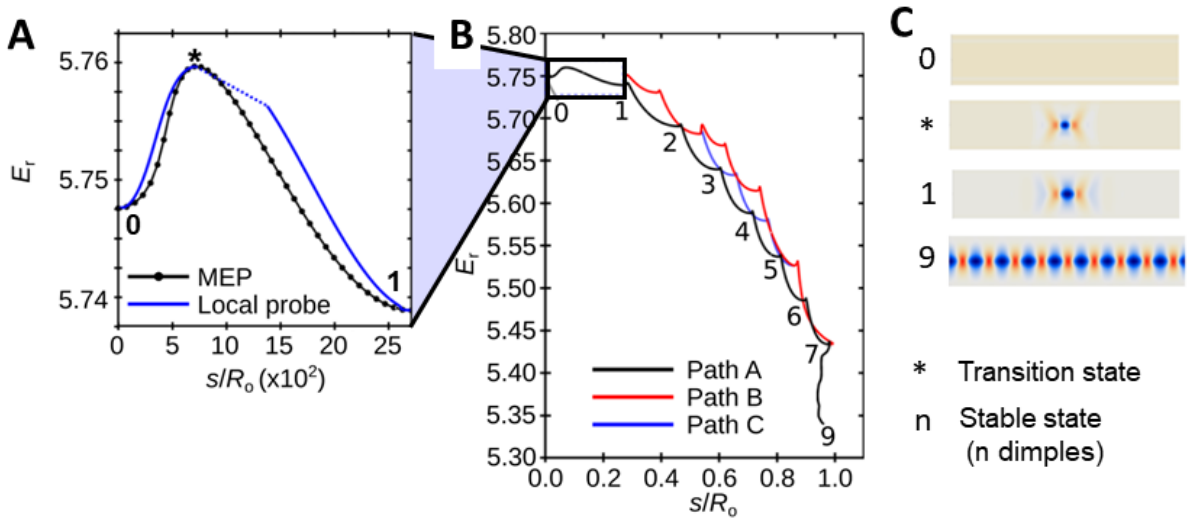

Figure 3.12 Minimum energy paths connecting the unbuckled state and the 9-dimple global energy minimum for a cylinder of $A_0 = 0.8, \lambda = 0.9986$. (A) Energy profiles along the minimum energy paths and local probe path for the 0-1 dimple transition. (B) Three example minimum energy paths connecting the unbuckled and 9-dimple state. The path length s is defined in Equation (3.4). The number of dimples is labelled at each minimum in path A. (C) Radial displacement contour plots for different states. This figure is adapted from Reference [112].

3.4.4 Disconnectivity graphs

In Figure 3.13, the energy landscapes are illustrated as disconnectivity graphs [117-118] for a lightly compressed short cylinder ($A_0 = 0.8, \lambda = 0.9986$), a heavily compressed short cylinder ($A_0 = 0.8, \lambda = 0.9986$), and a lightly compressed long cylinder ($A_0 = 3.0, \lambda = 0.9990$). In a disconnectivity graph, the network of local energy minima and MEPs is reduced to a spanning tree showing only the energy of the minima (the end points of each branch) and the lowest energy barrier connecting any two minima, read by tracing the path between two branches and finding the highest energy point.

In Figure 3. 13A, the disconnectivity graph is presented for the lightly compressed short cylinder. We observe that the unbuckled, singly dimpled, and multiply-dimpled states coexist. However, the energy landscape is rather simple: the minima are uniformly distributed across the energy range. The global minimum (1×9) (highlighted in red) and the second-lowest minimum (1×8) exist in a deep well, with the energy barrier to escape the well greater than that to escape the branch of the unbuckled state (highlighted in blue) by a factor of 7. Thus, if an unbuckled cylinder is subject to perturbations with sufficient energy to overcome the buckling energy barrier, although other stable states exist along the way, the tendency is to quickly become trapped in either the global minimum (1×9) or the second-lowest minimum (1×8).

Figure 3.13B shows the disconnectivity graph for the heavily compressed short cylinder. Here, the landscape is markedly different to the that for the less-compressed cylinder: the distribution of minima is less uniform with the majority of minima concentrated at the lower energy range. Another difference in this disconnectivity graph is that the global minimum (2×9) (high-

lighted in red) does not have a large energy barrier compared to other minima. Thus, random perturbations made to the unbuckled state may result in the system becoming trapped in the states different from the global minimum.

Figure 3.13C is the disconnectivity graph for the lightly compressed long cylinder, in which we have clustered the minima sharing the same number of dimples and having interconversion energy barriers less than 10^{-3}, reducing the number of minima shown by a factor of 10. We observe that this landscape is significantly different from those for the short cylinders: the number of minima has increased by a factor of 100 and the distribution of minima is highly non-uniform. The minima are concentrated in two energy ranges $10.1 < E_r < 10.3$ and $10.4 < E_r < 10.5$, where irregularly arranged dimples are dominant. Thus, the landscape is rough and glassy in those ranges. On the other hand, in the vicinity of the global minimum (2×6) (highlighted in red), the landscape becomes significantly less glassy. Nonetheless, the overall roughness of the landscape coupled with a large number of deep branches means that a perturbed cylinder may buckle to a large number of stable states.

The difference in the roughness of the landscape between short and long cylinders may be explained in the following way. For the short cylinder, the fixed ends tightly constrain the dimples to lie within either one or two rows, due to the characteristic dimple size. For the long cylinder, the constrain of the fixed ends is diminished, yielding a larger number of possibilities of dimple arrangements.

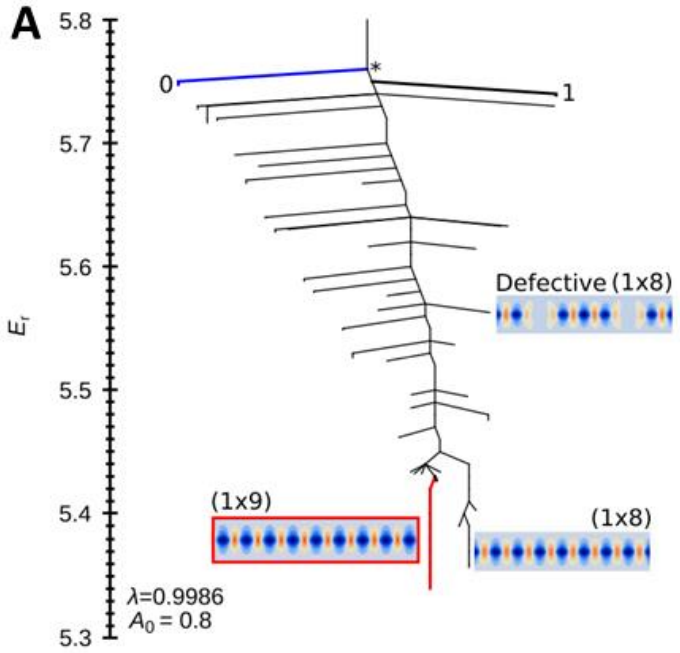
A
5.8
5.7
5.6
5.5
5.4
5.3
E_f
0
*
1
Defective (1x8)
(1x9)
(1x8)
λ=0.9986
A_0 = 0.8

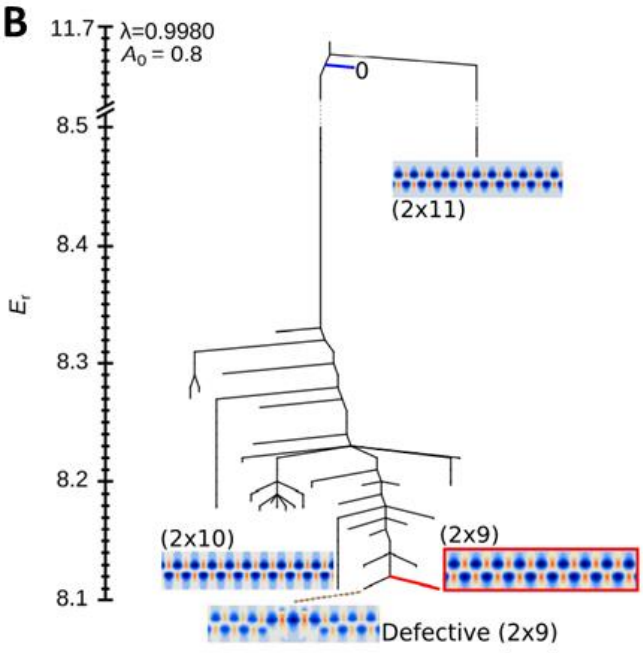
B
11.7
8.5
8.4
8.3
8.2
8.1
E_f
λ=0.9980
A_0 = 0.8
0
(2x11)
(2x10)
(2x9)
Defective (2x9)

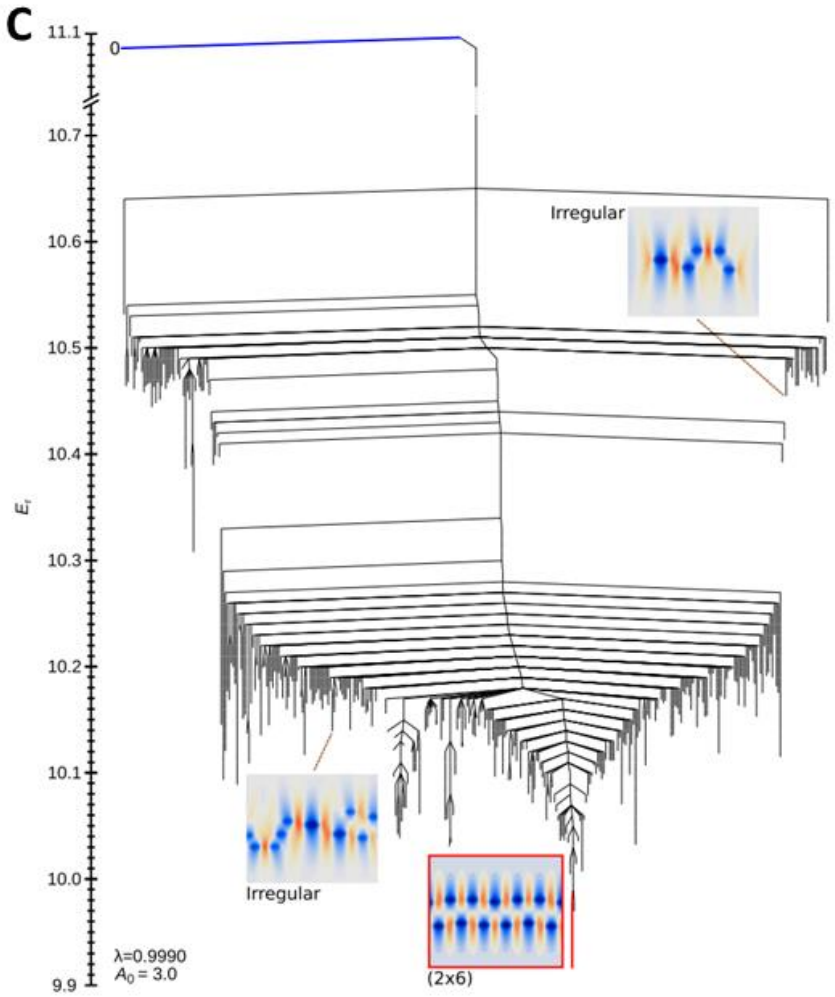

Figure 3.13 Disconnectivity graphs showing the minimum energy barrier between any pair of local energy minima. The branches corresponding to the unbuckled state and the global minimum are colored in blue and red, respectively. Radial displacement plots of the representative minima are also shown. (A) Lightly compressed short cylinder ($A_0 = 0.8, \lambda = 0.9986$). (B) Heavily compressed short cylinder ($A_0 = 0.8, \lambda = 0.9980$). (C) Lightly compressed long cylinder ($A_0 = 3.0, \lambda = 0.999$). This figure is adapted from Reference [112].

3.4.5 Increasing buckling resistance

We now demonstrate how the buckling energy landscapes enable us to increase the buckling resistance of a shell by 20% with almost no increase in weight. Taking the system with $A_0 = 0.8, \lambda = 0.9986$ as an example, for which the landscape is shown in Fig. 3.13A and the minimum energy paths are shown in Figure 3.12, we observe that the energy of the singly dimpled transition state (marked with * in Figure 3.12) determines the energy barrier between its unbuckled state and the global energy minimum. Therefore, to increase buckling resistance with minimum weight gain, it is crucial to energetically penalize a shell deforming into its transition state.

Our method is shown in Figures 3.14B-D. First, we obtain the radial deformation field for the original transition state (Figure 3.14B). Second, we compute the change in elastic energy density E_f when transforming from the unbuckled to the transition state (Figure 3.14C). Third, we energetically penalize the formation of this transition state by locally modifying shell thickness so that thickness is proportional to local energy density change and the total mass increase is 1%. Due to the symmetry of the transition state, to suppress dimple formation anywhere around the circumference, at each z we average the thickness profile over all θ. The final relative thickness profile is shown in Fig. 3.14D.

The transition state after local thickness modification is now forced off-center (Fig. 3.14E). The energy profile for this transition is shown as the solid red line in Fig. 3.14A, showing that for a 1% increase in mass, a 20% increase in buckling resistance is achieved. This improvement is over twice that of a uniformly thickened cylinder, 9%, with the same mass increase, the transition profile for which is shown as the dotted black line.

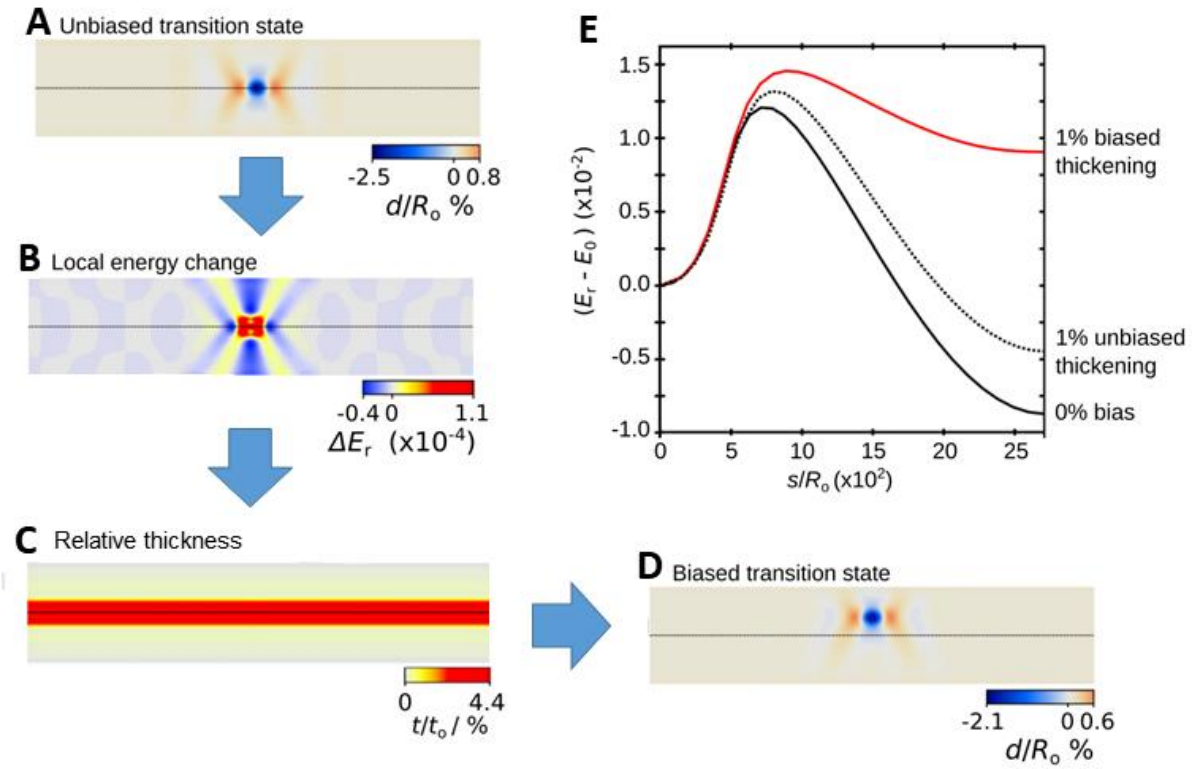

Figure 3.14 The workflow to increase shell stability and its effect for $A_0 = 0.8, \lambda = 0.9986$. (A) Radial displacement field of the original transition state. (B) Change in the energy density of the transition state relative to the unbuckled cylinder. (C) Relative thickness profile of the modified cylinder. (e) The transition state of the modified cylinder. (a) Energy profiles of the unbuckled to single dimple minimum energy paths for the unmodified and modified cylinders. This figure is adapted from Reference [112].

3.4.6 Stabilizing post-buckling state

We now demonstrate how to stabilize a post-buckling state for the system with $A_0 = 0.8, \lambda = 0.9986$. We observe the landscape shown in Figure 3.13A to exhibit a deep global minimum (1×9) and the shallower (1×8) state. Here, we show how to make sure the shell buckle into the (1×8) state that is highly resistant to lateral perturbation.

Figures 3.15A-B show the radial displacement field and the corresponding elastic energy density of the (1×8) state. We then energetically encourage the formation of the (1×8) state by locally modifying the shell thickness so that thickness is inversely proportional to energy density and there is no overall mass change. The thickness biasing amplitude is defined as

$$\beta = t_{\max}/t_{\min} - 1 \tag{3.5}$$

where $t_{\max}$ and $t_{\min}$ are the maximum and minimum shell thickness, respectively.

Figure 3.15C shows how the landscape changes at the bottom of the funnel with β increasing from 0 to 20%. At $\beta = 5\%$, the landscape changes significantly relative to $\beta = 0\%$: the landscape is simplified as the biasing destabilizes many local minima, and the barrier out of the (1×8) state increase by 207% relative to the $\beta = 0\%$ landscape. At $\beta = 10\%$, these effects are further magnified. At 20% bias, the stabilization of the (1×8) state and destabilization of the (1×9) state continues. This leads to a barrier increase of 302% for the (1×8) state, and a barrier decrease of 91% for the (1×9) state.

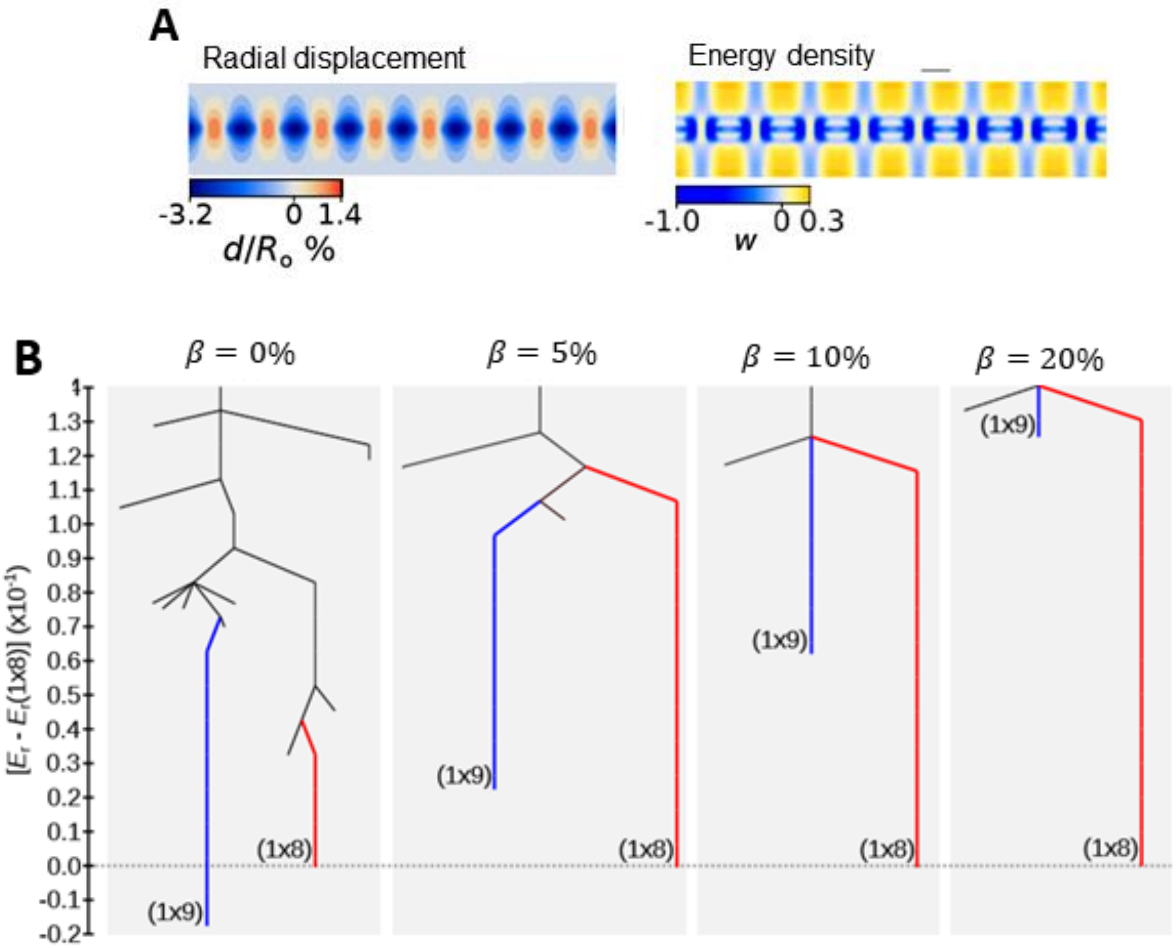

Figure 3.15 (A) radial displacement field and the corresponding elastic energy density of the (1×8) state for $A_0 = 0.8, \lambda = 0.9986$. (B) Evolution of the bottom of the landscape as the biasing amplitude increases, all energies shown relative to the (1×8) state. This figure is adapted from Reference [112].

3.5 Summary

In this work, a discrete shell model was used to evaluate the elastic energy of thin shells under large geometrically nonlinear deformation. This was combined with efficient energy minimization and path finding algorithms to fully describe the energy landscapes of shell buckling.

The discrete shell model was first implemented as a C++ class in LAMMPS. Using LAMMPS's built-in energy minimization and path-finding algorithms, our method was applied to the problem of indenting spherical cap shells. Two qualitatively different regimes are observed. The first is the bistable regime in which the shell remains in the inverted state the removal of the indenter. The second is the monostable regime in which the shell returns to the natural state after the removal of the indenter. We found that whether the shell is in the monostable or bistable regime depends on a single parameter λ_d.

I also implemented the discrete shell model in FORTRAN and collaborated with Prof. Halim Kusumaatmaja's group at Durham University to survey the energy landscape of cylindrical shell buckling under axial compression. To begin with, we surveyed the local energy minima, observing unbuckled, singly dimpled, and multiply dimpled states. The string method was used to find the minimum energy paths connecting pairs of minima and the transition states between them. We then illustrated the buckling energy landscapes as disconnectivity graphs, in which the landscapes became complex and glassy when increasing the aspect ratio or featured many deep states when increasing the compressive strain. Finally, we demonstrate methods to control energy landscapes by first showing how locally modifying shell thickness to energetically penalize the singly dimpled transition state produces a 20% increase in buckling resistance of the unbuckled cylinder for a 1% increase in mass. We then show how local thickness modification to energetically

favor a multiply dimpled post-buckling state simplifies the local landscape, tripling the targeted state stability with no mass change.

Our computational framework to survey the energy landscapes for shell buckling has potential applications in the design of robust thin shell structures or buckling-induced smart applications, ranging from energy harvesting devices [119] to morphable 3D structures [120].

Chapter 4: Multiscale Wrinkle Patterns of Annular Sheets

4.1 Introduction

Thin sheets often develop wrinkles to suppress compression generated by a broad range of conditions such as boundary loads [121], geometric incompatibility [122-124], differential swelling [125], expansion on soft substrates [126,127], and growth in confined spaces [128,129]. A simple 1D wrinkle model is a uniaxially compressed sheet lying on a solid or liquid substrate, resulting in a wrinkle pattern with uniform wrinkle wavelength λ and direction $\hat{\mathbf{n}}$ (Figure 4.1). The wrinkle wavelength λ can be obtained by minimizing the sum of bending energy of sheet and energy associated with substrate deformation [121,130]:

$$\lambda = 2\pi(B/K_{\mathrm{sub}})^{1/4} \tag{4.1}$$

where B is the bending modulus of sheet and K_{sub} is the substrate stiffness. However, most experimental setups for wrinkles differ significantly from such a simplistic 1D model, resulting in complex multiscale wrinkle patterns, where either the direction $\hat{\mathbf{n}}$ or the wavelength λ is nonuniform (Figure 4.2).

Here we consider a special case of radially oriented wrinkles with a local wavelength determined by Equation (4.1). We study a simple model for radially oriented wrinkles, the Lamé setup, consisting of an annular sheet attached to a liquid substrate subjected to radial tensile loads on its edges. There are several advantages in studying this setup: its axisymmetric geometry and boundary conditions make theoretical analysis [135-137] possible, and its experiments can be performed by placing a liquid drop on a circular sheet floating on a liquid bath (Figure 4.2A) [138].

Previous theoretical [136,137] and experimental works [131,135] on the Lamé setup have been dedicated to the defect-free regime where annular sheets develop wrinkle patterns with spatially constant wrinkle numbers m_0 and nonconstant wavelength $\lambda(r) = 2\pi r/m_0$ (Figure 4.3A). Our work addresses a distinct new defect-rich regime where wrinkle patterns exhibit nearly spatially constant wavelength $\lambda \approx \lambda_0$ and nonconstant wrinkle number $m(r) \approx 2\pi r/\lambda_0$ (Figure 4.3B). Our theoretical, experimental, and simulation results show that the prominent features of this new regime are modulations of the wrinkle amplitude and the proliferation of defect-rich regions where the number of wrinkles varies sharply.

This chapter is organized as follows. In section 4.2, we review the Lamé setup and define three governing dimensionless parameters. In section 4.3, we outline our theoretical approach to analyze and predict wrinkle patterns of the Lamé setup. In section 4.4, we provide a detailed description of the simulations and review the experimental setup, and compare their results with the theoretical predictions. In section 4.5, we conclude this chapter with some discussions of our work.

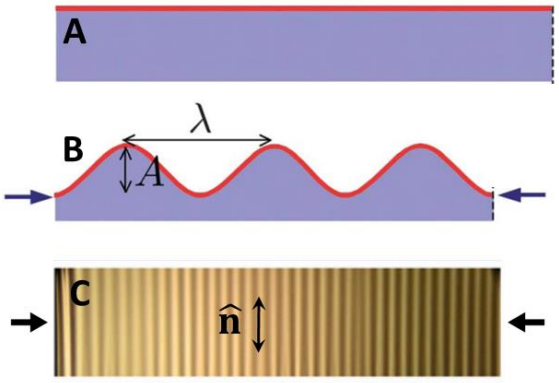

Figure 4.1 A simple 1D model for wrinkling: a uniaxially compressed sheet lying on a solid or liquid substrate, resulting in a wrinkle pattern by uniform wrinkle wavelength λ and direction **n̂.**

(A) Side view of a unwrinkled sheet (B) Side view of a wrinkled sheet (C) Top view of a wrinkled sheet

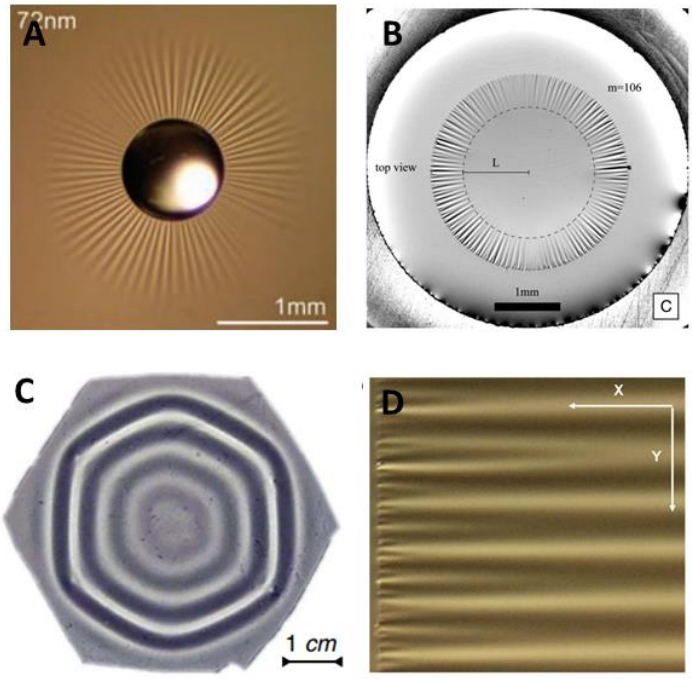

Figure 4.2 (A) A floating polymer film wrinkles under the capillary force exerted by a drop of water placed on its surface. Adapted from Reference [131]. (B) A circular polystyrene (PS) sheet placed on the free surface of the water at the top of a tube wrinkles due to geometric incompatibility between the sheet and liquid surface. Adapted from Reference [132]. (C) A spherical thin shell laid atop a flat body of water wrinkles as a means to overcome the geometric incompatibility. Adapted from Reference [133]. (D) An ultrathin polymer sheet floating on fluid forms a periodic pattern of parallel wrinkles when subjected to uniaxial compression. The wave number of the wrinkle pattern increases sharply near the fluid meniscus. Adapted from Reference [134].

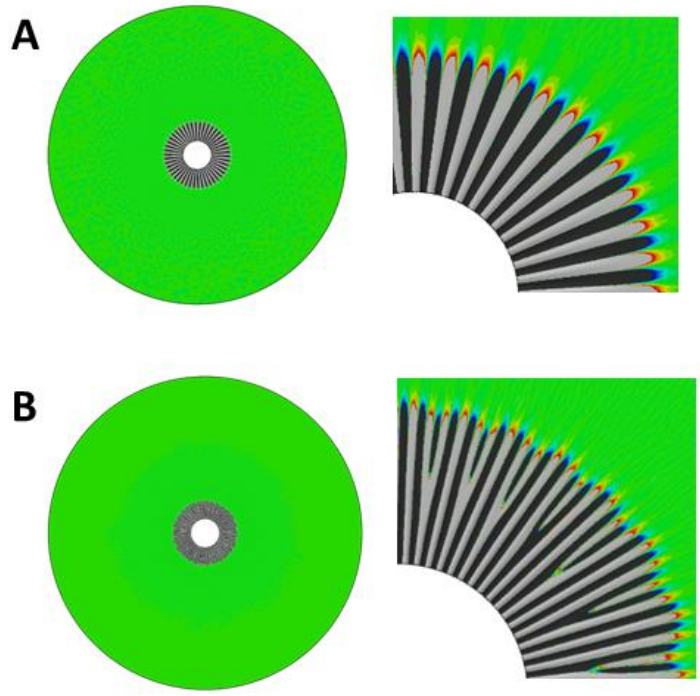

Figure 4.3 Wrinkle patterns observed in simulations of the Lamé setup. (A) Defect-free pattern exhibits spatially constant wrinkle numbers m_0 and nonconstant wavelength $\lambda(r) = 2\pi r/m_0$. (B) Defect-rich pattern exhibits nearly spatially constant wavelength $\lambda \approx \lambda_0$ and nonconstant wrinkle number $m(r) \approx 2\pi r/\lambda_0$.

4.2 Model system

The Lamé setup is shown schematically in Figure 4.4, where an annular sheet of thickness t and radii $R_{\text{in}} \ll R_{\text{out}}$ is attached to a liquid substrate of stiffness $K = \rho g$ (with ρ being the density of liquid bath), subjected to radial tensile loads γ_{in} and γ_{out} at the inner and outer edges, and hydrostatic pressure $p = -\rho g \zeta$ (with ζ being the out-of-plane deflection of the sheet) exerted by the liquid. The stretching and bending moduli of the sheet are $Y = Et$ and $B = Et^3/(12(1 - \nu^2)$, where E and ν are Young's modulus and Poisson's ratio.

The problem is governed by three dimensionless groups:

$$\tau = \frac{\gamma_{\text{in}}}{\gamma_{\text{out}}} \tag{4.2}$$

$$\epsilon^{-1} = \frac{\gamma_{\text{in}} R_{\text{in}}^2}{B} \tag{4.3}$$

$$B_o = \frac{K_{\text{sub}} R_{\text{in}}^2}{\gamma_{\text{in}}} \tag{4.4}$$

where τ, ϵ^{-1} and B_o characterize the ratio of tensile loads, the relative bendability of sheet, and the relative substrate stiffness. Here we study thin, highly bendable sheets ($\epsilon^{-1} \gg 1$) with strong substrate stiffness ($B_o \gg 1$) so that the wrinkle pattern is in the defect-rich regime where wrinkle wavelength is uniform [10,15] (Figure 4.3B).

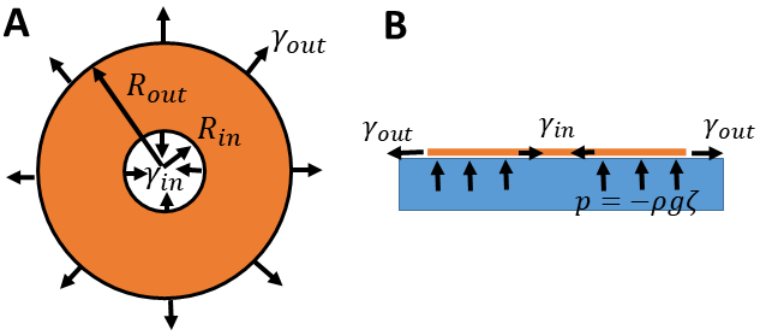

Figure 4.4 The Lamé setup: an annular sheet is attached to a liquid substrate subjected to radial tensile loads at the inner and outer edges. The liquid substrate exerts hydrostatic pressure on the sheet. The magnitude of the pressure is proportional to the out-of-plane deflection of the sheet.

4.3 Theoretical analysis

In this section, we describe our theoretical approach to the Lamé problem for highly bendable sheets ($\epsilon^{-1} \gg 1$) with strong substrate stiffness ($B_o \gg 1$). Our analysis is divided into four parts. In the first and second part, we briefly review the classical unwrinkled solution and the

tension field theory of the Lamé problem. In the third and fourth part, we construct an ansatz with constant wrinkle amplitude to recover Equation (4.1) for wrinkle wavelength and an ansatz with modulated wrinkle amplitude to derive its oscillatory period. Throughout this section, we simplify the expression by assuming $R_{\text{in}} \ll R_{\text{out}}$ and taking the Poisson's ratio $\nu = 0$, recalling that the Poisson's ratio does not affect the wrinkle pattern [137,139].

4.3.1 Linear elastic solution

In the classical linear elastic solution to the Lamé problem, the annular sheet is in an unwrinkled planar state. The radial and hoop stress components and the radial displacement field are given by [140]:

$$\sigma_{rr} = \gamma_{\text{in}} \left[\frac{R_{\text{in}}^2}{r^2} \left(1 - \frac{1}{\tau} \right) + \frac{1}{\tau} \right] \tag{4.5}$$

$$\sigma_{\theta\theta} = \gamma_{\text{in}} \left[\frac{R_{\text{in}}^2}{r^2} \left(-1 + \frac{1}{\tau} \right) + \frac{1}{\tau} \right] \tag{4.6}$$

$$u_r = \frac{\gamma_{\text{in}}}{Y} \left[\left(-1 + \frac{1}{\tau} \right) \frac{R_{\text{in}}^2}{r} + \frac{r}{\tau} \right] \tag{4.7}$$

The total elastic energy (including the strain energy and the work done by the boundary loads) of the system is:

$$U^{\text{Lamé}} = -\frac{\pi R_{\text{in}}^2 \gamma_{\text{in}}^2}{Y} \left(-1 + 2 \left(\frac{1}{\tau} - 1 \right)^2 + \frac{R_{\text{out}}^2}{R_{\text{in}}^2} \frac{1}{\tau^2} \right) \tag{4.8}$$

In the above solution, the radial stress is always in tension ($\sigma_{\theta\theta} > 0$) but the hoop stress becomes compressive ($\sigma_{\theta\theta} < 0$) in the zone $R_{\text{in}} < r < L^{\text{Lamé}} = \sqrt{\tau - 1} R_{\text{in}}$ for $\tau > 2$. Hence, for highly bendable sheets we study here, the unwrinkled state is unstable to the formation of radial wrinkles that relieve the compressive stress when τ is slightly above 2.

4.3.2 Tension field theory

Tension field theory (TFT) describes the stress and displacement field for highly bendable thin sheets ($\epsilon^{-1} \gg 1$) in the wrinkled state, at which the sheet cannot support any compressive stress, resulting in a purely tensile stress field. For the Lamé problem, the radial and hoop stress components and the radial displacement in the wrinkled zone $R_{\text{in}} < r < L = \tau R_{\text{in}}/2$ are given by [136,137]:

$$\sigma_{rr} = \frac{\gamma_{\text{in}} R_{\text{in}}}{r} \tag{4.9}$$

$$\sigma_{\theta\theta} = 0 \tag{4.10}$$

$$u_r = \frac{\gamma_{\text{in}}}{Y}\left[\left(-1 + \log\left(\frac{r}{L}\right)\right) R_{\text{in}} + \frac{2}{\tau} L\right] \tag{4.11}$$

The fractional arclength "wasted" by wrinkle undulations in a latitude of radius r in the wrinkled zone is:

$$\Phi^2(r) = -\frac{u_r}{r} = 2\left(\frac{\gamma_{\text{out}}}{Y}\right)\left(\frac{L}{r}\right)\log\left(\frac{L}{r}\right) \tag{4.12}$$

The total elastic energy (including the membrane strain energy and the work done by the boundary loads, ignoring the bending energy as it is negligible for a highly bendable thin sheet) of the system is:

$$U_{\text{dom}} = -\frac{\pi R_{\text{in}}^2 \gamma_{\text{out}}^2}{Y}\tau^2\left(-\frac{1}{2} + \log\frac{\tau}{2} + \frac{R_{\text{out}}^2}{R_{\text{in}}^2}\frac{1}{\tau^2}\right) \tag{4.13}$$

The total elastic energy in the tension field theory (Equation (4.13)) is lower than its counterpart in the linear elastic solution (Equation (4.8)), therefore justifying the use of tension field theory to describe the stress and displacement field in the wrinkled sheet.

4.3.3 FvK theory

The FvK (Föppl–von Kármán) theory describes the large out-of-plane deflections of thin flat plates (or sheets) under the kinematic assumptions that (1) the shear deformation is negligible, (2) the strain in the sheet is small, and (3) the deflection is characterized by small slopes everywhere.

The first FvK equation describes the out-of-plane force balance and is given by:

$$\left(B\frac{1}{r^4}\frac{\partial^4}{\partial\theta^4}-\sigma_{\theta\theta}\frac{1}{r^2}\frac{\partial^2}{\partial\theta^2}-\sigma_{rr}\frac{\partial^2}{\partial r^2}+K_{\text{sub}}\right)\zeta(r,\theta)=0 \tag{4.14}$$

where $\zeta(r,\theta)$ is the out-of-plane deflection, and $\sigma_{\theta\theta},\sigma_{rr}$ are the in-plane stress components. The total energy consists of in-plane strain energy U_{strain}, bending energy U_{bend}, and substrate deformation energy U_{subst}:

$$U_{\text{strain}}=\int \epsilon_{ij}\sigma_{ij}\,dA \tag{4.15}$$

$$U_{\text{bend}}\approx\int\frac{B}{2}\text{tr}(\kappa)^2\,dA \tag{4.16}$$

$$U_{\text{subst}}=\int\frac{K}{2}\zeta^2\,dA \tag{4.17}$$

where κ is the curvature tensor whose components are approximated as:

$$\kappa_{rr}=\partial_{rr}^2\zeta \tag{4.18}$$

$$\kappa_{\theta\theta}=\frac{1}{r}\partial_r\zeta+\frac{1}{r^2}\partial_{\theta\theta}^2\zeta \tag{4.19}$$

$$\kappa_{r\theta}=2\partial_{r\theta}^2\zeta \tag{4.20}$$

4.3.4 Constant wrinkle amplitude

We first assume the out-of-plane deflection takes the following form in each narrow annulus $r\in r_a\pm l_\perp$ within the entire annular sheet, where $l_\perp\ll r_a$ and $R_{in}<r_a<L$:

$$\zeta(r,\theta) = \Psi(r)\cos(m\theta) \tag{4.21}$$

where

$$\sigma_{\theta\theta}(r) = -\left[B\left(\frac{m}{r}\right)^2 + K\left(\frac{m}{r}\right)^{-2}\right] \tag{4.22}$$

Here the assumed deflection curve features a constant amplitude $\Psi(r)$ with wrinkle number m for any fixed r, as plotted in Figure 4.5B. The resulting energy of bending and substrate deformation after using Equations (4.16) and (4.17) is

$$U_m \approx \bar{C} + \frac{1}{2}B\int d\theta \int dr\ \Psi(r)^2 r^{-3} m^2 \left(m - \bar{m}(r)\right)^2 \tag{4.23}$$

where

$$\bar{m}(r) = \frac{2\pi r}{\bar{\lambda}}\ ; \tag{4.24}$$

$$\bar{\lambda} = 2\pi\left(\frac{B}{K_{sub}}\right)^{\frac{1}{4}}, \tag{4.25}$$

and $\bar{C}$ is a constant $\sim \sqrt{BK_{sub}}$. Minimizing U_m over integers m in a sufficiently narrow annulus, $l_\perp \ll r_a$, yields

$$m \approx m_a = 2\pi r_a/\bar{\lambda} \tag{4.26}$$

thus recovering Equation (4.1).

Even though the assumed deflection Equation (4.21) with constant amplitude successfully predicts the wrinkle wavelength, it does not indicate how transitions occur between distinct values of m_a at adjacent narrow annuli. We will overcome this difficulty in the next section by assuming the deflection modulated by an oscillating amplitude.

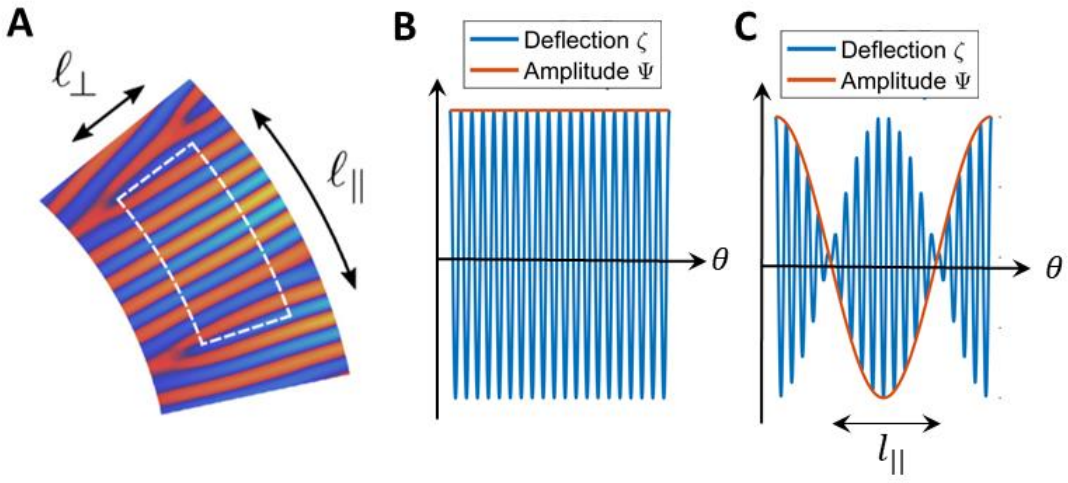

Figure 4.5 (A) Schematic of a defect-rich wrinkle pattern where $l_\perp$ is the width of the narrow annular zone and $l_{||}$ is the width of the defect-free area. Adapted from Reference [143] (B) Schematic of the deflection $\zeta(r,\theta)$ with the constant amplitude $\Psi(r)$ at a given r. (C) Schematic of the deflection $\zeta(r,\theta)$ modulated by the oscillating amplitude $\Psi(r,\theta)$ at a given r.

4.3.5 Modulated wrinkle amplitude

We generalize the deflection (4.21) to:

$$\zeta(r,\theta) = \Psi(r,\theta)\cos(m_a\theta) \tag{4.27}$$

where $m_a = 2\pi r_a/\bar{\lambda}$ and $\bar{\lambda}$ is given by Equation (4.25). In contrast to the deflection (4.21), Equation (4.27) admits azimuthally oscillatory solutions to the wrinkle amplitude, facilitating a transition mechanism between distinct integer values of m_a at adjacent annuli, so that defects can nucleate within the amplitude-suppressed zones ($\Psi(r,\theta_a) \approx 0$) at negligible energy cost. For the deflection (4.27), the avoidance of resonant effects in a perturbative expansion of Equation (4.14) implies the equation

$$\left[\sigma_{rr}\frac{\partial^2}{\partial r^2} + 4|\sigma_{\theta\theta}|\frac{1}{r^2}\frac{\partial^2}{\partial\theta^2}\right]\Psi(r,\theta) = 0 \tag{4.28}$$

Within a narrow, defect-free annulus around $r = r_a$, a solution to Equation (4.28) may be approximated by:

$$\Psi \propto e^{-2\pi\sqrt{\frac{|\sigma_{\theta\theta}|}{\sigma_{rr}(r_a)}}\frac{(r-r_a)}{l_\parallel}} \cos\left(\frac{\pi r_a \theta}{l_\parallel}\right) \tag{4.29}$$

where $l_\parallel$ is the width of the defect-free area (Figure 4.5A).

Using Equations (4.15)-(4.17) and Equation (4.29), we obtain the energy U_m (Equation 4.23) and two other terms:

$$U_\Psi \approx \frac{1}{2}\int d\theta \int r dr \left(\sigma_{rr}|\partial_r \Psi|^2 + 4|\sigma_{\theta\theta}|\frac{1}{r^2}|\partial_\theta \Psi|^2\right) \tag{4.30}$$

$$U_{\text{nonlin}} \approx \frac{Y}{2}\int d\theta \int r dr \left[\frac{m^2|\Psi|^2}{4r^2} - \Phi^2(r)\right]^2 + \frac{m^2}{4r^4}|\Psi|^4\left(\frac{\partial_{\arg}\Psi}{\partial\theta}\right)^2 \tag{4.31}$$

where Φ, σ_{rr}, $\sigma_{\theta\theta}$ are given by Equations (4.12), (4.9) and (4.22).

For a small, defect-free zone of azimuthal and radial extents, $l_\parallel,\ l_\perp \ll r_a$, respectively, the second term in Equation (4.31) indicates that strain is induced by any deviation of wrinkles from the tension-carrying lines (i.e. radials, for which $\frac{\partial_{\arg}\Psi}{\partial\theta} = 0$), hence the radial orientation of wrinkles persists in defect-free zones, locally suppressing the smectic order imparted by uniformly-spaced wrinkles (for which $\frac{\partial_{\arg}\Psi}{\partial\theta} \approx \bar{m}(r) - m_a$). In contrast, the first term in Equation (4.31) does not vanish for any azimuthally-oscillating amplitude, but its cost can be made negligible by requiring the corresponding integrand and its radial derivative to vanish upon integrating over an oscillatory period of Ψ, yielding:

$$l_\parallel \approx 4\pi^2 l_{BC}^* \frac{l_{bend}^*}{\bar{\lambda}}, \tag{4.32}$$

where

$$l_{bend}^{*} = \left(\frac{1}{r_a} + \left| \frac{\Phi'(r_a)}{\Phi(r_a)} \right| \right)^{-1} \tag{4.33}$$

4.4 Simulation

4.4.1 ABAQUS setup

We perform finite element simulations in ABAQUS/Explicit using 3-node linear shell elements (S3R) with geometric nonlinearity turned on. The liquid substrate is modeled as a pressure exerted on the sheet whose magnitude is proportional to the out-of-plane deflection of the element. The deflection-dependent liquid pressure is implemented through the user-defined subroutine for load distribution. A fine mesh is adopted near the inner edge with gradually increasing element sizes towards the outer edge, and large-scale simulations with 1 to 14 million elements are required, to capture a large number of wrinkles. After applying a small initial pressure on the entire sheet to trigger buckling, we run the simulations dynamically with decreasing pressure and fictitious material damping until the wrinkle patterns relax to stable states.

4.4.2 Model validation tests

4.4.2.1 Thin film folding tests

Figure 4.6A is a setup to verify our approach of modeling liquid substrate as a pressure proportional to deflection, where a thin rectangular film on the initially flat liquid surface is confined in one horizontal direction [142]. The thin film responds to confinement first by wrinkling and then by folding, resulting from the competition between the bending energy to deform the film and the gravitational energy to lift the liquid. We compare the total energy of the system and the configurations of the thin film at different confinement levels obtained from our ABAQUS simulations with the analytical solutions and the discrete model simulations obtained from Reference [142] in Figure 4.6B. The good agreement of ABAQUS results with the reference shows

that a pressure proportional to displacement can accurately model liquid substrate. This also confirms that the developed simulation model can capture highly nonlinear deformation of the floating film systems.

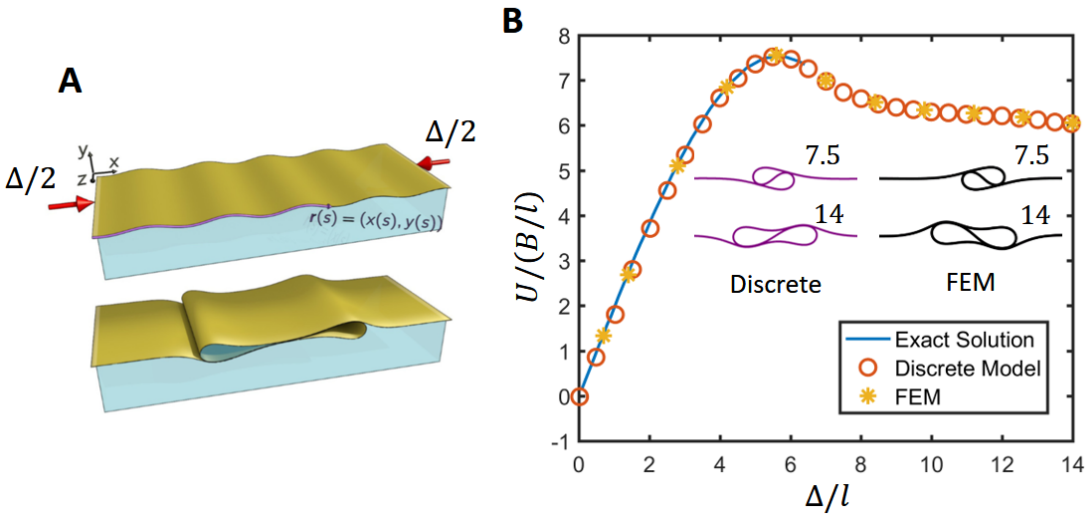

Figure 4.6 (A) A thin film on an initially flat liquid surface responds to uniaxial confinement first by wrinkling (top) and then by forming a large fold (bottom). Adapted from Reference [142]. (B) Normalized total energy U (sum of bending and gravity energies) of the buckled films as functions of normalized confinement length Δ, obtained from the analytical solutions and discrete model simulations in Reference [142], along with our ABAQUS results. Inset: Configurations of thin films when $\Delta/l = 7.5$ and 14 for ABAQUS and discrete model simulations.

4.4.2.2 Scaling laws tests

Figures 4.7 and 4.8 present our simulation results to test the scaling laws $m \sim r_i(\rho g/B)^{1/4}$ [135] in the gravity-dominated regime and $m \sim \epsilon^{-1/4}$ [136] in tension-dominated regime [136] for the number of wrinkles in Lamé setup. The parameters of each test are listed in Tables 4.1 and 4.2. The wrinkle numbers predicted by ABAQUS simulations are in good agreement with theoretical predictions, LAMMPS simulations, and eigenvalue analysis.

Table 4.1 Lamé setup parameters and simulated wrinkle number for the results in Figure 4.7

r_i	r_o	B	S	γ_i	γ_o	ρg	Simulated wrinkle number m		
							Eigenvalue analysis	ABAQUS simulation	LAMMPS simulation
50	500	0.4	1000	2.84	1	0.1	41	40	41
50	500	0.4	1000	2.56	1	0.01	27	27	28
50	500	0.4	1000	2.5	1	0.001	22	24	24
50	500	0.4	1000	2.5	1	0.0001	22	23	22

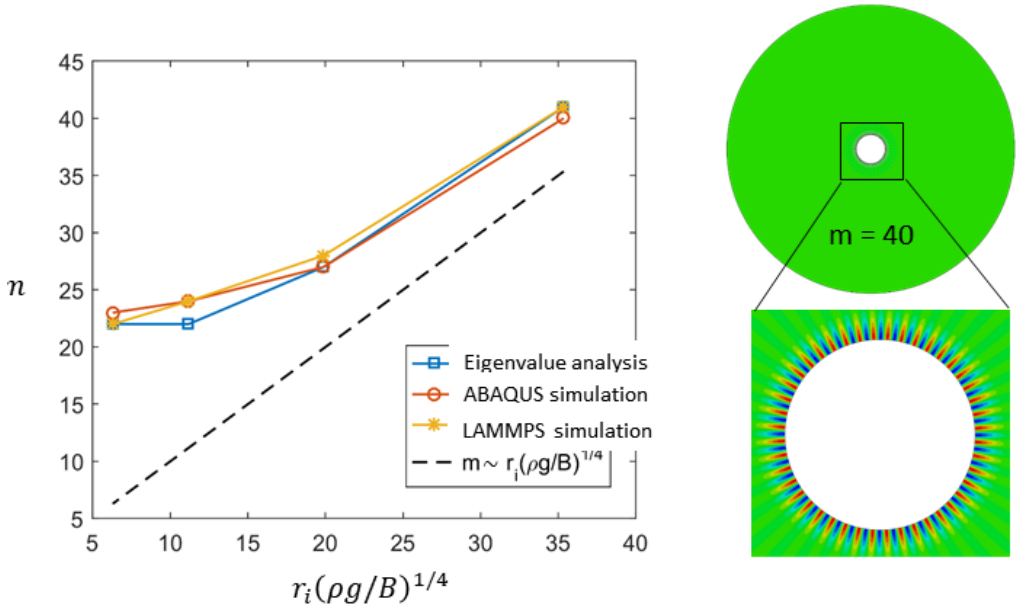

Figure 4.7 Validation of the finite element model by testing the scaling law $m \sim \epsilon^{-1/4}$

r_i	r_o	B	S	γ_i	γ_o	ρg	Simulated wrinkle number m (ABAQUS)
100	600	0.0125	923.761	1	0.25	0	37
100	600	0.05	923.761	1	0.25	0	29
50	300	0.05	923.761	1	0.25	0	20
50	300	0.2	923.761	1	0.25	0	14
50	300	0.8	923.761	1	0.25	0	11

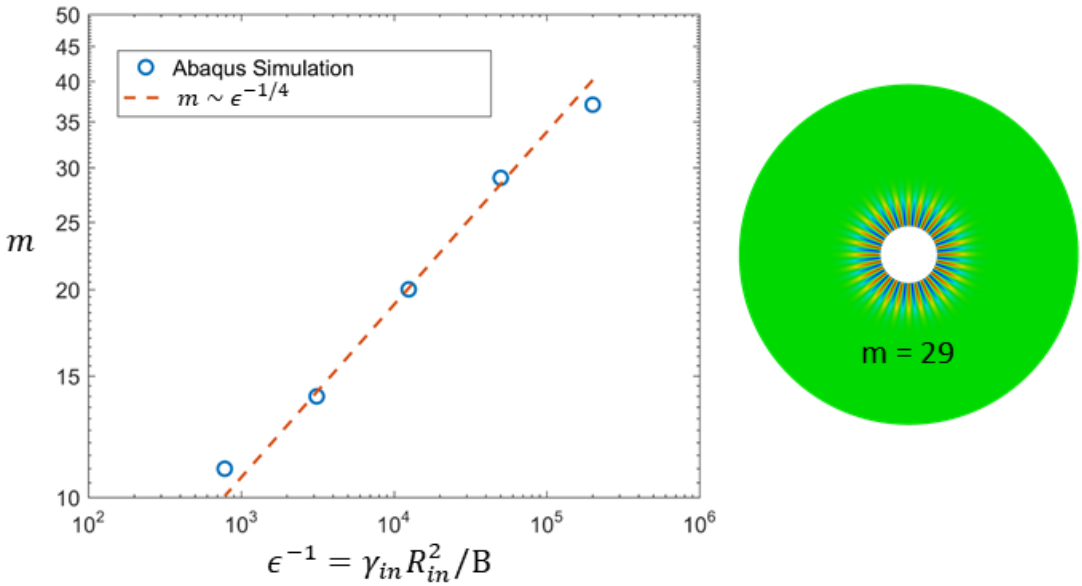

Figure 4.8 Validation of the finite element model by testing the scaling law $m \sim r_i(\rho g/B)^{1/4}$

4.4.2.3 Initial perturbation sensitivity tests

Figure 4.9 compares the effect of two different types of initial perturbations – spatially uniform and spatially random initial pressures acting on the annular sheets – on the fully relaxed wrinkle patterns. We can observe that there is no significant difference in the macroscopic wrinkle patterns for the four Lamé setup cases we have tested.

Table 4.3 Lamé setup parameters for the results in Figure 4.9

ID	r_i	r_o	γ_i	γ_o	t	E	ν	ρg	ϵ^{-1}	τ	B_o
4EHJBD	50	500	4	1	0.0752768	800	0.3	0.08	320000.000	4	0.02
7ZBKYN	50	500	4	1	0.0948428	800	0.3	0.04	160000.000	4	0.04
DHPGRO	50	500	4	1	0.1085679	800	0.3	0.02667	106666.667	4	0.06
IH8VZW	50	500	4	1	0.1194944	800	0.3	0.02	80000.000	4	0.08

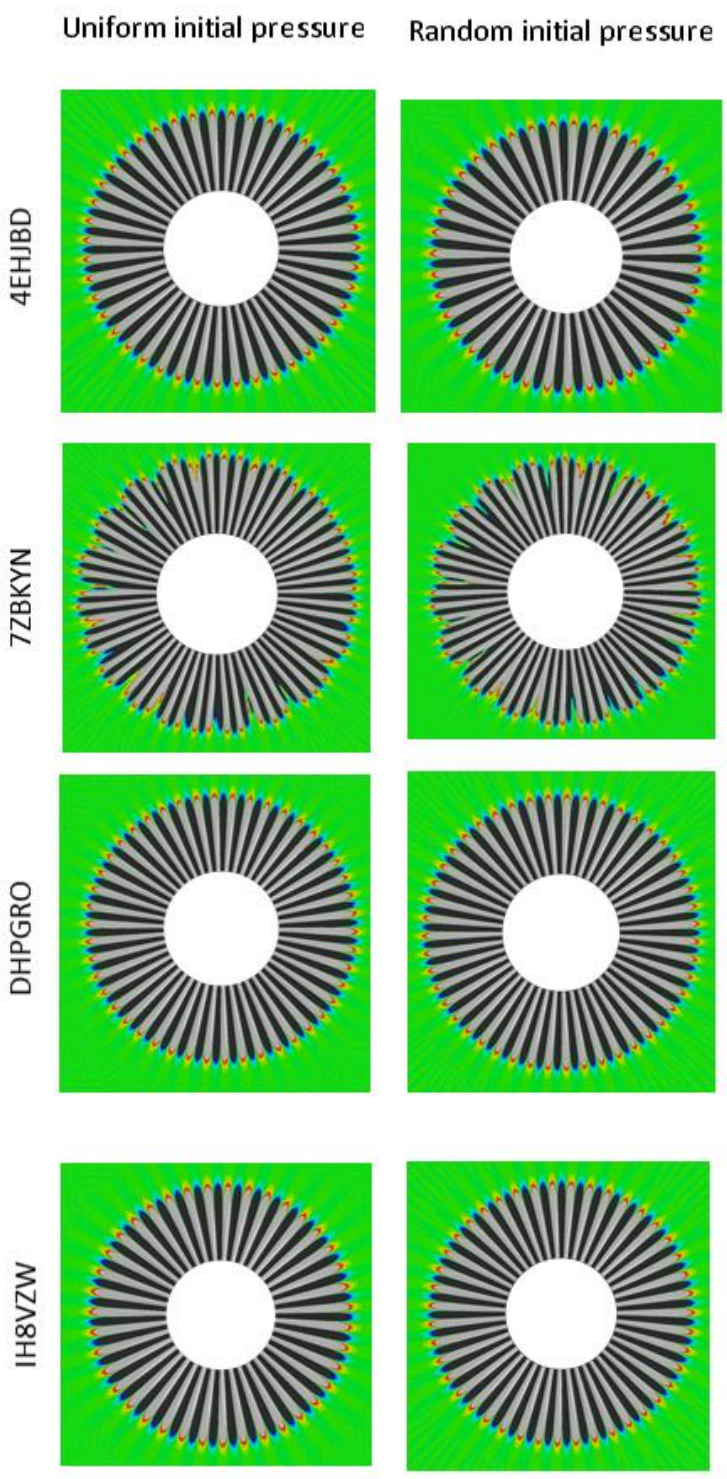

Figure 4.9 Comparison of the effects of two different types of initial perturbations – spatially uniform and spatially random initial pressures – on the fully relaxed wrinkle patterns.

4.4.3 Data analysis

The wrinkle number of each simulation is extracted from the out-of-plane deflection data using custom MATLAB code. The same routine is used to extract the wrinkle number from experiments after converting wrinkle images to intensity signal data using a custom automated image analysis following References [130,132].

We extract $l_{||}$ from the out-of-plane deflection data obtained from the simulations and the intensity signal data obtained from the experiments using FFT (Fast Fourier Transform) algorithm provided in MATLAB. Consider the simplest possible amplitude-modulated deflection (or signal) data curve at a given radius r corresponding to Equation (4.28), as illustrated schematically in Figure 4.5C:

$$\zeta(\theta) = \cos\left(\frac{2\pi r}{\lambda}\theta\right)\cos\left(\frac{\pi r}{l_{||}}\theta\right) \tag{4.34}$$

or equivalently

$$\zeta(\theta) = \frac{1}{2}\cos\left[2\pi\left(\frac{r}{\lambda}+\frac{r}{2l_{||}}\right)\theta\right] + \frac{1}{2}\cos\left[2\pi\left(\frac{r}{\lambda}-\frac{r}{2l_{||}}\right)\theta\right] \tag{4.35}$$

FFT analysis of this data curve gives a Fourier spectrum with two peaks corresponding to the frequencies

$$k_1 = \frac{r}{\lambda} - \frac{r}{2l_{||}} \tag{4.36}$$

$$k_2 = \frac{r}{\lambda} + \frac{r}{2l_{||}} \tag{4.37}$$

Reducing r in the Equations (4.36) and (4.37) gives the equation for extracting $l_{||}$ from the FFT analysis of simulation and experimental data:

$$\frac{l_{||}}{\lambda} = \frac{k_1 + k_2}{2(k_2 - k_1)} \tag{4.38}$$

Figures 4.10B-E show the deflection data curves and their Fourier spectrums obtained from two of our simulations. The spectrum in Figure 4.10C has two strong peaks at $k_1 = 55$ and $k_2 = 92$. Plugging them into Equation (4.38) yields $l_{||}/\lambda = 2.0$. However, from Figure 4.10E, it is difficult to distinguish two dominant peaks. In cases such as this, we obtain $l_{||}$ from direct inspection of the out-of-plane displacement maps (or experimental images) by identifying regions of strong, nearly-parallel wrinkles, an example of which is shown in Figure 4.10A.

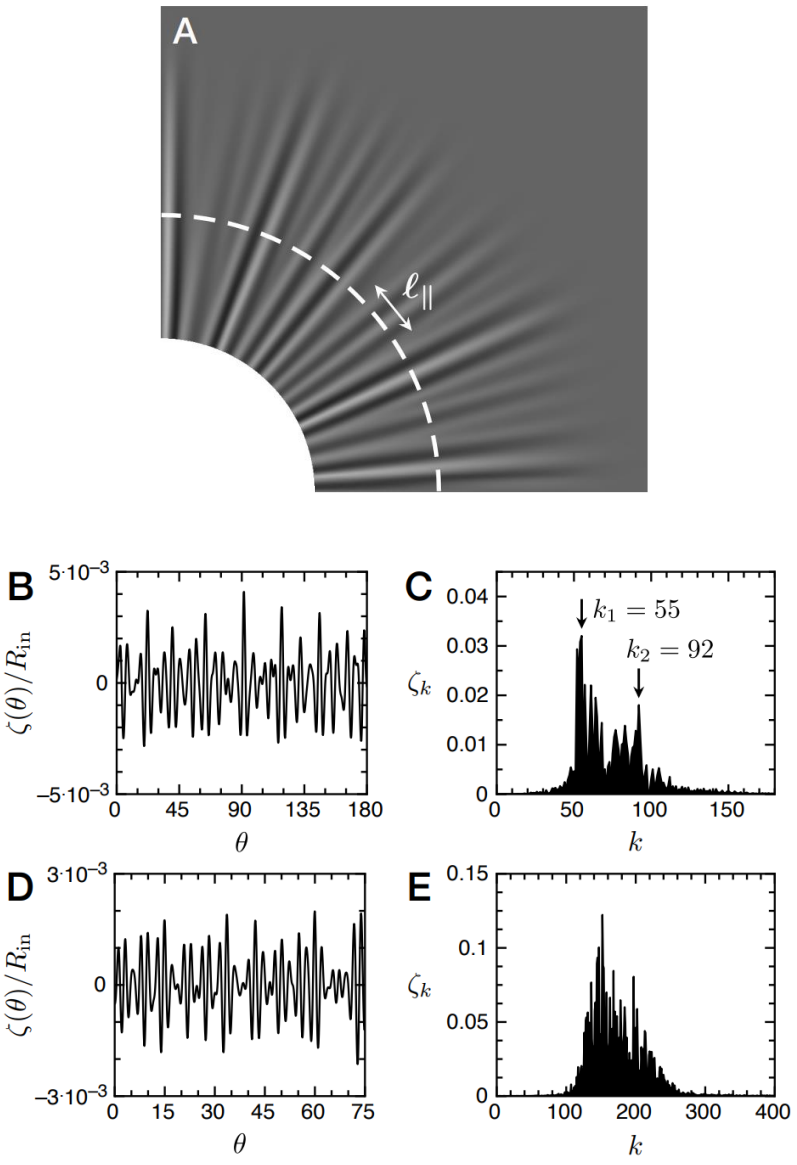

Figure 4.10 (A) Wrinkle pattern from simulations, showing strong amplitude modulation. (B)-(E) Deflection data curves and the corresponding Fourier spectrums from simulations with and without two dominant peaks. This figure is adapted from Reference [143].

4.5 Comparing simulation and experimental results with theory

4.5.1 Regime diagram

Simulations are performed for a wide range of values for three dimensionless parameters in the Lamé problem: $B_o \in (0.07, 333)$, $\tau \in (3.0, 8.7)$ and $\epsilon^{-1} \in (5 \times 10^4, 3 \times 10^7)$. Furthermore, in the large B_o regime, which is the primary focus of our study, we fix the ratio $\sqrt{B_o \cdot \epsilon} = 0.01$, to make sure the wrinkle pattern is well described by the tension field theory. The simulated annular sheet is made of an elastic material with large Young's modulus and Poisson's ratio $\nu = 0.3$ to ensure the tension is much smaller than the in-plane stiffness ($\gamma_{in}/Y < 0.01$). The complete set of parameters is listed in Table 4.4.

Figure 4.11 shows the wrinkle patterns observed in simulations and experiments for various values of B_o and τ. Two distinctive patterns can be identified: one with a spatially constant wrinkle number $m \approx m_0$ and nonconstant wavelength $\lambda(r) \approx 2\pi r/m_0$ (Figure 4.11 A, E, C, G); the other with a spatially constant wavelength $\lambda \approx \lambda_0$ and nonconstant wrinkle number $m(r) \approx 2\pi r/\lambda_0$ (Figure 4.11 B, F, D, H). The former patterns are simpler, free of defects and exhibit almost uniform wrinkle amplitude. In contrast, the later ones are more complex, proliferated with defects, and exhibit strong modulations of the wrinkle amplitude, such that defect-rich regions occur at amplitude-suppressed zones. We collect our observations in a regime diagram (Figure 4.11I) in which the defect-free and defect-rich regimes are separated by a transitional curve $B_o^c(\tau)$ scaling as

$$B_o^c(\tau) \sim (\tau - 2)^{-3.4 \pm 0.3} \tag{4.39}$$

Table 4.4 Lamé setup parameters for the results in Figure 4.9

r_i	r_o	γ_i	γ_o	t	E	ν	ρg	ϵ^{-1}	τ	B_o
50	500	3.1	1	0.0236	500	0.3	0.16533	12813333	3.1	0.0075
50	500	3.1	1	0.0298	500	0.3	0.08267	6406667	3.1	0.015
50	500	3.1	1	0.0375	500	0.3	0.04133	3203333	3.1	0.03
50	500	3.1	1	0.0473	500	0.3	0.02067	1601667	3.1	0.06
50	500	3.1	1	0.0596	500	0.3	0.01033	800833	3.1	0.12
50	500	3.1	1	0.0750	500	0.3	0.00517	400417	3.1	0.24
50	500	3.1	1	0.0946	500	0.3	0.00258	200208	3.1	0.48
50	500	3.1	1	0.1191	500	0.3	0.00129	100104	3.1	0.96
50	500	3.3	1	0.0215	500	0.3	0.22000	18150000	3.3	0.006
50	500	3.3	1	0.0271	500	0.3	0.11000	9075000	3.3	0.012
50	500	3.3	1	0.0341	500	0.3	0.05500	4537500	3.3	0.024
50	500	3.3	1	0.0430	500	0.3	0.02750	2268750	3.3	0.048
50	500	3.6	1	0.0312	500	0.3	0.07200	6480000	3.6	0.02
50	500	3.6	1	0.0393	500	0.3	0.03600	3240000	3.6	0.04
50	500	3.6	1	0.0495	500	0.3	0.01800	1620000	3.6	0.08
50	500	3.6	1	0.0624	500	0.3	0.00900	810000	3.6	0.16
50	500	3.8	1	0.0306	500	0.3	0.07600	7220000	3.8	0.02
50	500	3.8	1	0.0386	500	0.3	0.03800	3610000	3.8	0.04
50	500	3.8	1	0.0486	500	0.3	0.01900	1805000	3.8	0.08
50	500	3.8	1	0.0613	500	0.3	0.00950	902500	3.8	0.16
50	500	3.8	1	0.0772	500	0.3	0.00475	451250	3.8	0.32
50	500	3.8	1	0.0972	500	0.3	0.00238	225625	3.8	0.64
50	500	4.3	1	0.0354	500	0.3	0.04914	5282857	4.3	0.035
50	500	4.3	1	0.0446	500	0.3	0.02457	2641429	4.3	0.07

50	500	4.3	1	0.0562	500	0.3	0.01229	1320714	4.3	0.14
50	500	4.3	1	0.0708	500	0.3	0.00614	660357	4.3	0.28
50	500	4.3	1	0.0893	500	0.3	0.00307	330179	4.3	0.56
50	500	4.7	1	0.0285	500	0.3	0.09400	11045000	4.7	0.02
50	500	4.7	1	0.0360	500	0.3	0.04700	5522500	4.7	0.04
50	500	4.7	1	0.0453	500	0.3	0.02350	2761250	4.7	0.08
50	500	4.7	1	0.0571	500	0.3	0.01175	1380625	4.7	0.16
50	500	4.7	1	0.0719	500	0.3	0.00588	690313	4.7	0.32
50	500	4.7	1	0.0906	500	0.3	0.00294	345156	4.7	0.64
50	500	4.7	1	0.1141	500	0.3	0.00147	172578	4.7	1.28
50	500	5.7	1	0.0425	500	0.3	0.02850	4061250	5.7	0.08
50	500	5.7	1	0.0535	500	0.3	0.01425	2030625	5.7	0.16
50	500	5.7	1	0.0674	500	0.3	0.00713	1015313	5.7	0.32
50	500	5.7	1	0.0850	500	0.3	0.00356	507656	5.7	0.64
50	500	5.7	1	0.1070	500	0.3	0.00178	253828	5.7	1.28
50	500	5.7	1	0.1349	500	0.3	0.00089	126914	5.7	2.56
50	500	7.3	1	0.0310	500	0.3	0.07300	13322500	7.3	0.04
50	500	7.3	1	0.0391	500	0.3	0.03650	6661250	7.3	0.08
50	500	7.3	1	0.0493	500	0.3	0.01825	3330625	7.3	0.16
50	500	7.3	1	0.0621	500	0.3	0.00913	1665313	7.3	0.32
50	500	8.7	1	0.0811	500	0.3	0.00409	890471	8.7	0.85
50	500	8.7	1	0.1022	500	0.3	0.00205	445235	8.7	1.7
50	500	8.7	1	0.1287	500	0.3	0.00102	222618	8.7	3.4
50	500	8.7	1	0.1622	500	0.3	0.00051	111309	8.7	6.8

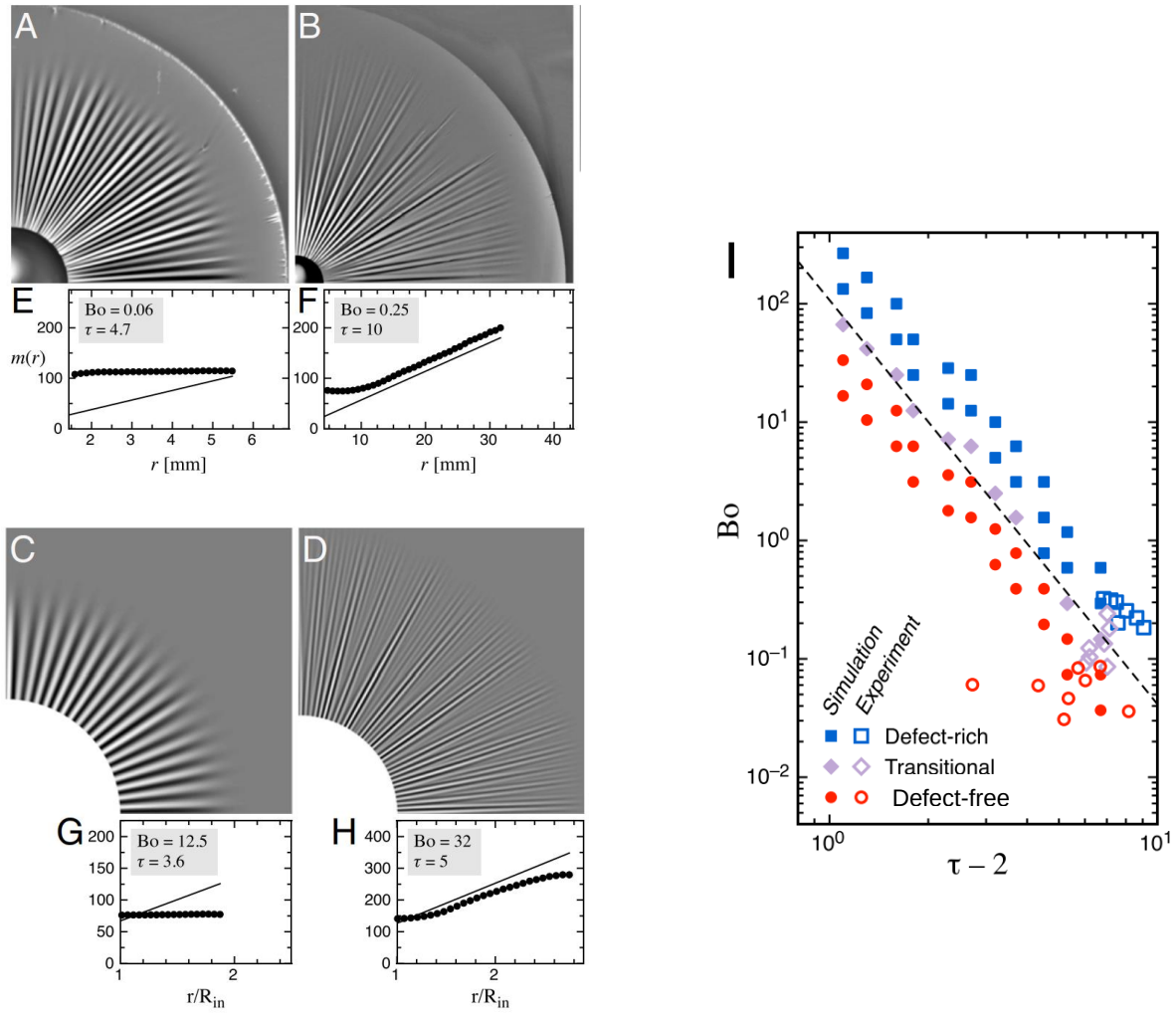

Figure 4.11 Characteristic wrinkle patterns observed in experiments and simulations for various values of B_o and τ. (A-D) Representative wrinkle patterns in the defect-free (left two) and defect-rich (right two) regimes observed in experiments (upper two) and simulations (lower two). (E-H) Wrinkle number m versus radial coordinate r for the images above them. Solid lines: theoretical prediction of wrinkle number by Equation (4.26). (I) A regime diagram, spanned by the parameters B_o and τ, is divided into two regimes where wrinkle patterns are proliferated with defects and free of defects. This figure is adapted from Reference [143].

4.5.1 Length scale of wrinkle amplitude

Figures 4.12 A and C show the azimuthal profile of the out-of-plane deflection at a single radius, extracted from experiments and simulations. Large modulations of wrinkle amplitude are clearly present. Figures 4.12 B and D show the measured $l_{\|}/\bar{\lambda}$ at several radii compared to the theoretical predictions. Figure 4.12E compares the measured and predicted values of $l_{\|}/\bar{\lambda}$ for several sheets with varied values of B_o and τ. No fitting parameters are used. The experiments exhibit good agreement with the theory, whereas simulation results are systematically lower than expected and approach the predicted values only at large B_o and small τ. We attribute this discrepancy to the numerical difficulty in reaching the most low-lying energy states and the apparent abundance of metastable states where defects are scattered randomly throughout the film, rather than gathering in a smaller number of defect-rich zones, which tends to increase $l_{\|}$ towards the predicted value.

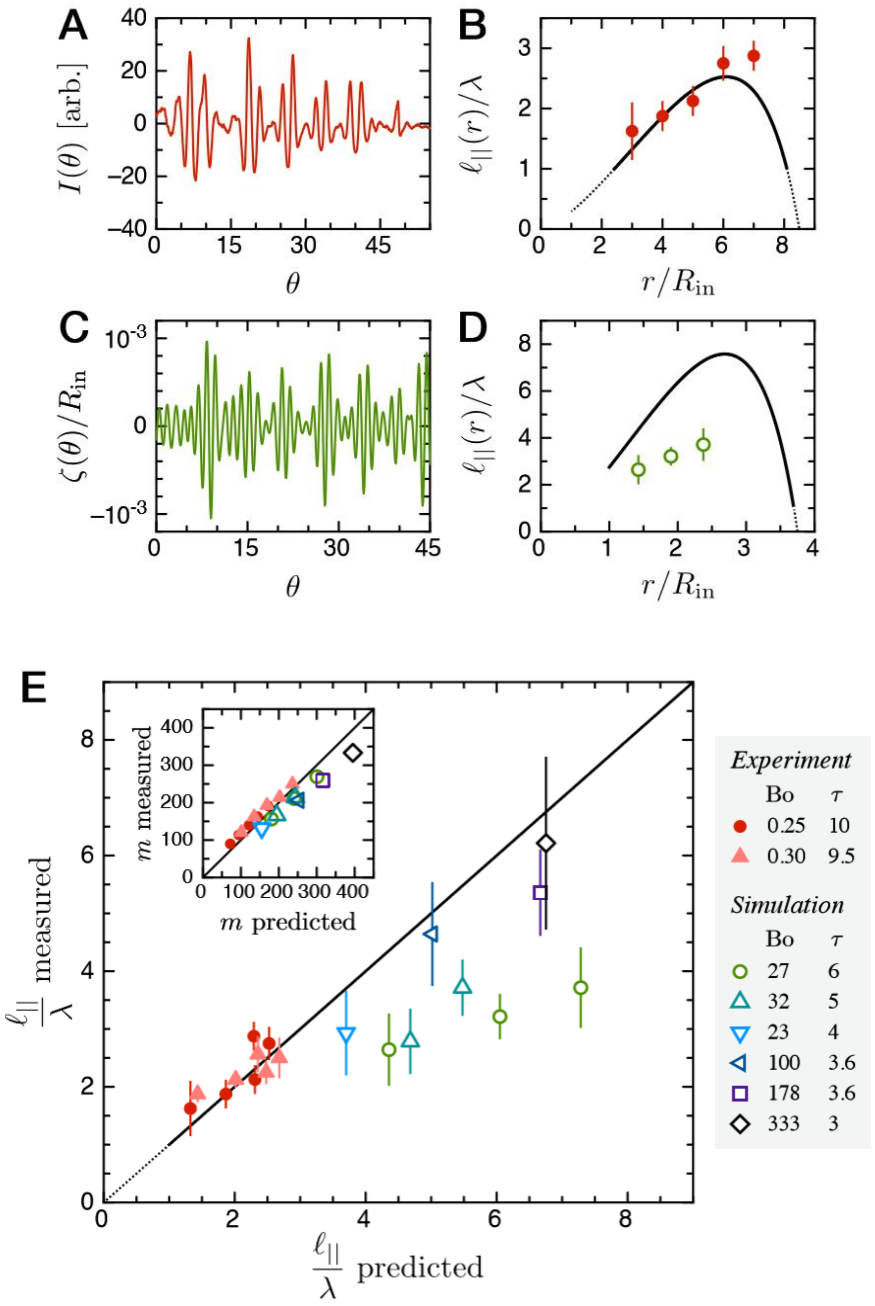

Figure 4.12 Amplitude modulations and their lateral length scale $l_{\|}$ (normalized by the wavelength λ). (A) Image intensity profile $I(\theta)$ at radius r = 26 mm from an experiment with B_o = 0.25 and τ = 10. (B) Radial dependence of $l_{\|}/\lambda$ measured in the experiment in panel A (circles), compared with the theoretical prediction (solid line) by Equation (4.32). (C) Out-of-plane deflec-

tion profile $\zeta(\theta)$ at radius r/R_{in} = 2.4 in a simulation with B_o= 27 and τ = 6. (D) Radial dependence of $l_{\|}/\lambda$ extracted from the simulation in panel C (circles), compared with the theoretical prediction (solid line) by Equation (4.32). (E) Main: Measured $l_{\|}/\lambda$ versus the predicted value. Inset: The measured wrinkle number compared with its theoretical prediction (solid line) by Equation (4.26). Data are sampled at the same radii as the main panel. This figure is adapted from Reference [143].

4.6 Summary

In this work, we studied the Lamé setup, an annular sheet attached to a liquid substrate subjected to tensile loads on its edges, as a prototypical model for more general wrinkling phenomena characterized by a uniform wavelength and radial wrinkle directions. Our theoretical, simulation and experimental results show that the wrinkle patterns of the Lamé setup may either consist of a fixed number of wrinkles absent of defects, or be characterized by a uniform wavelength $\bar{\lambda}$ with modulated amplitude (over a length scale $l_{\|}$) that enables the proliferation of defect-rich zones. The combined effect of defects and amplitude modulations suggests an analogy between thin elastic systems and defect-proliferated phases of liquid crystals and superconductors, allowing us to make predictions about the emerging patterns observed in them.

While our work addresses only wrinkle problems with a uniform wavelength and radial wrinkle directions, we anticipate that the theoretical, numerical, and experimental approaches developed here may provide a unified framework to predict multiscale patterns in a broad class of wrinkle problems in thin sheets [124].

Chapter 5: Conclusion and Future Works

5.1 Conclusion

In summary, we modeled and simulated the wrinkling of annular sheets and the buckling of cylindrical shells by using finite element methods and discrete shell models integrated with energy minimization and pathfinding algorithms. The results of these two prototypical problems reveal complex post-buckling morphologies, and our methods provide unified frameworks for studying morphological instabilities in thin solids. The results of each chapter are summarized as follows.

In Chapter 2, our tests showed that among the three discrete shell models (hinge model, triangle averaged model, and quadratic fit model), only the quadratic fit model exhibited mesh-independent behaviors, although all models are convergent on an equilateral triangular mesh. For annular wrinkling problems (e.g. Lamé problem) in which there exist a large number of neighboring stable states, dynamic relaxation simulations of the discrete shell model will be highly sensitive to different meshes or initial perturbations.

In Chapter 3, we integrated a discrete shell model with energy minimization and pathfinding algorithms, to survey the stable states and the transition paths between them for the buckling of spherical cap and cylindrical shells. For spherical cap buckling, two qualitatively different regimes were observed: a bistable regime in which the shell remains in the inverted state after the removal of the indenter and a monostable regime in which the shell returns to the natural state after the removal of the indenter. We found that whether the shell is in the monostable or bistable regime depends on a single parameter λ_d. For cylindrical shell buckling, we found that the global energy minima are either unbuckled states or multiply dimpled states and that the transition

states are always singly dimpled states. We then illustrated the buckling energy landscapes as disconnectivity graphs and showed that the landscapes for long cylinders are complex and glassy, featuring a large number of clustering local energy minima. For cylinders under large compressive strains, their landscapes feature many low-energy stable states. Finally, we demonstrated how the buckling energy landscapes enable us to significantly increase the buckling resistance or stabilize a post-buckling state of a cylindrical shell with almost no increase in its overall weight.

In Chapter 4, we addressed the wrinkle phenomena characterized by a uniform wavelength and radial wrinkle directions, through analyzing the wrinkle pattern of an annular sheet attached to a liquid substrate subjected to tensile loads on its edges, also known as the Lamé setup. Our theoretical, simulation and experimental results show that such phenomena may either consist of a fixed number of wrinkles with varying wavelengths or a uniform wavelength with a modulated amplitude that enables the proliferation of defect-rich zones.

5.2 Future works

Here we present our preliminary results and future work for the simulations of 3D reconfigurable structures, which is based on the collaborative work with Prof. Halim Kusumaatmaja's group at Durham University, UK and Prof. Xueju Wang's group at the University of Connecticut.

Reconfigurable 3D structures whose geometries can be actively and reversibly altered between different configurations are important upon external stimuli (e.g. mechanical forces, magnetic fields, hydration, and temperature) [144-147] in a wide range of engineering applications, including deployable solar panels [148], electromagnetic metamaterials [149,150], phononics [151-153], biomedical devices [154,155], emerging soft robotics [156-158], metasurfaces [159-

161], and many others. Reconfigurability based on the multistability of structures can potentially realize shape changes without the requirement of persistent external stimuli [20-23]. Despite intensive studies and great progress, there is still a lack of fundamental understanding of the principles that control and tailor the multistable states.

Here we will search for a set of strategies and design concepts to address this issue. Our approach relies on 3D structures assembled from ferromagnetic composite films which can be remotely and rapidly deformed into multiple distinct states under external magnetic forces and maintain those deformed shapes even after the magnetic field is removed, as illustrated in Figure 5.1A. We explore the energy landscapes of the 3D structures using the minimization and path-finding algorithms and the discrete shell model mentioned in Chapter 3, to systematically identify their multistable states and the energy-efficient reconfiguration path.

Figures 5.1B-E present our simulation predictions for two 3D structures reconfigured into distinct stable configurations using a portable disk magnet, with the color in the figures denoting the displacement along z-direction in the structure. The peak strain values in all stable states remain within the elastic range of the ferromagnetic composite, which ensures structural integrity and allows repeated reversible deformation processes without damage to the constituent material. Our simulations will be compared with experimental results for the same 3D structures for verification.

Our future works include identifying the minimum energy paths between these stable configurations and their energy barriers, and maximizing the energy well depth of targeted configurations, and eliminating small and unfavorable local minima in the design of reconfigurable structures.

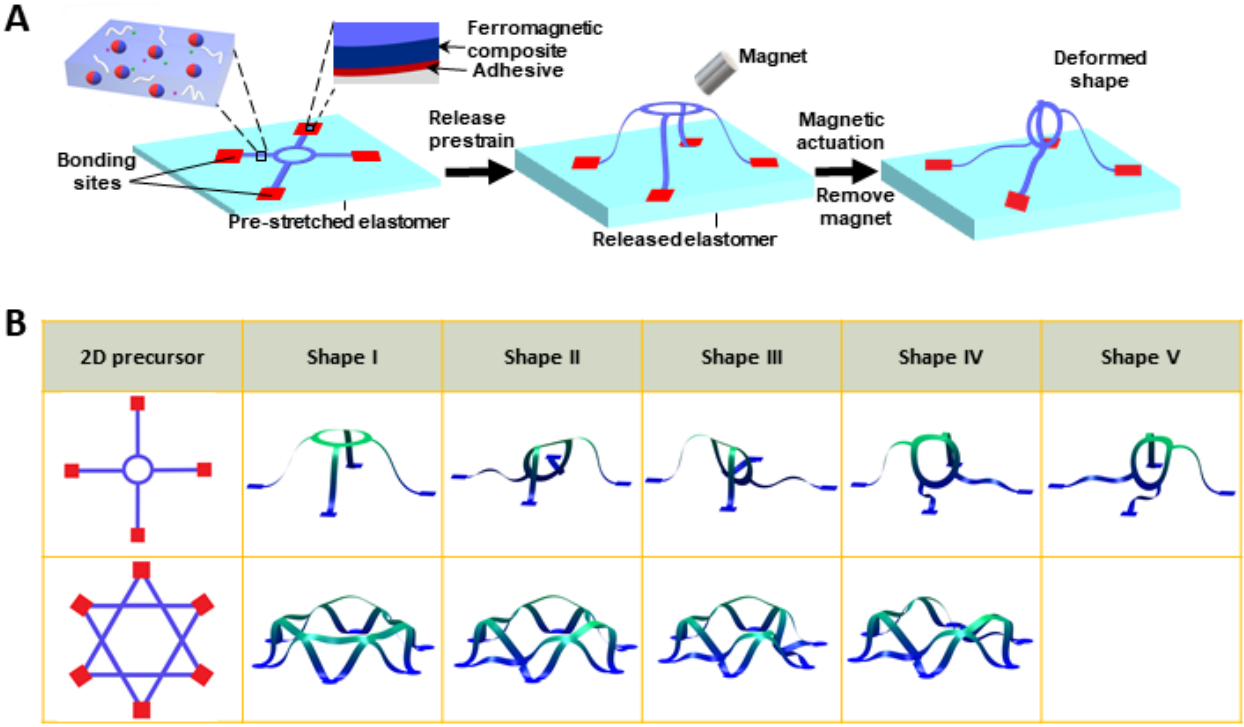

Figure 5.1 Magnetically reconfigurable 3D structures. (A) Schematic illustration of the assembly and reconfiguration of ferromagnetic 3D structures (courtesy of Prof. Xueju Wang). (B) Simulation predictions for multistable states of two 3D structures.

Appendix A: Force Calculation of Discrete Thin Shell Models

A.1 Membrane force

Let $\mathbf{F}_{mi}$ be the membrane force vector acting on vertex i. Taking gradient of the discrete membrane energy in Section 2.3.1 with respect to coordinate vector $\mathbf{x}_i$ of vertex i we have

$$\begin{aligned}\mathbf{F}_{m1} &= \frac{\partial E_m}{\partial \mathbf{x}_1} = -A\frac{\partial U_m}{\partial \mathbf{x}_1} = -A\left(\frac{\partial U_m}{\partial s_2}\frac{\partial s_2}{\partial \mathbf{x}_1} + \frac{\partial U_m}{\partial s_3}\frac{\partial s_3}{\partial \mathbf{x}_1}\right) \\ &= -2A\left(a_{2p}s_p\mathbf{v}_{13} - a_{3p}s_p\mathbf{v}_{21}\right)\end{aligned} \tag{A.1}$$

$$\begin{aligned}\mathbf{F}_{m2} &= \frac{\partial E_m}{\partial \mathbf{x}_2} = -A\frac{\partial U_m}{\partial \mathbf{x}_2} = -A\left(\frac{\partial U_m}{\partial s_1}\frac{\partial s_1}{\partial \mathbf{x}_2} + \frac{\partial U_m}{\partial s_3}\frac{\partial s_3}{\partial \mathbf{x}_2}\right) \\ &= -2A\left(a_{1p}s_p\mathbf{v}_{32} - a_{3p}s_p\mathbf{v}_{21}\right)\end{aligned} \tag{A.2}$$

$$\begin{aligned}\mathbf{F}_{m3} &= \frac{\partial E_m}{\partial \mathbf{x}_3} = -A\frac{\partial U_m}{\partial \mathbf{x}_3} = -A\left(\frac{\partial U_m}{\partial s_1}\frac{\partial s_2}{\partial \mathbf{x}_3} + \frac{\partial U_m}{\partial s_2}\frac{\partial s_3}{\partial \mathbf{x}_3}\right) \\ &= -2A\left(a_{1p}s_p\mathbf{v}_{32} - a_{2p}s_p\mathbf{v}_{13}\right)\end{aligned} \tag{A.3}$$

A.2 Bending force (hinge model)

The bending force $\mathbf{F}_{bi}$ acting on vertex i corresponding to the discrete bending energy in Section 2.3.2 is

$$\mathbf{F}_{bi} = -\frac{\partial E_b}{\partial \mathbf{x}_i} = -k[1 + \sin(\theta - \bar{\theta})]\frac{\partial \theta}{\partial \mathbf{x}_i} \tag{A.4}$$

where

$$\frac{\partial \theta}{\partial \mathbf{x}_1} = -\|\mathbf{v}_{32}\|\frac{\mathbf{v}_{21} \times \mathbf{v}_{32}}{\|\mathbf{v}_{21} \times \mathbf{v}_{32}\|^2} \tag{A.5}$$

$$\frac{\partial \theta}{\partial \mathbf{x}_4} = \|\mathbf{v}_{32}\| \frac{\mathbf{v}_{34} \times \mathbf{v}_{23}}{\|\mathbf{v}_{34} \times \mathbf{v}_{23}\|^2} \tag{A.6}$$

$$\frac{\partial \theta}{\partial \mathbf{x}_2} = \left(\frac{\mathbf{v}_{12} \cdot \mathbf{v}_{32}}{\|\mathbf{v}_{32}\|^2} - 1\right) \frac{\partial \theta}{\partial \mathbf{x}_1} - \frac{\mathbf{v}_{34} \cdot \mathbf{v}_{32}}{\|\mathbf{v}_{32}\|^2} \frac{\partial \theta}{\partial \mathbf{x}_4} \tag{A.7}$$

$$\frac{\partial \theta}{\partial \mathbf{x}_3} = \left(\frac{\mathbf{v}_{34} \cdot \mathbf{v}_{32}}{\|\mathbf{v}_{32}\|^2} - 1\right) \frac{\partial \theta}{\partial \mathbf{x}_4} - \frac{\mathbf{v}_{12} \cdot \mathbf{v}_{32}}{\|\mathbf{v}_{32}\|^2} \frac{\partial \theta}{\partial \mathbf{x}_1} \tag{A.8}$$

A.3 Bending force (triangle-averaged model)

The bending force $\mathbf{F}_{bk}$ acting on vertex i corresponding to the discrete bending energy in Section 2.3.3 is

$$\mathbf{F}_{bk} = -\frac{\partial E_b}{\partial \mathbf{x}_k} = \frac{1}{2A}\left[\alpha[(\theta_i - \bar{\theta}_i)L_i]\left(\frac{\partial \theta_i}{\partial \mathbf{x}_k} L_i\right) + \beta \frac{\partial \theta_i}{\partial \mathbf{x}_k} \theta_j \frac{T_{ij}^2}{L_i L_j}\right] \tag{A.9}$$

where $\frac{\partial \theta_i}{\partial \mathbf{x}_k}$ are given by Equations (A.5) ~ (A.8).

A.4 Bending force (quadratic fit model)

The bending force $\mathbf{F}_{bk}$ acting on vertex k corresponding to the discrete bending energy in Section 2.3.4 is

$$\mathbf{F}_{bk} = -\frac{\partial E_b}{\partial \mathbf{x}_k} = -\frac{\partial E_b}{\partial a_i} \frac{\partial a_i}{\partial \theta_j} \frac{\partial \theta_j}{\partial \mathbf{x}_k} \tag{A.10}$$

where

$$\frac{\partial E_b}{\partial a_4} = 8\alpha(a_4 - A_4 + a_6 - A_6) + 8\beta(a_4 - A_4) \tag{A.11}$$

$$\frac{\partial E_b}{\partial a_5} = 4\beta(a_5 - A_5) \tag{A.12}$$

$$\frac{\partial E_b}{\partial a_6} = 8\alpha(a_4 - A_4 + a_6 - A_6) + 8\beta(a_6 - A_6) \tag{A.13}$$

$$\frac{\partial a_i}{\partial \theta_j} = C_{ij} D_j \tag{A.14}$$

and $\frac{\partial \theta_j}{\partial \mathbf{x}_k}$ are given by Equations (A.5) ~ (A.8).

Appendix B: Fortran Subroutines for Discrete Thin Shell Models

```
! ================================================================================

   module dsm

 ! Calculate the energy, gradient and hessian of the discrete thin shell model
 !
    implicit none
    double precision, allocatable, private :: bondlist(:,:), ks(:), r0(:), &
                                              dihedrallist(:,:), kb(:), phi0(:)
    integer, private :: nbondlist, nbondtype, ndihedrallist, ndihedraltype, ndof

  contains

    ! --------------------------------------------------------------------------------

    subroutine init(blist, dlist, S, r0_, B, phi0_, nnode)

    ! Module initialization
    !
    ! Input parameters
    ! blist(i,j)    Bond list
    !               blist(i,1) First node of the ith bond
    !               blist(i,2) Second node of the ith bond
    !               blist(i,3) Bond Type of the ith bond
    ! dlist(i,j)    Dihedral list
    !               dlist(i,1) First node of the ith dihedral
    !               dlist(i,2) Second node of the ith dihedral
    !               dlist(i,3) Third node of the ith dihedral
    !               dlist(i,4) Fourth node of the ith dihedral
    !               dlist(i,5) Dihedral type of the ith dihedral
    ! S             Model parameter
    ! r0_             "
    ! B               "
    ! phi0_           "
    ! nnode         Number of nodes

      implicit none
      double precision, intent(in) :: S(:), r0_(:), B(:), phi0_(:)
      integer, intent(in) :: blist(:,:), dlist(:,:), nnode
      nbondlist = size(blist, 1)
      nbondtype = size(r0_)
      ndihedrallist = size(dlist, 1)
      ndihedraltype = size(phi0_)
      allocate(bondlist(nbondlist,3), ks(nbondtype), r0(nbondtype))
      allocate(dihedrallist(ndihedrallist,5), kb(ndihedraltype), phi0(ndihedraltype))
      bondlist = blist
      ks = S * (sqrt(3d0)/4d0)
      r0 = r0_
      dihedrallist = dlist
      kb = B * (2d0/sqrt(3d0))
      phi0 = phi0_
      ndof = 3*nnode
```

```
end subroutine init

! ------------------------------------------------------------------------------

subroutine compev(x,e,v)

! Compute energy and gradient
!
! Input parameters
! x(i)      Nodal coordinates
!           x(3*i-2) First coordinate of the ith node
!           x(3*i-1) Second coordinate of the ith node
!           x(3*i) Third coordinate of the ith node
! Ouput parameters
! e         Energy
! v(i)      Gradient de/dxi

  implicit none
  double precision, intent(in) :: x(ndof)
  double precision, intent(out) :: e, v(ndof)
  integer :: n, i1, i2, i3, i4, bondtype, dihedraltype, m, i
  double precision :: delx, dely, delz, rsq, r, dr, rk, fbond, &
                      vb1x, vb1y, vb1z, vb2x, vb2y, vb2z, vb2xm, vb2ym, vb2zm, vb3x, &
                      vb3y, vb3z, ax, ay, az, bx, by, bz, rasq, rbsq, rgsq, rg, &
                      rginv, ra2inv, rb2inv, rabinv, c, s, p, ddf1, df1, sin_shift, &
                      cos_shift, fg, hg, fga, hgb, gaa, gbb, dtfx, dtfy, dtfz, dtgx, &
                      dtgy, dtgz, dthx, dthy, dthz, df, sx2, sy2, sz2, f1x, f1y, f1z, &
                      f2x, f2y, f2z, f3x, f3y, f3z, f4x, f4y, f4z
  e = 0d0
  v = 0d0

  ! Stretching energy and gradient
  do n = 1,nbondlist
    i1 = bondlist(n,1)
    i2 = bondlist(n,2)
    bondtype = bondlist(n,3)
    delx = x(3*i1-2) - x(3*i2-2)
    dely = x(3*i1-1) - x(3*i2-1)
    delz = x(3*i1) - x(3*i2)
    rsq = delx*delx + dely*dely + delz*delz
    r = sqrt(rsq)
    dr = r - r0(bondtype)
    rk = ks(bondtype) * dr
    if (r > 0d0) then
        fbond = -2d0*rk/r
    else
        fbond = 0d0
    endif
    e = e + rk*dr
    v(3*i1-2) = v(3*i1-2) - delx*fbond
    v(3*i1-1) = v(3*i1-1) - dely*fbond
    v(3*i1) = v(3*i1) - delz*fbond
    v(3*i2-2) = v(3*i2-2) + delx*fbond
    v(3*i2-1) = v(3*i2-1) + dely*fbond
    v(3*i2) = v(3*i2) + delz*fbond
  enddo

  ! Bending energy and gradient
  do n = 1,ndihedrallist
    i1 = dihedrallist(n,1)
```

```
i2 = dihedrallist(n,2)
i3 = dihedrallist(n,3)
i4 = dihedrallist(n,4)
dihedraltype = dihedrallist(n,5)
vb1x = x(3*i1-2) - x(3*i2-2)
vb1y = x(3*i1-1) - x(3*i2-1)
vb1z = x(3*i1) - x(3*i2)
vb2x = x(3*i3-2) - x(3*i2-2)
vb2y = x(3*i3-1) - x(3*i2-1)
vb2z = x(3*i3) - x(3*i2);
vb2xm = -vb2x
vb2ym = -vb2y
vb2zm = -vb2z
vb3x = x(3*i4-2) - x(3*i3-2)
vb3y = x(3*i4-1) - x(3*i3-1)
vb3z = x(3*i4) - x(3*i3)
ax = vb1y*vb2zm - vb1z*vb2ym
ay = vb1z*vb2xm - vb1x*vb2zm
az = vb1x*vb2ym - vb1y*vb2xm
bx = vb3y*vb2zm - vb3z*vb2ym
by = vb3z*vb2xm - vb3x*vb2zm
bz = vb3x*vb2ym - vb3y*vb2xm
rasq = ax*ax + ay*ay + az*az
rbsq = bx*bx + by*by + bz*bz
rgsq = vb2xm*vb2xm + vb2ym*vb2ym + vb2zm*vb2zm
rg = sqrt(rgsq)
rginv = 0d0
ra2inv = 0d0
rb2inv = 0d0
if (rg > 0d0) then
    rginv = 1d0/rg
endif
if (rasq > 0d0) then
    ra2inv = 1d0/rasq
endif
if (rbsq > 0d0) then
    rb2inv = 1d0/rbsq
endif
rabinv = sqrt(ra2inv*rb2inv)
c = (ax*bx + ay*by + az*bz)*rabinv
s = rg*rabinv*(ax*vb3x + ay*vb3y + az*vb3z)
if (c > 1d0) then
    c = 1d0
endif
if (c < -1d0) then
    c = -1d0
endif
p = 1d0
ddf1 = 0d0
df1 = 0d0
ddf1 = p*c - df1*s
df1 = p*s + df1*c
p = ddf1
cos_shift = cos(phi0(dihedraltype))
sin_shift = sin(phi0(dihedraltype))
p = p*cos_shift + df1*sin_shift
df1 = df1*cos_shift - ddf1*sin_shift
df1 = -1d0 * df1
p = p + 1d0
fg = vb1x*vb2xm + vb1y*vb2ym + vb1z*vb2zm
hg = vb3x*vb2xm + vb3y*vb2ym + vb3z*vb2zm
```

```
    fga = fg*ra2inv*rginv
    hgb = hg*rb2inv*rginv
    gaa = -ra2inv*rg
    gbb = rb2inv*rg
    dtfx = gaa*ax
    dtfy = gaa*ay
    dtfz = gaa*az
    dtgx = fga*ax - hgb*bx
    dtgy = fga*ay - hgb*by
    dtgz = fga*az - hgb*bz
    dthx = gbb*bx
    dthy = gbb*by
    dthz = gbb*bz
    e = e + kb(dihedraltype) * p
    df = -kb(dihedraltype) * df1
    sx2 = df*dtgx
    sy2 = df*dtgy
    sz2 = df*dtgz
    f1x = df*dtfx
    f1y = df*dtfy
    f1z = df*dtfz
    f2x = sx2 - f1x
    f2y = sy2 - f1y
    f2z = sz2 - f1z
    f4x = df*dthx
    f4y = df*dthy
    f4z = df*dthz
    f3x = -sx2 - f4x
    f3y = -sy2 - f4y
    f3z = -sz2 - f4z
    v(3*i1-2) = v(3*i1-2) - f1x
    v(3*i1-1) = v(3*i1-1) - f1y
    v(3*i1) = v(3*i1) - f1z
    v(3*i2-2) = v(3*i2-2) - f2x
    v(3*i2-1) = v(3*i2-1) - f2y
    v(3*i2) = v(3*i2) - f2z
    v(3*i3-2) = v(3*i3-2) - f3x
    v(3*i3-1) = v(3*i3-1) - f3y
    v(3*i3) = v(3*i3) - f3z
    v(3*i4-2) = v(3*i4-2) - f4x
    v(3*i4-1) = v(3*i4-1) - f4y
    v(3*i4) = v(3*i4) - f4z
  enddo

end subroutine compev

! ------------------------------------------------------------------------------

subroutine comph(x,h)

! Compute hessian
!
! Input parameters
! x(i)      Nodal coordinates
!           x(3*i-2) First coordinate (x) of the ith node
!           x(3*i-1) Second coordinate (y) of the ith node
!           x(3*i) Third coordinate (z) of the ith node
! Ouput parameters
! h(i,j)    Hessian de2/dxidxj

  use hdn
```

```
implicit none
double precision, intent(in) :: x(ndof)
double precision, intent(out) :: h(ndof,ndof)
integer :: n, i1, i2, i3, i4, i, j, bondtype, dihedraltype, idx6(6), idx12(12), k
type(hyperdual) :: x6(6), x12(12), x6mod(6), x12mod(12), e, delx, dely, delz, rsq, &
                   r, r0hdn, dr, kshdn, rk, vb1x, vb1y, vb1z, vb2x, vb2y, vb2z, &
                   vb2xm, vb2ym, vb2zm, vb3x, vb3y, vb3z, ax, ay, az, bx, by, bz, &
                   rasq, rbsq, rgsq, rg, rginv, ra2inv, rb2inv, rabinv, c, s, p, &
                   ddf1, df1, sin_shift, cos_shift, fg, hg, fga, hgb, gaa, gbb, &
                   dtfx, dtfy, dtfz, dtgx, dtgy, dtgz, dthx, dthy, dthz, kbhdn
double precision :: h6(6,6), h12(12,12)
type(hyperdual), parameter :: zero=hyperdual(0d0,0d0,0d0,0d0), &
                              one=hyperdual(1d0,0d0,0d0,0d0)
h = 0d0

! Hessian of stretching energy
do n = 1,nbondlist
  i1 = bondlist(n,1)
  i2 = bondlist(n,2)
  bondtype = bondlist(n,3)
  idx6 = [3*i1-2, 3*i1-1, 3*i1, 3*i2-2, 3*i2-1, 3*i2]
  do i = 1,6
    x6(i) = hyperdual(x(idx6(i)),0d0,0d0,0d0)
  enddo
  do i = 1,6
    do j = 1,6
      x6mod = x6
      x6mod(i) = x6mod(i) + hyperdual(0d0,1d0,0d0,0d0)
      x6mod(j) = x6mod(j) + hyperdual(0d0,0d0,1d0,0d0)
      delx = x6mod(1) - x6mod(4)
      dely = x6mod(2) - x6mod(5)
      delz = x6mod(3) - x6mod(6)
      rsq = delx*delx + dely*dely + delz*delz
      r = rsq**(1d0/2d0)
      r0hdn = hyperdual(r0(bondtype),0d0,0d0,0d0)
      dr = r - r0hdn
      kshdn = hyperdual(ks(bondtype),0d0,0d0,0d0)
      rk = kshdn * dr
      e = rk * dr
      h6(i,j) = dual12(e)
    enddo
  enddo
  h(idx6,idx6) = h(idx6,idx6) + h6
enddo

! Hessian of bending energy
do n = 1,ndihedrallist
  i1 = dihedrallist(n,1)
  i2 = dihedrallist(n,2)
  i3 = dihedrallist(n,3)
  i4 = dihedrallist(n,4)
  dihedraltype = dihedrallist(n,5)
  idx12 = [3*i1-2, 3*i1-1, 3*i1, 3*i2-2, 3*i2-1, 3*i2, 3*i3-2, 3*i3-1, 3*i3, &
    3*i4-2, 3*i4-1, 3*i4]
  do i = 1,12
    x12(i) = hyperdual(x(idx12(i)),0d0,0d0,0d0)
  enddo
  do i = 1,12
    do j = 1,12
      x12mod = x12
      x12mod(i) = x12mod(i) + hyperdual(0d0,1d0,0d0,0d0)
```

```
x12mod(j) = x12mod(j) + hyperdual(0d0,0d0,1d0,0d0)
vb1x = x12mod(1) - x12mod(4)
vb1y = x12mod(2) - x12mod(5)
vb1z = x12mod(3) - x12mod(6)
vb2x = x12mod(7) - x12mod(4)
vb2y = x12mod(8) - x12mod(5)
vb2z = x12mod(9) - x12mod(6)
vb2xm = -vb2x
vb2ym = -vb2y
vb2zm = -vb2z
vb3x = x12mod(10) - x12mod(7)
vb3y = x12mod(11) - x12mod(8)
vb3z = x12mod(12) - x12mod(9)
ax = vb1y*vb2zm - vb1z*vb2ym
ay = vb1z*vb2xm - vb1x*vb2zm
az = vb1x*vb2ym - vb1y*vb2xm
bx = vb3y*vb2zm - vb3z*vb2ym
by = vb3z*vb2xm - vb3x*vb2zm
bz = vb3x*vb2ym - vb3y*vb2xm
rasq = ax*ax + ay*ay + az*az
rbsq = bx*bx + by*by + bz*bz
rgsq = vb2xm*vb2xm + vb2ym*vb2ym + vb2zm*vb2zm
rg = rgsq**(1d0/2d0)
rginv = zero
ra2inv = zero
rb2inv = zero
if (real_(rg) > 0d0) then
    rginv = one/rg
endif
if (real_(rasq) > 0d0) then
    ra2inv = one/rasq
endif
if (real_(rbsq) > 0d0) then
    rb2inv = one/rbsq
endif
rabinv = (ra2inv*rb2inv)**(1d0/2d0)
c = (ax*bx + ay*by + az*bz)*rabinv
s = rg*rabinv*(ax*vb3x + ay*vb3y + az*vb3z)
if (real_(c) > 1d0) then
    c%a = 1d0
endif
if (real_(c) < -1d0) then
    c%a = -1d0
endif
p = one
ddf1 = zero
df1 = zero
ddf1 = p*c - df1*s
df1 = p*s + df1*c
p = ddf1
cos_shift = hyperdual(cos(phi0(dihedraltype)),0d0,0d0,0d0)
sin_shift = hyperdual(sin(phi0(dihedraltype)),0d0,0d0,0d0)
p = p*cos_shift + df1*sin_shift
df1 = df1*cos_shift - ddf1*sin_shift
df1 = -df1
p = p + one
fg = vb1x*vb2xm + vb1y*vb2ym + vb1z*vb2zm
hg = vb3x*vb2xm + vb3y*vb2ym + vb3z*vb2zm
fga = fg*ra2inv*rginv
hgb = hg*rb2inv*rginv
gaa = -ra2inv*rg
```

```
          gbb = rb2inv*rg
          dtfx = gaa*ax
          dtfy = gaa*ay
          dtfz = gaa*az
          dtgx = fga*ax - hgb*bx
          dtgy = fga*ay - hgb*by
          dtgz = fga*az - hgb*bz
          dthx = gbb*bx
          dthy = gbb*by
          dthz = gbb*bz
          kbhdn = hyperdual(kb(dihedraltype),0d0,0d0,0d0)
          e = kbhdn*p
          h12(i,j) = dual12(e)
        enddo
      enddo
      h(idx12,idx12) = h(idx12,idx12) + h12
    enddo

  end subroutine comph

  ! ------------------------------------------------------------------------------

  subroutine comphdiff(x,h)
    implicit none
    double precision, intent(in) :: x(ndof)
    double precision, intent(out) :: h(ndof,ndof)
    double precision :: v1(ndof), v2(ndof), dx(ndof), etmp
    double precision, parameter :: eps0=1d-5
    integer :: i
    do i = 1,ndof
      dx = 0d0
      dx(i) = eps0
      call compev(x-dx,etmp,v1)
      call compev(x+dx,etmp,v2)
      h(:,i) = (v2-v1)/(2d0*eps0)
    enddo
  end subroutine comphdiff

end module dsm

! ================================================================================
```

References

[1] Euler, L. (1744). *Methodus inveniendi lineas curvas maximi minimive proprietate gaudentes.* Marcum Michaelem Bosquet.

[2] Timoshenko, S. (1953). *History of strength of materials: with a brief account of the history of theory of elasticity and theory of structures.* Dover Publications.

[3] Bažant, Z. P. (2000). Structural stability. *International Journal of Solids and Structures*, 37(1-2), 55-67.

[4] Bazant, Z. and Cedolin, L. (2010). *Stability of structures: elastic, inelastic, fracture and damage theories.* World Scientific.

[5] Reis, P. M. (2015). A perspective on the revival of structural (in) stability with novel opportunities for function: from buckliphobia to buckliphilia. *Journal of Applied Mechanics*, 82(11).

[6] Reis, P. M., Brau, F., & Damman, P. (2018). The mechanics of slender structures. *Nature Physics*, 14(12), 1150-1151.

[7] Rus, D., & Tolley, M. T. (2015). Design, fabrication and control of soft robots. *Nature*, 521(7553), 467-475.

[8] Zhai, Z., Wang, Y., & Jiang, H. (2018). Origami-inspired, on-demand deployable and collapsible mechanical metamaterials with tunable stiffness. Proceedings of the National Academy of Sciences, 115(9), 2032-2037.

[9] Fu, H., Nan, K., Bai, W., Huang, W., Bai, K., Lu, L., ... & Han, M. (2018). Morphable 3D mesostructures and microelectronic devices by multistable buckling mechanics. Nature materials, 17(3), 268-276.

[10] Pellegrino, S. (Ed.). (2014). *Deployable structures*. Springer.

[11] Dagdeviren, C., Joe, P., Tuzman, O. L., Park, K. I., Lee, K. J., Shi, Y., ... & Rogers, J. A. (2016). Recent progress in flexible and stretchable piezoelectric devices for mechanical energy harvesting, sensing and actuation. Extreme mechanics letters, 9, 269-281.

[12] Haghpanah, B., Shirazi, A., Salari-Sharif, L., Izard, A. G., & Valdevit, L. (2017). Elastic architected materials with extreme damping capacity. *Extreme Mechanics Letters*, 17, 56-61.

[13] Terwagne, D., Brojan, M., & Reis, P. M. (2014). Smart morphable surfaces for aerodynamic drag control. *Advanced materials*, 26(38), 6608-6611.

[14] Cerda, E., & Mahadevan, L. (2003). Geometry and physics of wrinkling. *Physical review letters*, 90(7), 074302.

[15] Hure, J., Roman, B., & Bico, J. (2012). Stamping and wrinkling of elastic plates. *Physical review letters*, 109(5), 054302.

[16] Stoop, N., Lagrange, R., Terwagne, D., Reis, P. M., & Dunkel, J. (2015). Curvature-induced symmetry breaking determines elastic surface patterns. *Nature materials*, 14(3), 337-342.

[17] Paulsen, J. D. (2019). Wrapping liquids, solids, and gases in thin sheets. *Annual Review of Condensed Matter Physics*, 10, 431-450.

[18] Klein, Y., Venkataramani, S., & Sharon, E. (2011). Experimental study of shape transitions and energy scaling in thin non-Euclidean plates. *Physical review letters*, 106(11), 118303.

[19] Bowden, N., Brittain, S., Evans, A. G., Hutchinson, J. W., & Whitesides, G. M. (1998). Spontaneous formation of ordered structures in thin films of metals supported on an elastomeric polymer. *Nature*, 393(6681), 146-149.

[20] Breid, D., & Crosby, A. J. (2011). Effect of stress state on wrinkle morphology. *Soft Matter*, 7(9), 4490-4496.

[21] Savin T, Kurpios NA, Shyer AE, Florescu P, Liang H, Mahadevan L, Tabin CJ. On the growth and form of the gut. *Nature*. 2011 Aug;476(7358):57-62.

[22] Kücken, M., & Newell, A. C. (2004). A model for fingerprint formation. *EPL (Europhysics Letters)*, 68(1), 141.

[23] Nelson, C. M. (2016). On buckling morphogenesis. *Journal of biomechanical engineering*, 138(2).

[24] Richman, D. P., Stewart, R. M., Hutchinson, J. W., & Caviness, V. S. (1975). Mechanical model of brain convolutional development. *Science*, 189(4196), 18-21.

[25] Savin, T., Kurpios, N. A., Shyer, A. E., Florescu, P., Liang, H., Mahadevan, L., & Tabin, C. J. (2011). On the growth and form of the gut. *Nature*, 476(7358), 57-62.

[26] Schlecht, M., & Schulte, K. (1999). Advanced calculation of the room-temperature shapes of unsymmetric laminates. *Journal of Composite Materials*, 33(16), 1472-1490.

[27] Coburn, B. H., Pirrera, A., Weaver, P. M., & Vidoli, S. (2013). Tristability of an orthotropic doubly curved shell. *Composite Structures*, 96, 446-454.

[28] Li, H., Dai, F., Weaver, P. M., & Du, S. (2014). Bistable hybrid symmetric laminates. *Composite Structures*, 116, 782-792.

[29] Taylor, M., Davidovitch, B., Qiu, Z., & Bertoldi, K. (2015). A comparative analysis of numerical approaches to the mechanics of elastic sheets. *Journal of the Mechanics and Physics of Solids*, 79, 92-107.

[30] Grinspun, E., Hirani, A. N., Desbrun, M., & Schröder, P. (2003, July). Discrete shells. In *Proceedings of the 2003 ACM SIGGRAPH/Eurographics symposium on Computer animation* (pp. 62-67).

[31] Weischedel, C., Tuganov, A., Hermansson, T., Linn, J., & Wardetzky, M. (2012). Construction of discrete shell models by geometric finite differences.

[32] Grinspun, E., Gingold, Y., Reisman, J., & Zorin, D. (2006, September). Computing discrete shape operators on general meshes. In *Computer Graphics Forum* (Vol. 25, No. 3, pp. 547-556). Oxford, UK and Boston, USA: Blackwell Publishing, Inc.

[33] Gingold, Y., Secord, A., Han, J. Y., Grinspun, E., & Zorin, D. (2004, August). A discrete model for inelastic deformation of thin shells. In *ACM SIGGRAPH/Eurographics Symposium on Computer Animation*.

[34] Ripp, M. M., Démery, V., Zhang, T., & Paulsen, J. D. (2020). Geometry underlies the mechanical stiffening and softening of an indented floating film. *Soft Matter*, 16(17), 4121-4130.

[35] Zhang, T., Li, X., & Gao, H. (2015). Fracture of graphene: a review. *International Journal of Fracture*, 196(1-2), 1-31.

[36] Seung, H. S., & Nelson, D. R. (1988). Defects in flexible membranes with crystalline order. *Physical Review A*, 38(2), 1005.

[37] Hughes, T. J., & Liu, W. K. (1981). Nonlinear finite element analysis of shells: Part I. Three-dimensional shells. *Computer methods in applied mechanics and engineering*, 26(3), 331-362.

[38] Benson, D. J., Bazilevs, Y., Hsu, M. C., & Hughes, T. J. R. (2011). A large deformation, rotation-free, isogeometric shell. *Computer Methods in Applied Mechanics and Engineering*, 200(13-16), 1367-1378.

[39] Bathe, K. J., & Dvorkin, E. N. (1985). A four-node plate bending element based on Mindlin/Reissner plate theory and a mixed interpolation. *International Journal for Numerical Methods in Engineering*, 21(2), 367-383.

[40] Bathe, K. J., Brezzi, F., & Cho, S. W. (1989). The MITC7 and MITC9 plate bending elements. *Computers & Structures*, 32(3-4), 797-814.

[41] Simo, J. C., & Rifai, M. (1990). A class of mixed assumed strain methods and the method of incompatible modes. *International journal for numerical methods in engineering*, 29(8), 1595-1638.

[42] Bletzinger, K. U., Bischoff, M., & Ramm, E. (2000). A unified approach for shear-locking-free triangular and rectangular shell finite elements. *Computers & Structures*, 75(3), 321-334.

[43] Arnold, D., & Brezzi, F. (1997). Locking-free finite element methods for shells. *Mathematics of Computation*, 66(217), 1-14.

[44] Cirak, F., Ortiz, M., & Schröder, P. (2000). Subdivision surfaces: a new paradigm for thin-shell finite-element analysis. Int*ernational Journal for Numerical Methods in Engineering*, 47(12), 2039-2072.

[45] Benson, D. J., Bazilevs, Y., Hsu, M. C., & Hughes, T. J. R. (2011). A large deformation, rotation-free, isogeometric shell. *Computer Methods in Applied Mechanics and Engineering*, 200(13-16), 1367-1378.

[46] Benson, D. J., Bazilevs, Y., Hsu, M. C., & Hughes, T. J. R. (2010). Isogeometric shell analysis: the Reissner–Mindlin shell. *Computer Methods in Applied Mechanics and Engineering*, 199(5-8), 276-289.

[47] Grinspun, E., Gingold, Y., Reisman, J., & Zorin, D. (2006, September). Computing discrete shape operators on general meshes. In Computer Graphics Forum (Vol. 25, No. 3, pp. 547-556). Oxford, UK and Boston, USA: Blackwell Publishing, Inc.

[48] Ciarlet, P. G. (2005). An introduction to differential geometry with applications to elasticity. *Journal of Elasticity*, 78(1-3), 1-215.

[49] Koiter, W. T. (1966). On the nonlinear theory of thin elastic shells. *Proc. Koninkl. Ned. Akad. van Wetenschappen*, Series B, 69, 1-54.

[50] Steigmann, D. J. (2013). Koiter's shell theory from the perspective of three-dimensional nonlinear elasticity. *Journal of Elasticity*, 111(1), 91-107.

[51] Reddy, J. N. (2006). Theory and analysis of elastic plates and shells. *CRC press*.

[52] Mardare, C. (2008). On the derivation of nonlinear shell models from three-dimensional elasticity. *Rev Roumaine Maths Pures Appl*, 53, 499–522.

[53] Naghdi, P. M. (1962). Foundations of elastic shell theory (No. TR15). CALIFORNIA UNIV BERKELEY INST OF ENGINEERING RESEARCH.

[54] Hale, J. S., Brunetti, M., Bordas, S. P., & Maurini, C. (2018). Simple and extensible plate and shell finite element models through automatic code generation tools. *Computers & Structures*, 209, 163-181.

[55] Taylor, M., Bertoldi, K., & Steigmann, D. J. (2014). Spatial resolution of wrinkle patterns in thin elastic sheets at finite strain. J*ournal of the Mechanics and Physics of Solids*, 62, 163-180.

[56] Taylor, M., Davidovitch, B., Qiu, Z., & Bertoldi, K. (2015). A comparative analysis of numerical approaches to the mechanics of elastic sheets. *Journal of the Mechanics and Physics of Solids*, 79, 92-107.

[57] Gingold, Y., Secord, A., Han, J. Y., Grinspun, E., & Zorin, D. (2004, August). A discrete model for inelastic deformation of thin shells. In ACM SIGGRAPH/Eurographics Symposium on Computer Animation.

[58] Weischedel, C., Tuganov, A., Hermansson, T., Linn, J., & Wardetzky, M. (2012). Construction of discrete shell models by geometric finite differences.

[59] Baraff, D., & Witkin, A. (1998, July). Large steps in cloth simulation. In Proceedings of the 25th annual conference on Computer graphics and interactive techniques (pp. 43-54).

[60] Grinspun, E., Hirani, A. N., Desbrun, M., & Schröder, P. (2003, July). Discrete shells. In Proceedings of the 2003 ACM SIGGRAPH/Eurographics symposium on Computer animation (pp. 62-67).

[61] Seung, H. S., & Nelson, D. R. (1988). Defects in flexible membranes with crystalline order. *Physical Review A*, 38(2), 1005.

[62] DiDonna, B. A. (2002). Scaling of the buckling transition of ridges in thin sheets. *Physical Review E*, 66(1), 016601.

[63] Liang, T., & Witten, T. A. (2005). Crescent singularities in crumpled sheets. *Physical Review E*, 71(1), 016612.

[64] Wang, J. W. (2011). Rim curvature anomaly in thin conical sheets revisited. *Physical Review E*, 84(6), 066603.

[65] Zupan, D., & Saje, M. (2004). On "A proposed standard set of problems to test finite element accuracy": the twisted beam. *Finite elements in analysis and design*, 40(11), 1445-1451.

[66] White, D. W., & Abel, J. F. (1989). Testing of shell finite element accuracy and robustness. *Finite elements in Analysis and Design*, 6(2), 129-151.

[67] Plimpton, S. (1995). Fast parallel algorithms for short-range molecular dynamics. *Journal of computational physics*, 117(1), 1-19.

[68] Timoshenko, S. P., & JN Goodier, J. N. (1968). *Theory of elasticity*. McGraw Hill. New York.

[69] Reddy, J. N. (2006). Theory and analysis of elastic plates and shells. *CRC press*.

[70] Paulsen, J. D. (2019). Wrapping liquids, solids, and gases in thin sheets. *Annual Review of Condensed Matter Physics*, 10, 431-450.

[71] https://lammps.sandia.gov/

[72] Koiter, W. T. (1963). The effect of axisymmetric imperfections on the buckling of cylindrical shells under axial compression. *Proceedings, Kon. Ned. Ak. Wet.*, 66, 265-279.

[73] Hutchinson, J. W. (1967). Imperfection sensitivity of externally pressurized spherical shells. *Journal of Applied Mechanics*, 34, 49-55

[74] Hunt, G. W., Lord, G. J., & Peletier, M. A. (2003). Cylindrical shell buckling: a characterization of localization and periodicity. *Discrete & Continuous Dynamical Systems-B*, 3(4), 505.

[75] Horák, J., Lord, G. J., & Peletier, M. A. (2006). Cylinder buckling: the mountain pass as an organizing center. *SIAM Journal on Applied Mathematics*, 66(5), 1793-1824.

[76] Vaziri, A., & Mahadevan, L. (2008). Localized and extended deformations of elastic shells. *Proceedings of the National Academy of Sciences*, 105(23), 7913-7918.

[77] Kreilos, T., & Schneider, T. M. (2017). Fully localized post-buckling states of cylindrical shells under axial compression. *Proceedings of the Royal Society A: Mathematical, Physical and Engineering Sciences*, 473(2205), 20170177.

[78] Audoly, B., & Hutchinson, J. W. (2020). Localization in spherical shell buckling. *Journal of the Mechanics and Physics of Solids*, 136, 103720.

[79] Groh, R. M. J., & Pirrera, A. (2019). On the role of localizations in buckling of axially compressed cylinders. *Proceedings of the Royal Society A*, 475(2224), 20190006.

[80] Thompson JM. Advances in shell buckling: theory and experiments. *International Journal of Bifurcation and Chaos.* 2015 Jan;25(01):1530001.

[81] Hutchinson, J. W. (2016). Buckling of spherical shells revisited. *Proceedings of the Royal Society A: Mathematical, Physical and Engineering Sciences*, 472(2195), 20160577.

[82] Hutchinson, J. W., & Thompson, J. M. T. (2017). Nonlinear buckling behaviour of spherical shells: barriers and symmetry-breaking dimples. *Philosophical Transactions of the Royal Society A: Mathematical, Physical and Engineering Sciences*, 375(2093), 20160154.

[83] Hutchinson, J. W., & Thompson, J. M. T. (2017). Nonlinear buckling interaction for spherical shells subject to pressure and probing forces. *Journal of Applied Mechanics*, 84(6).

[84] Lee, A., López Jiménez, F., Marthelot, J., Hutchinson, J. W., & Reis, P. M. (2016). The geometric role of precisely engineered imperfections on the critical buckling load of spherical elastic shells. *Journal of Applied Mechanics*, 83(11).

[85] Virot, E., Kreilos, T., Schneider, T. M., & Rubinstein, S. M. (2017). Stability landscape of shell buckling. *Physical review letters*, 119(22), 224101.

[86] Marthelot, J., López Jiménez, F., Lee, A., Hutchinson, J. W., & Reis, P. M. (2017). Buckling of a pressurized hemispherical shell subjected to a probing force. *Journal of Applied Mechanics*, 84(12).

[87] Thompson, J. M. T., Hutchinson, J. W., & Sieber, J. (2017). Probing shells against buckling: a nondestructive technique for laboratory testing. *International Journal of Bifurcation and Chaos*, 27(14), 1730048.

[88] Hutchinson, J. W., & Thompson, J. M. T. (2018). Imperfections and energy barriers in shell buckling. *International Journal of Solids and Structures*, 148, 157-168.

[89] Plimpton, S. (1995). Fast parallel algorithms for short-range molecular dynamics. *Journal of computational physics*, 117(1), 1-19.

[90] Virot, E., Kreilos, T., Schneider, T. M., & Rubinstein, S. M. (2017). Stability landscape of shell buckling. *Physical review letters*, 119(22), 224101.

[91] Nocedal, J., & Wright, S. J. (1999). *Numerical Optimization*. Springer, New York, 2, 173-195.

[92] Press, W. H., Flannery, B. P., Teukolsky, S. A. & Vetterling, W. T. (1997). *Numerical Recipes in C*. Cambridge University Press, Cambridge, England.

[93] Leach, A. R. (2001). *Molecular Modelling: Principles and Applications*. Prentice Hall, Harrlow, UK.

[94] Schlick, T. (2002). *Molecular Modeling and Simulation: An Interdisciplinary Guide.* Interdisciplinary Applied Mathematics Vol. 21. Springer-Verlag, New York.

[95] Bitzek, E., Koskinen, P., Gähler, F., Moseler, M., & Gumbsch, P. (2006). Structural relaxation made simple. *Physical review letters*, 97(17), 170201.

[96] Beeler, J. R. (2012). *Radiation effects computer experiments.* Elsevier.

[97] Berne, B. J., Ciccotti, G., & Coker, D. F. (Eds.). (1998). *Classical and Quantum Dynamics in Condensed Phase Simulations: Proceedings of the International School of Physics.* World Scientific.

[98] Hagelaar, J. H. A., Bitzek, E., Flipse, C. F. J., & Gumbsch, P. (2006). Atomistic simulations of the formation and destruction of nanoindentation contacts in tungsten. *Physical Review B*, 73(4), 045425.

[99] Fletcher, R., & Reeves, C. M. (1964). Function minimization by conjugate gradients. *The Computer Journal*, 7(2), 149-154.

[100] Polak, E. (1971). Computational methods in optimization: a unified approach (Vol. 77). *Academic Press.*

[101] Broyden, C. G. (1970). The convergence of a class of double-rank minimization algorithms 1. general considerations. *IMA Journal of Applied Mathematics*, 6(1), 76-90.

[102] Fletcher, R. (1970). A new approach to variable metric algorithms. *The computer journal*, 13(3), 317-322.

[103] Goldfarb, D. (1970). A family of variable-metric methods derived by variational means. *Mathematics of computation*, 24(109), 23-26.

[104] Shanno, D. F. (1970). Conditioning of quasi-Newton methods for function minimization. *Mathematics of computation*, 24(111), 647-656.

[105] Liu, D. C., & Nocedal, J. (1989). On the limited memory BFGS method for large scale optimization. *Mathematical programming*, 45(1-3), 503-528.

[106] Berne, B. J., Ciccotti, G., & Coker, D. F. (Eds.). (1998). *Classical and Quantum Dynamics in Condensed Phase Simulations: Proceedings of the International School of Physics.* World Scientific.

[107] Henkelman, G., Uberuaga, B. P., & Jónsson, H. (2000). A climbing image nudged elastic band method for finding saddle points and minimum energy paths. *The Journal of chemical physics*, 113(22), 9901-9904.

[108] Henkelman, G., & Jónsson, H. (2000). Improved tangent estimate in the nudged elastic band method for finding minimum energy paths and saddle points. *The Journal of chemical physics*, 113(22), 9978-9985.

[109] Weinan, E., Ren, W., & Vanden-Eijnden, E. (2002). String method for the study of rare events. *Physical Review B*, 66(5), 052301.

[110] Weinan, E., Ren, W., & Vanden-Eijnden, E. (2007). Simplified and improved string method for computing the minimum energy paths in barrier-crossing events. *Journal of Chemical Physics*, 126(16), 164103.

[111] Ren, W., & Vanden-Eijnden, E. (2013). A climbing string method for saddle point search. *The Journal of chemical physics*, 138(13), 134105.

[112] Panter, J. R., Chen, J., Zhang, T., & Kusumaatmaja, H. (2019). Harnessing energy landscape exploration to control the buckling of cylindrical shells. *Communications Physics*, 2(1), 1-9.

[113] Taffetani, M., Jiang, X., Holmes, D. P., & Vella, D. (2018). Static bistability of spherical caps. *Proceedings of the Royal Society A: Mathematical, Physical and Engineering Sciences*, 474(2213), 20170910.

[114] Libai, A., & Simmonds, J. G. (2005). *The nonlinear theory of elastic shells.* Cambridge university press.

[115] Brinkmeyer, A., Santer, M., Pirrera, A., & Weaver, P. M. (2012). Pseudo-bistable self-actuated domes for morphing applications. *International Journal of Solids and Structures*, 49(9), 1077-1087.

[116] Yoshimura, Y. (1955). On the mechanism of buckling of a circular cylindrical shell under axial compression. (National Advisory Committee for Aeronautics, Washington, DC, 1955).

[117] Wales, D. (2003). Energy landscapes: Applications to clusters, biomolecules and glasses. *Cambridge University Press.*

[118] Wales, D. J., Miller, M. A., & Walsh, T. R. (1998). Archetypal energy landscapes. *Nature*, 394(6695), 758-760.

[119] Dagdeviren, C., Joe, P., Tuzman, O. L., Park, K. I., Lee, K. J., Shi, Y., ... & Rogers, J. A. (2016). Recent progress in flexible and stretchable piezoelectric devices for mechanical energy harvesting, sensing and actuation. *Extreme mechanics letters*, 9, 269-281.

[120] Fu, H., Nan, K., Bai, W., Huang, W., Bai, K., Lu, L., ... & Han, M. (2018). Morphable 3D mesostructures and microelectronic devices by multistable buckling mechanics. *Nature materials*, 17(3), 268-276.

[121] Cerda, E., & Mahadevan, L. (2003). Geometry and physics of wrinkling. *Physical review letters*, 90(7), 074302.

[122] Hure, J., Roman, B., & Bico, J. (2012). Stamping and wrinkling of elastic plates. *Physical review letters*, 109(5), 054302.

[123] Stoop, N., Lagrange, R., Terwagne, D., Reis, P. M., & Dunkel, J. (2015). Curvature-induced symmetry breaking determines elastic surface patterns. *Nature materials*, 14(3), 337-342.

[124] Paulsen, J. D. (2019). Wrapping liquids, solids, and gases in thin sheets. Annual Review of *Condensed Matter Physics*, 10, 431-450.

[125] Klein, Y., Venkataramani, S., & Sharon, E. (2011). Experimental study of shape transitions and energy scaling in thin non-Euclidean plates. *Physical review letters*, 106(11), 118303.

[126] Bowden, N., Brittain, S., Evans, A. G., Hutchinson, J. W., & Whitesides, G. M. (1998). Spontaneous formation of ordered structures in thin films of metals supported on an elastomeric polymer. *Nature*, 393(6681), 146-149.

[127] Breid, D., & Crosby, A. J. (2011). Effect of stress state on wrinkle morphology. *Soft Matter*, 7(9), 4490-4496.

[128] Savin, T., Kurpios, N. A., Shyer, A. E., Florescu, P., Liang, H., Mahadevan, L., & Tabin, C. J. (2011). On the growth and form of the gut. *Nature*, 476(7358), 57-62.

[129] Kücken, M., & Newell, A. C. (2004). A model for fingerprint formation. *EPL (Europhysics Letters)*, 68(1), 141.

[130] Paulsen, J. D., Hohlfeld, E., King, H., Huang, J., Qiu, Z., Russell, T. P., ... & Davidovitch, B. (2016). Curvature-induced stiffness and the spatial variation of wavelength in wrinkled sheets. *Proceedings of the National Academy of Sciences*, 113(5), 1144-1149.

[131] Huang, J., Juszkiewicz, M., De Jeu, W. H., Cerda, E., Emrick, T., Menon, N., & Russell, T. P. (2007). Capillary wrinkling of floating thin polymer films. *Science*, 317(5838), 650-653.

[132] King, H., Schroll, R. D., Davidovitch, B., & Menon, N. (2012). Elastic sheet on a liquid drop reveals wrinkling and crumpling as distinct symmetry-breaking instabilities. *Proceedings of the National Academy of Sciences*, 109(25), 9716-9720.

[133] Aharoni, H., Todorova, D. V., Albarrán, O., Goehring, L., Kamien, R. D., & Katifori, E. (2017). The smectic order of wrinkles. *Nature communications*, 8(1), 1-7.

[134] Huang, J., Davidovitch, B., Santangelo, C. D., Russell, T. P., & Menon, N. (2010). Smooth cascade of wrinkles at the edge of a floating elastic film. P*hysical review letters*, 105(3), 038302.

[135] Pineirua, M., Tanaka, N., Roman, B., & Bico, J. (2013). Capillary buckling of a floating annulus. *Soft Matter*, 9(46), 10985-10992.

[136] Davidovitch, B., Schroll, R. D., Vella, D., Adda-Bedia, M., & Cerda, E. A. (2011). Prototypical model for tensional wrinkling in thin sheets. *Proceedings of the National Academy of Sciences*, 108(45), 18227-18232.

[137] Davidovitch, B., Schroll, R. D., & Cerda, E. (2012). Nonperturbative model for wrinkling in highly bendable sheets. *Physical Review E*, 85(6), 066115.

[138] Vella, D., Adda-Bedia, M., & Cerda, E. (2010). Capillary wrinkling of elastic membranes. *Soft Matter*, 6(22), 5778-5782.

[139] Taylor, M., Davidovitch, B., Qiu, Z., & Bertoldi, K. (2015). A comparative analysis of numerical approaches to the mechanics of elastic sheets. *Journal of the Mechanics and Physics of Solids*, 79, 92-107.

[140] Timoshenko, S. P., & Goodier, J. N. (1970). *Theory of Elasticity*. McGraw-Hill.

[141] Schroll, R. D., Adda-Bedia, M., Cerda, E., Huang, J., Menon, N., Russell, T. P., ... & Davidovitch, B. (2013). Capillary deformations of bendable films. *Physical review letters*, 111(1), 014301.

[142] Démery, V., Davidovitch, B., & Santangelo, C. D. (2014). Mechanics of large folds in thin interfacial films. *Physical Review E*, 90(4), 042401.

[143] Tovkach, O., Chen, J., Ripp, M. M., Zhang, T., Paulsen, J. D., & Davidovitch, B. (2020). Mesoscale structure of wrinkle patterns and defect-proliferated liquid crystalline phases. *Proceedings of the National Academy of Sciences*, 117(8), 3938-3943.

[144] Overvelde, J. T., Weaver, J. C., Hoberman, C., & Bertoldi, K. (2017). Rational design of reconfigurable prismatic architected materials. *Nature*, 541(7637), 347-352.

[145] Filipov, E. T., Tachi, T., & Paulino, G. H. (2015). Origami tubes assembled into stiff, yet reconfigurable structures and metamaterials. *Proceedings of the National Academy of Sciences*, 112(40), 12321-12326.

[146] Kim, Y., Yuk, H., Zhao, R., Chester, S. A., & Zhao, X. (2018). Printing ferromagnetic domains for untethered fast-transforming soft materials. *Nature*, 558(7709), 274-279.

[147] Wehner, M., Truby, R. L., Fitzgerald, D. J., Mosadegh, B., Whitesides, G. M., Lewis, J. A., & Wood, R. J. (2016). An integrated design and fabrication strategy for entirely soft, autonomous robots. *Nature*, 536(7617), 451-455.

[148] Thesiya, D., Srinivas, A. R., & Shukla, P. (2015). A novel lateral deployment mechanism for segmented mirror/solar panel of space telescope. *Journal of Astronomical Instrumentation*, 4(03n04), 1550006.

[149] Fu, Y. H., Liu, A. Q., Zhu, W. M., Zhang, X. M., Tsai, D. P., Zhang, J. B., ... & Teng, J. H. (2011). A Micromachined Reconfigurable Metamaterial via Reconfiguration of Asymmetric Split-Ring Resonators. *Advanced Functional Materials*, 21(18), 3589-3594.

[150] Arnold, D., & Brezzi, F. (1997). Locking-free finite element methods for shells. *Mathematics of Computation*, 66(217), 1-14.

[151] Babaee, S., Overvelde, J. T., Chen, E. R., Tournat, V., & Bertoldi, K. (2016). Reconfigurable origami-inspired acoustic waveguides. *Science Advances*, 2(11), e1601019.

[152] Babaee, S., Viard, N., Wang, P., Fang, N. X., & Bertoldi, K. (2016). Harnessing deformation to switch on and off the propagation of sound. *Advanced Materials*, 28(8), 1631-1635.

[153] Deng, B., Wang, P., Tournat, V., & Bertoldi, K. (2020). Nonlinear transition waves in free-standing bistable chains. *Journal of the Mechanics and Physics of Solids*, 136, 103661.

[154] Damdam, A. N., Qaisar, N., & Hussain, M. M. (2019). Honeycomb-serpentine silicon platform for reconfigurable electronics. *Applied Physics Letters*, 115(11), 112105.

[155] Anderson, P. L., Mahoney, A. W., & Webster, R. J. (2017). Continuum reconfigurable parallel robots for surgery: Shape sensing and state estimation with uncertainty. *IEEE robotics and automation letters*, 2(3), 1617-1624.

[156] Shepherd, R. F. (2011). F. llievski, C. Wonjae, MA Stephen, SA Stokes, MD Aaron, C. Xin, W. Michael and GM Whitesides. *Proceedings of the National Academy of Sciences*, 51, 20400-20403.

[157] Plitea, N., Lese, D., Pisla, D., & Vaida, C. (2013). Structural design and kinematics of a new parallel reconfigurable robot. *Robotics and computer-integrated manufacturing*, 29(1), 219-235.

[158] Tang, Y., Li, Y., Hong, Y., Yang, S., & Yin, J. (2019). Programmable active kirigami metasheets with more freedom of actuation. *Proceedings of the National Academy of Sciences*, 116(52), 26407-26413.

[159] Liu, K., Tachi, T., & Paulino, G. H. (2019). Invariant and smooth limit of discrete geometry folded from bistable origami leading to multistable metasurfaces. *Nature communications*, 10(1), 1-10.

[160] Wang, Q., Rogers, E. T., Gholipour, B., Wang, C. M., Yuan, G., Teng, J., & Zheludev, N. I. (2016). Optically reconfigurable metasurfaces and photonic devices based on phase change materials. *Nature Photonics*, 10(1), 60-65.

[161] Huang, C., Zhang, C., Yang, J., Sun, B., Zhao, B., & Luo, X. (2017). Reconfigurable metasurface for multifunctional control of electromagnetic waves. *Advanced Optical Materials*, 5(22), 1700485.

[162] Nemati, A., Wang, Q., Hong, M., & Teng, J. (2018). Tunable and reconfigurable metasurfaces and metadevices. *Opto-Electronic Advances*, 1(5), 180009.

[163] Song, Y., Panas, R. M., Chizari, S., Shaw, L. A., Jackson, J. A., Hopkins, J. B., & Pascall, A. J. (2019). Additively manufacturable micro-mechanical logic gates. *Nature communications*, 10(1), 1-6.

[164] Yang, H., & Ma, L. (2019). Multi-stable mechanical metamaterials by elastic buckling instability. *Journal of materials science*, 54(4), 3509-3526.

[165] O'Donnell, M. P., Towes, M., Groh, R. M., & Chenchiah, I. V. (2020). Exploring Adaptive Behavior of Non-linear Hexagonal Frameworks. *Frontiers in Materials*, 7, 64.

[166] Li, Y., & Pellegrino, S. (2020). A Theory for the Design of Multi-Stable Morphing Structures. *Journal of the Mechanics and Physics of Solids*, 136, 103772.

Vita

Junbo Chen was born on May 01, 1993 in Shanghai, China. He attended Tongji University in 2011 and received the B. S. in Civil Engineering in 2015. Upon graduation, he was enrolled in Northwestern University in 2015 and was rewarded the M.S. in civil engineering in 2017. Subsequently, he entered the Ph.D. program in Mechanical and Aerospace Engineering at Syracuse University in 2017. His research focused on modeling and simulation of morphological instabilities in thin elastic solids.